CRANFIELD UNIVERSITY

GANESH MOHAN

# A TOOLBOX FOR MULTI-OBJECTIVE OPTIMISATION OF LOW CARBON POWERTRAIN TOPOLOGIES

SCHOOL OF ENGINEERING
Department of Automotive Engineering

PhD
Academic Year: 2011 - 2014

Supervisors: Prof Francis Assadian
Dr Stefano Longo

May 2016

CRANFIELD UNIVERSITY

SCHOOL OF ENGINEERING
Department of Automotive Engineering

PhD

Academic Year 2011 - 2014

GANESH MOHAN

# A Toolbox for Multi-Objective Optimisation of Low Carbon Powertrain Topologies

Supervisors: Prof Francis Assadian
Dr Stefano Longo

May 2016

This thesis is submitted in partial fulfilment of the requirements for the degree of PhD

© Cranfield University 2014. All rights reserved. No part of this publication may be reproduced without the written permission of the copyright owner.

# ABSTRACT

Stricter regulations and evolving environmental concerns have been exerting ever-increasing pressure on the automotive industry to produce low carbon vehicles that reduce emissions. As a result, increasing numbers of alternative powertrain architectures have been released into the marketplace to address this need. However, with a myriad of possible alternative powertrain configurations, which is the most appropriate type for a given vehicle class and duty cycle? To that end, comparative analyses of powertrain configurations have been widely carried out in literature; though such analyses only considered limited types of powertrain architectures at a time. Collating the results from these literature often produced findings that were discontinuous, which made it difficult for drawing conclusions when comparing multiple types of powertrains.

The aim of this research is to propose a novel methodology that can be used by practitioners to improve the methods for comparative analyses of different types of powertrain architectures. Contrary to what has been done so far, the proposed methodology combines an optimisation algorithm with a Modular Powertrain Structure that facilitates the simultaneous approach to optimising multiple types of powertrain architectures. The contribution to science is two-folds; presenting a methodology to simultaneously select a powertrain architecture and optimise its component sizes for a given cost function, and demonstrating the use of multi-objective optimisation for identifying trade-offs between cost functions by powertrain architecture selection.

Based on the results, the sizing of the powertrain components were influenced by the power and energy requirements of the drivecycle, whereas the powertrain architecture selection was mainly driven by the autonomy range requirements, vehicle mass constraints, $CO_2$ emissions, and powertrain costs. For multi-objective optimisation, the creation of a 3-dimentional Pareto front showed multiple solution points for the different powertrain architectures, which was inherent from the ability of the methodology to concurrently evaluate those architectures. A diverging trend was observed on this front with the increase in the autonomy range, driven primarily by variation in powertrain cost per kilometre.

Additionally, there appeared to be a trade-off in terms of electric powertrain sizing between $CO_2$ emissions and lowest mass. This was more evident at lower autonomy ranges, where the battery efficiency was a deciding factor for $CO_2$ emissions.

The results have demonstrated the contribution of the proposed methodology in the area of multi-objective powertrain architecture optimisation, thus addressing the aims of this research.

Keywords:

Hybrid electric vehicle, genetic algorithm, scalable components, modular powertrain

# ACKNOWLEDGEMENTS

In loving memory of my brothers Sree Kumaressh Mohan and Saravanesh Mohan. I miss you both dearly. Your love and guidance has made this journey possible. May god bless your souls.

I want to begin by thanking my parents for their undivided love and support throughout the many ups and downs during this PhD. Their patience and guidance brought me back to my feet, and fuelled me with renewed courage to pursue my ambitions.

This thesis is dedicated to my supervisors, Prof Francis Assadian and Dr Stefano Longo, who did an excellent job of overseeing this research and shepherding it along. Your levels of enthusiasm were without doubt a true inspiration for me to charge ahead with this PhD. I also want to acknowledge Dr James Marco and Dr Daniel Auger whose valuable inputs made an impactful contribution to this thesis.

My utmost thanks goes to Ravi Shankar, my mentor and partner in crime, for the vast amounts of time and patience that you bestowed upon this research. You were a big help during my transition from vehicle dynamics into the unchartered territory of automotive powertrain engineering. This research would have never been possible without you.

To my lecturers and friends from the Department of Automotive Engineering, all of you deserve a big “thank you” for making my time at Cranfield University a truly enjoyable and memorable one.

This research would also have not been possible without the generous support from the funded projects, LCVTP and FUTURE vehicles, as well as the Smart Move trial program by Cenex.

Finally, I’d like to thank both my internal and external examiners, Dr Dongpu Cao and Prof Ricardo Martinez-Botas, for taking the time to read this thesis and providing constructive feedback to make it even better.

To the future readers of this thesis, I hope you will find some beneficial information from my research, and I want to thank you for your interest.

Ganesh Mohan

May 2016

# TABLE OF CONTENTS

# LIST OF FIGURES

# LIST OF TABLES

# LIST OF ABBREVIATIONS

| | |
|---|---|
| AC | Alternating Current |
| AER | All Electric Range |
| APU | Auxiliary Power Unit |
| BSFC | Brake Specific Fuel Consumption |
| CAN | Controller Area Network |
| CFRP | Carbon Fibre Reinforced Plastic |
| $CO_2$ | Carbon dioxide |
| CSV | Comma Separated Values |
| CV | Conventional Vehicle |
| CVT | Continuous Variable Transmission |
| DC | Direct Current |
| EEC | Equivalent Electrical Circuit |
| EM | Electrical Machine |
| EV | Electric Vehicle |
| FCEV | Fuel Cell EV |
| GA | Genetic Algorithm |
| GHG | Green House Gas |
| HEV | Hybrid Electric Vehicle |
| HIL | Hardware-In-the-Loop |
| ICE | Internal Combustion Engine |
| LCVTP | Low Carbon Vehicle Technical Partnership |
| MHV | Mechanical Hybrid Vehicle |
| MPS | Modular Powertrain Structure |
| NEDC | New European Drive Cycle |
| NREL | National Renewable Energy Laboratory |
| NSGA | Non-dominated Sorting-based Genetic Algorithm |
| NTS | National Travel Survey |
| OCV | Open Circuit Voltage |

| | |
|---|---|
| PHEV | Plug-in Hybrid Electric Vehicle |
| PI | Proportional-Integral (controller) |
| PM | Permanent Magnet (type of Electrical Machine) |
| PNGV | Partnership for a New Generation of Vehicles |
| PSAT | PNGV System Analysis Toolkit |
| SOC | State-of-Charge |

# LIST OF NOMENCLATURE

| | | |
|---|---|---|
| $a$ | Acceleration of vehicle | $m/s^2$ |
| $A_f$ | Frontal area of vehicle | $m^2$ |
| $C_D$ | Drag coefficient | - |
| $c_m$ | Mean piston speed | m/s |
| $e$ | Thermodynamic efficiency | - |
| $E_f$ | Flywheel energy | J |
| $E_{f(max)}$ | Maximum flywheel energy capacity | J |
| $E_{loss}$ | Energy dissipated from losses (flywheel) | J |
| $E_{max}$ | Maximum flywheel energy capacity | J |
| $F_A$ | Vehicle inertial forces | N |
| $F_D$ | Aerodynamic drag | N |
| $F_{inc}$ | Resistance due to road inclination | N |
| $F_{RR}$ | Rolling resistance | N |
| $F_T$ | Total force at tyre contact patch | N |
| $g$ | Acceleration due to gravity | $m/s^2$ |
| $G$ | Constraints (for optimisations) | - |
| $H_l$ | Fuel calorific heating value | J/kg |
| $I_b$ | Current flowing through battery | A |
| $I_{em}$ | Current flowing through EM | A |
| $I_L$ | Current flowing through cell | A |
| $J_f$ | Flywheel Inertia | $kg \cdot m^2$ |
| $m_f$ | Mass of flywheel | kg |
| $m_{fuel}$ | Fuel mass | kg |
| $m_v$ | Vehicle mass | kg |
| $n_p$ | Number of parallel strings (battery) | - |
| $n_s$ | Number of cells in series (battery) | - |
| $N_{stroke}$ | ICE Combustion cycle type (2/4 stroke) | - |
| $P_b$ | Battery power demand | W |
| $P_{b(loss)}$ | Power losses from battery | W |
| $P_{b(max)}$ | Maximum battery power | W |
| $P_{e(max)}$ | Maximum ICE power | W |
| $P_{em}$ | EM power demand | W |
| $P_{em(max)}$ | Maximum EM power | W |
| $P_f$ | Flywheel power demand | W |

| | | |
|---|---|---|
| $p_{loss}$ | Mean mechanical losses pressure | $N/m^2$ |
| $p_{me}$ | Piston mean effective pressure | $N/m^2$ |
| $p_{mf}$ | Fuel mean effective pressure | $N/m^2$ |
| $Q_b$ | Battery capacity | Ah |
| $Q_{b(max)}$ | Maximum battery capacity | Ah |
| $Q_{cell}$ | Cell capacity | Ah |
| $R_0$ | Cell internal resistance | Ω |
| $R_b$ | Battery internal resistance | Ω |
| $r_i$ | Flywheel inner radius | m |
| $r_o$ | Flywheel outer radius | m |
| $r_w$ | Tyre rolling radius | m |
| $S$ | Piston stroke length | m |
| $T_e$ | ICE torque | Nm |
| $T_{em}$ | EM torque | Nm |
| $T_{em(dmd)}$ | EM torque demand | Nm |
| $T_{gb}$ | Input torque to the transmission | Nm |
| $T_{loss}$ | Friction torque from bearing (flywheel) | Nm |
| $t_s$ | Simulation step time increment | s |
| $TtW\_CO_2$ | Tank-to-Wheel $CO_2$ | kg |
| $T_w$ | Torque at the wheels | Nm |
| $U_{L(cell)}$ | Terminal voltage (cell) | V |
| $U_{L(em)}$ | EM terminal voltage | V |
| $U_{OCV(batt)}$ | Open-circuit voltage (battery) | V |
| $U_{OCV(cell)}$ | Open-circuit voltage (cell) | V |
| $U_{string}$ | Potential difference across a string of cells | V |
| $v$ | Vehicle velocity | m/s |
| $V_d$ | Engine displacement | $m^3$ |
| $WtT\_CO_2$ | Well-to-tank $CO_2$ | kg |
| $WtW\_CO_2$ | Well-to-wheel $CO_2$ | kg |
| $X$ | Decision variables (for optimisations) | - |
| β | Weightings of two cost functions (multi-objective optimisation) | - |
| $\eta_b$ | Overall battery efficiency | - |
| $\eta_{CVT}$ | Efficiency of the CVT (flywheel) | - |
| $\eta_e$ | Overall engine efficiency | - |
| $\eta_{em}$ | Overall EM efficiency | - |

| | | |
|---|---|---|
| $\eta_{gb}$ | Overall transmission efficiency | - |
| $\theta$ | Angle of road inclination | rad |
| $\mu_{RR}$ | Rolling resistance coefficient | - |
| $\rho$ | Density of air | kg/m$^3$ |
| $\phi(X)$ | Cost function (for optimisations) | (varies) |
| $\varphi_{gb}$ | Gear ratio | - |
| $\omega_e$ | Engine speed | rad/s |
| $\omega_{em}$ | EM rotation speed | rad/s |
| $\omega_f$ | Flywheel rotational speed | rad/s |
| $\omega_{f(max)}$ | Maximum flywheel rotational speed | rad/s |
| $\omega_{gb}$ | Input angular velocity to the transmission | rad/s |
| $\omega_w$ | Wheel speed | rad/s |
| $\dot{m}_{fuel}$ | Fuel mass flow rate | kg/s |
| $E_k^t$ | Flywheel energy at time *t* | J |

# 1 INTRODUCTION

Road transportation is still the leading choice for mobility of people and goods [1]. However, stricter regulations and evolving environmental concerns have been exerting ever-increasing pressure on the automotive industry to produce vehicles that are more fuel efficient and lower in emissions. This is also in line with changes in consumer demands due to perceived risks of climate change and fluctuation in fossil fuel costs [2].

Several advanced powertrain solutions are being used by vehicle manufacturers to address this, including increasing the efficiency of Internal Combustion Engines (ICE), electric powertrains, and hybrid powertrains. A hybrid powertrain is defined as having two or more power sources to propel a vehicle [3], and can be further broken down into the following architectures: series hybrid powertrains, parallel hybrid powertrains, and compound hybrid powertrains.

Electric and hybrid powertrains are trending topics amongst academics and the industry. There are many possible topological combinations that constitute a hybrid powertrain, including but not limited to the following:

- Hybrid Electric Vehicles (HEV)
- Plug-in Hybrid Electric Vehicle (PHEV)
- Mechanical Hybrid Vehicle (MHV)
- Battery-Ultracapacitor HEV.

Each powertrain topology has its own advantage and shortcoming. Various publications have compared and contrasted these topologies to identify the most promising configuration, chiefly for reducing emissions. However, literature survey carried out as part of this research has revealed conflicting findings because of variations in methodology, assumptions, and modelling techniques.

Furthermore, the pressures are mounting for both industry and governments in deciding on powertrain developmental paths. Providing and allocating finite capital and technological investments for developing future advanced powertrain technology are crucial for decision makers at all levels. One approach that could be used to assist in this process is a flexible powertrain simulation environment that allows for simultaneous analysis of different powertrain topologies, in order to access the suitability of a given topology for a particular vehicle class and its target duty cycle. This would alleviate the need for carrying out individual simulations on each type of powertrain topology separately, thus saving time and minimising variations in the simulation environment.

This research aims to investigate the feasibility of such an approach, by developing a methodology that would allow practitioners to identify the characteristics of each powertrain topology, and conduct insightful comparative analyses across various types of topologies. The proposed methodology lent itself to a simulation and optimisation

toolbox, which could ultimately be used to establish standards within the automotive modelling community.

This toolbox is useful to obtain a first-hand approximation for the type of powertrain that is most appropriate for a given vehicle type and duty cycle. It is suitable for preliminary powertrain design analysis, rather than specific higher-fidelity powertrain design. It can be used to predict measures such as fuel consumption, emissions, and running costs, and this is demonstrated by way of case studies throughout this thesis.

## 1.1 Research Motivation

With increasing pressure from legislative bodies for reduction in $CO_2$ emissions from road vehicles, alternative powertrain technologies are gaining considerable momentum. Apart from reducing emissions, the introduction of new powertrain technologies also helps bolster the image of the vehicle manufacturer and their commitment to environmental sustainability. Amongst the alternative powertrain architectures that are available on the market today include EVs, HEVs, and PHEVs. Another powertrain architecture that is gaining attention is the flywheel-based MHVs, derived from motorsports [4]. This architecture contains a flywheel that is mechanically coupled to the powertrain via a Continuous Variable Transmission (CVT).

The ability of alternative powertrains to reduce emissions is a topic of discussion amongst academics and the industry. HEVs are becoming increasingly popular [5], driven by the notion of reduced running costs due to lower fuel consumption when compared to Conventional Vehicles (CV) with an ICE. However, the level of advantage that is gained from reduced fuel consumption is dependent on how the vehicle is used. Similarly, a pure Electric Vehicle (EV) also becomes less suitable if the consumer requires a vehicle with a relatively long travel range and minimal refuel times [2]. With a myriad of alternative powertrain configurations that currently exist within the automotive industry, choosing the most appropriate powertrain architecture for the target vehicle class and duty cycle can be challenging [6]. There are ongoing researches and debates on trying to identify which is the most promising powertrain architecture for future low carbon vehicle propulsion [7-10].

Additionally, several cost functions can be used to optimise the size of the components within the powertrain architecture, such as lowest Carbon Dioxide ($CO_2$) emissions, lowest mass, component costs, or any combination of these attributes. However, in most literatures, such analyses were often carried out by comparing only limited types of powertrain architectures at a time [6; 11-15]. Hence, collating results from various literatures often produced findings that were discontinuous, thus making it difficult for drawing conclusions when comparing multiple types of powertrains. For example, An and Santini [16] compared the tank-to-wheel efficiencies of new powertrain

technologies by collating data from publications by MIT [17] and General Motors [18]. However, based on their findings, the analyses between the two publications demonstrated very different results and showed a wide range of uncertainties, primarily due to variations in the assumptions surrounding the powertrain models.

This is one of the factors that influenced the direction of this research. By improving the methodology used to compare different types of powertrain architectures, practitioners can quantify the benefits that can be achieved from each type of architecture on a level playing field, thus making it easier to develop the reasoning for manufacturers to accelerate the implementation of alternative powertrain technology [19]. Additionally, the comparative methods need to be flexible enough to accommodate emerging powertrain technologies, such as newer battery chemistries, fuel cell configurations, and so forth.

## 1.2 Research Hypothesis

The magnitude of reduction in emissions when comparing different powertrain technologies is dependent on how the vehicle is used. Like-for-like, powertrains that are capable of energy recuperation display significantly higher fuel savings in urban driving than in highway driving, when compared to conventional powertrains. This is a result of increased braking occurrences and speed variations. A study carried out by Fontaras *et al.* [20] suggested that HEVs exhibited reduction in $CO_2$ over CVs for urban duty cycles. However, this advantage is diminished as the duty cycle approaches that of a highway pattern, i.e. constant high-speed cruising. At this point, it could be argued that a CV could have similar overall fuel consumption to a HEV (for a given vehicle class) because of lower opportunities for regenerative braking and near steady-state operation of the ICE.

In the case of a PHEV, its total mass is usually heavier than that of a comparable CV, as observed when comparing the mass of Jaguar Limo Green to the conventional Jaguar XJ (Appendix C). If the PHEV usage does not exceed its All-Electric Range (AER), then its Auxiliary Power Unit (APU) essentially becomes “dead weight”, because its contribution to propulsion power would be minimal. Similarly, a pure EV also becomes less suitable if the consumer requires a vehicle with a relatively long autonomy range and minimal refuel times [2]. Although the battery can be sized up to meet the requirements of a long autonomy range, this will add considerable mass to the vehicle, and may affect other attributes such as handling and tyre wear [21].

Therefore, selecting the most appropriate powertrain architecture for a given vehicle class and duty cycle is favourable. Additionally, several cost functions can be used to optimise the size of the components within the powertrain architecture, such as lowest $CO_2$ emissions, lowest mass, component costs, or any combination of these attributes.

However, in most literatures, such analyses were often carried out by comparing only limited types of powertrain architectures at a time [6; 11-14]. Collating results from these literatures often produced findings that were discontinuous, thus making it difficult for drawing conclusions when comparing multiple types of powertrains.

This has motivated the research hypothesis; is it possible to determine the most appropriate powertrain architecture for a given vehicle type and usage profile, based on a unified optimisation routine? Identifying the options available in terms of powertrain architectures and quantifying the benefits that can be achieved from each type of architecture makes it easier to develop the reasoning for manufacturers to accelerate the implementation of alternative powertrain technology [19]. To investigate this hypothesis, further understanding would be required in the areas of powertrain modelling techniques, current state of powertrain architectures, as well as the state of simulation tools. These will be explored further in the next chapter.

## 1.3 Aims and Objectives

This research aims to investigate this hypothesis, by proposing a methodology to critically evaluate different powertrain architectures. To achieve this, a robust simulation toolbox that would enable comparative analysis of multiple powertrain architectures will be developed. The output from this toolbox could be used as a first-hand approximation for identifying the most appropriate powertrain topology depending on the vehicle class, duty cycle, and cost function, as demonstrated by the author in prior publications [22; 23]. To develop this toolbox, research was carried out in three different study areas, and this is represented by the Venn diagram in Figure 1.

In Figure 1, the “Powertrain Architectures” circle encompasses the range of powertrain architectures considered in this research, several of which were mentioned in the Introduction. Within each architecture, there are several “topologies”. A powertrain topology is defined as a subset of powertrain architecture, and contains one or more combinations of energy storage and energy converter. The classification of Powertrain Architecture and Powertrain Topology is shown in Figure 2.

Next, the “Vehicle Class” circle defines the type of vehicle that the powertrain will be simulated with, and contains parameters such as mass, aerodynamic drag, and rolling resistance. Finally, the “Duty Cycle” circle contains information on the usage profile of the vehicle, such as a representative drivecycle that it will encounter, as well as the required range that it has to travel before replenishing the on-board energy storage.

An optimisation algorithm is employed to provide an objective approach to comparing different powertrain topologies. It allows powertrain topologies to be compared for a given vehicle class and duty cycle. As a result, this enables the most appropriate powertrain topology to be selected and sized for a given vehicle application.

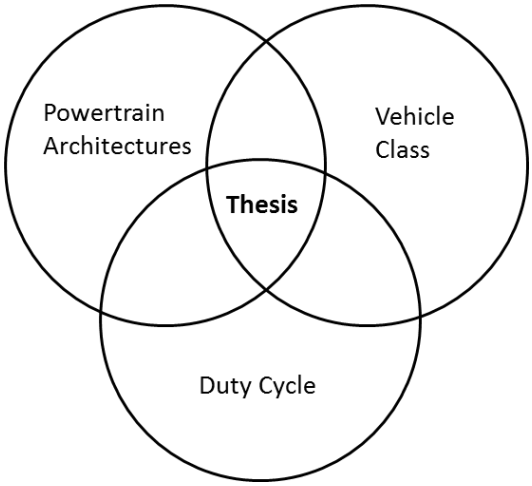


**Figure 1: PhD research scope**

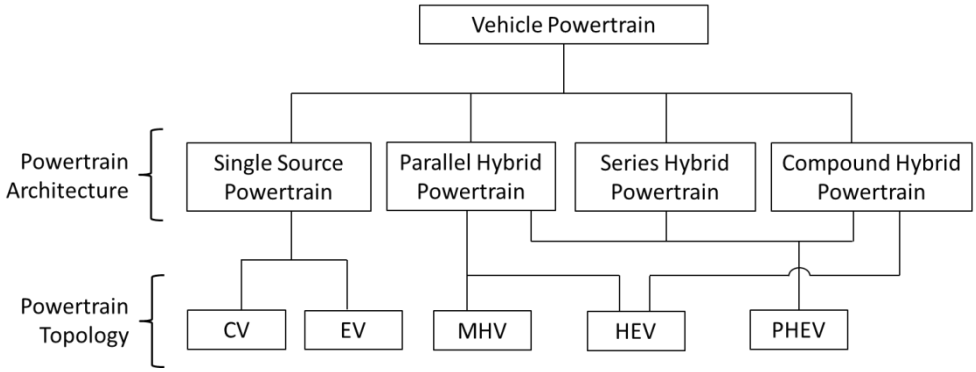


**Figure 2: Distinction between Powertrain Architecture and Powertrain Topology**

This research aims to compare hybrid powertrains in terms of:

- Fuel economy and emissions
- Estimated powertrain costs
- Power and energy demands from duty cycles

This list was drawn from literature review, and it is covered further in the next chapter.

## 1.4 Claim of Novelty

The original contribution to knowledge of this research is the following:

1. A methodology to simultaneously select a powertrain topology and optimise its component sizes for a given cost function
2. Utilising multi-objective optimisation for identifying trade-offs between cost functions by powertrain topology selection.

Each of the points above has been published by the author in [22] and [24] respectively.

Over the last decade, a myriad of low carbon powertrain technologies have been launched into the market [2]. Additionally, several commercial computer simulation packages have been developed to analyse vehicle powertrains, with varying degrees of fidelity. Examples include ADVISOR [25], PSAT [26], and the QSS toolbox [27].

However, based on underlying literature review, there has been no published work on combining such simulation software with comparative analysis capabilities for different powertrain topologies. In most literatures, comparative analyses of powertrains were carried out manually by comparing only limited types of powertrain topologies at a time [6; 11-13] [28]. Collating results from these literatures often produce findings that were discontinuous, which made it difficult for drawing conclusions when comparing multiple types of powertrains.

To address this, a novel methodology was developed that simultaneously optimises and compares powertrain topologies. Contrary to what has been done so far, the proposed methodology combines an optimisation algorithm with a Modular Powertrain Structure (MPS), which facilitates the simultaneous approach to comparing multiple types of powertrain architectures. The use of this methodology (in the form of a simulation toolbox) provides an objective evaluation of each type of powertrain architecture, and illustrates the potential impact of powertrain selection towards a given cost function, or multiple cost functions.

Thus, similar to using the commercial software packages mentioned above, practitioners would be able to optimise powertrain component sizes for a given cost function using the proposed methodology. However, the methodology also extends this capability by automating the selection of the powertrain topology as part of the optimisation routine. This capability underscores the first novelty of this research.

The application of multi-objective optimisation towards powertrain architecture selection and sizing also seems to be missing in the literature, and this will form the second novelty of this research. As mentioned in the introduction, the proposed approach could be used to establish standards within the automotive modelling community. Subsequent chapter will describe the implementation and results of this methodology by way of case studies.

## 1.5 List of Publications

The following are a list of publications that were produced over the course of this research to support its findings:

### 1.5.1 Conferences

- Mohan, G., Assadian, F. and Marco, J. (2012), "Influence of Cost Function on EV Powertrain Sizing", Powertrain Modelling and Control, September 4, Bradford
- Mohan, G., Assadian, F. and Longo, S. (2013), "Comparative analysis of forward-facing models vs backward-facing models in powertrain component sizing", IET 4th Hybrid and Electric Vehicles Conference (HEVC13), November 6-7, London
- Auger DJ, Groff MF, Mohan G, Longo S & Assadian F. (2013) The Impact of Battery Ageing on an Electric Vehicle Powertrain Optimisation., Dubrovnik, Croatia.
- Mohan, G., Assadian, A., and Longo, S., "Comparative Analysis of Multiple Powertrain Architectures based on a Novel Optimisation Framework" SAE Technical Paper 2014-01-1105, 2014

### 1.5.2 Journal Publication

- Mohan, G., Assadian, F., Longo, S. An Optimisation Framework for Comparative Analysis of Multiple Vehicle Powertrains. *Energies* **2013**, *6*, 5507-5537.

## 1.6 Thesis Outline

The complete layout of this thesis is presented as a flowchart in Figure 3. Having discussed the research motivation and objectives in this chapter, Chapter 2 covers the literature review and can be divided into three key areas: powertrain architectures, modelling techniques, and performance criteria. A slight discontinuity follows, where Chapter 3 discusses further on powertrain architectures specifically, and expands on the development of selected powertrain components.

Chapter 4 then merges the discussions from Chapters 2 and 3, and describes the integration of the powertrain topologies and components into the MPS, along with their integration to the optimiser. The findings from this chapter then merge with the discussion of cost functions from Chapter 2, and leads to the study of the sensitivity of cost functions towards optimisation results, in Chapter 5.

Chapters 6 and 7 highlight the first and second novelties of this research, by building upon the understanding gained from the previous chapters. This then finishes with Chapter 8, which covers the conclusions of this research as well as future work.

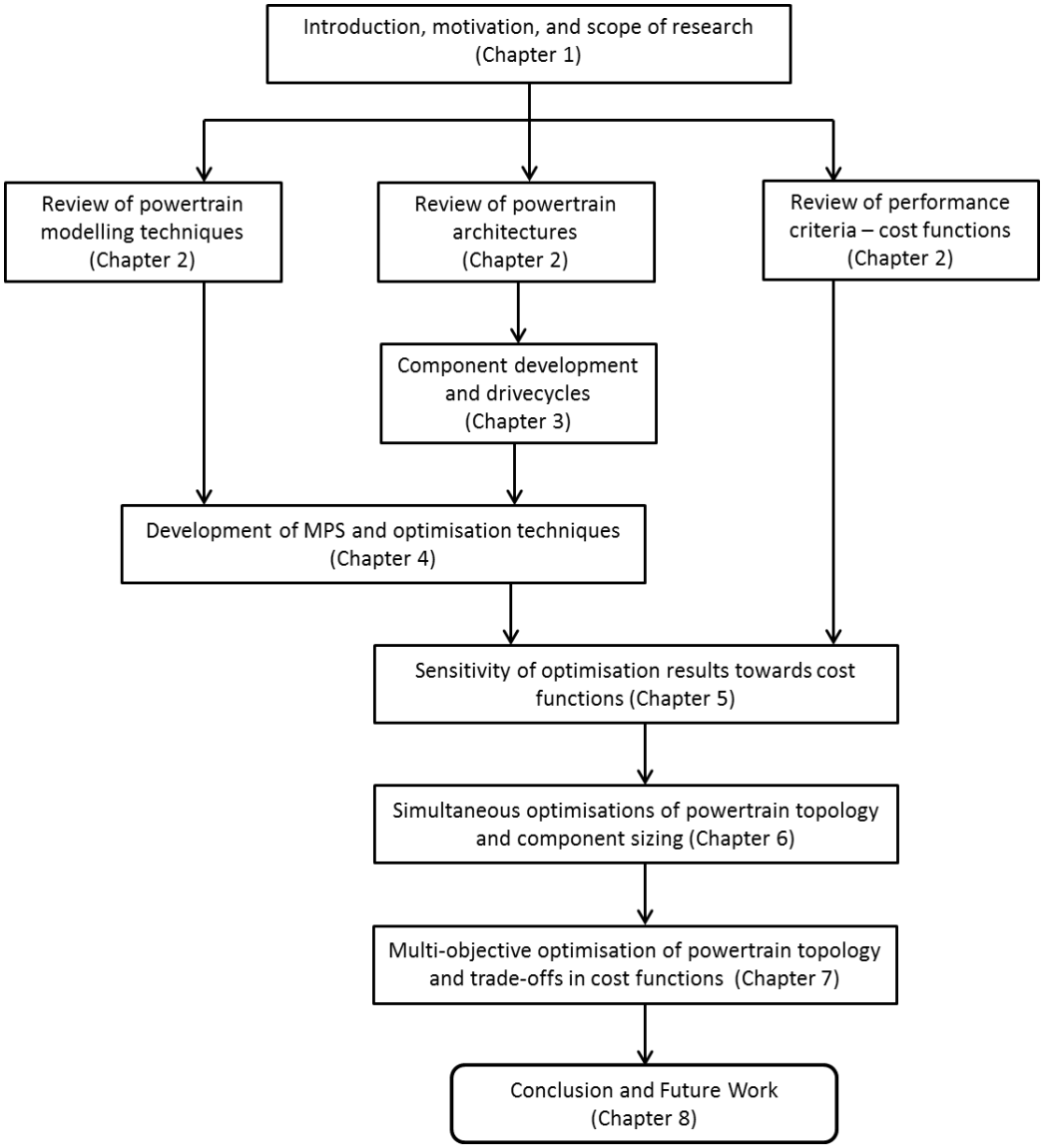


**Figure 3: Layout and flow of this thesis**

# 2 LITERATURE REVIEW

## 2.1 Review of Powertrain Modelling Techniques

The basic modelling technique for evaluating vehicle powertrains is the longitudinal dynamics simulation [29]. This technique involves dividing a given drivecycle into a number of time steps and calculating the characteristics of the vehicle at the end of each time interval. To achieve the desired longitudinal acceleration levels for a given drivecycle, powertrain components have to be sized appropriately to meet the desired performance levels. Assanis *et al.* stated that conventional powertrains are often oversized for the intended use of the vehicle, leading to the operating point deviating from the optimal operating range, and that a hybrid powertrain optimised for the intended usage could simultaneously improve vehicle performance at reduced emissions [30].

Backward-facing models, containing scalable powertrain components, are often used in the domain of powertrain size optimisation [31; 32]. Backward-facing models do not require a driver model, and the vehicle speed trace is obtained directly from the drivecycle. In a backward-facing model, the speed trace is imposed onto the vehicle model to calculate the angular velocity and torque at the wheels. Subsequently, the angular velocity and torque at the ICE (in the case of a CV) is determined "backwards" from the wheels through each drivetrain component, via efficiency models or maps. The efficiency maps are obtained from steady-state testing of real components, hence this is why backward-facing models are also considered as "quasi-static" models. These models also run with a relatively larger time step when compared to forward-facing models [32], resulting in quicker simulation times. These attributes have enabled backward-facing models to be used extensively in the area of powertrain component size optimisation [26; 33].

However, because of their quasi-static nature, backward-facing models give very limited information about measurable quantities in a vehicle such as throttle and brake position [32]. As a result, backward-facing models are less meaningful for implementation in hardware-in-the-loop (HIL) test systems [34].

In contrast, a dynamic system contains differential equations that describes the state of a system, and includes elements like inertia and inductance. As a result, dynamic systems are used in the forward-facing modelling approach, because forward-facing models deal with quantities that are measurable in real drivetrains and with the correct causality [35]. Forward-facing models also feature a driver model, which is typically a Proportional-Integral (PI) controller [26; 32].

### 2.1.1 Forward-facing Model

Using a CV as an example, the driver model provides torque demand in the form of desired ICE torque and brake torque, to meet the speed trace from a drivecycle. The topology of a representative forward-facing model is shown in Figure 4. A basic driver model typically uses one or more Proportional-Integral (PI) controllers to achieve the torque demand, with reference to the desired speed trace. The torque produced by the ICE propagates through the transmission and final drive ratios, before ending up as torque applied at the wheels. This is then exerted to the vehicle mass via force on the tyre contact patch. The vehicle speed that results from the applied force is propagated back through the drivetrain, and returns to the ICE as angular velocity at the crankshaft. Brake torque is applied directly at the wheels.

Unlike backward-facing models (Figure 5), the speed trace is not "imposed" onto the vehicle model in forward-facing models, and therefore there will inevitably be a small margin of error between the actual vehicle speed and the speed trace. It is the role of the driver model to minimise this margin of error. This is similar to the role of a real-world test driver carrying out an emissions test for vehicle type-approval.

Forward-facing models provide insight into the vehicle model drivability, and it captures the limits of the physical system [32; 36]. It also facilitates control systems development and implementation on HIL systems [34]. However, with the presence of multiple state equations in a typical forward-facing model, the vehicle speed (and subsequently drivetrain angular velocity) is computed via multiple state integration, resulting in the need to run the simulation in smaller time steps. This results in longer simulation times when compared to backward-facing models.

Furthermore, resizing the powertrain will alter the dynamics of the system. This potentially requires the driver model to be re-tuned to maximise the performance of the system in areas such as fuel economy and longitudinal acceleration.

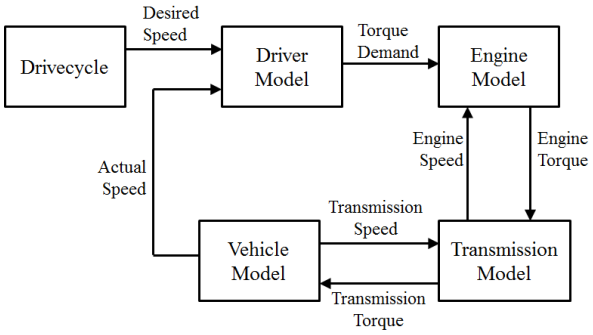


**Figure 4: Forward-facing (dynamic) vehicle model**

### 2.1.2 Backward-facing Model

The ability of the vehicle model to meet the demands of the drivecycle is the principal assumption of a backward-facing model [32]. Based on the speed trace from the drivecycle, the vehicle acceleration and resistive forces are calculated to determine the resultant tractive force at the tyre contact patch. It is then converted into wheel torque and propagated back to the ICE via the drivetrain, along with angular velocity. Therefore, in backward-facing models, the power information is mono-directional (effort and flow are in the same direction), as seen in Figure 5.

With both speed and torque imposed onto the powertrain components, a backward-facing model can also be considered as non-causal (physically non-realisable), as described by Hauer and Moore [37]. In contrast, based on Figure 4, it was observed that the transfer of power information is bi-directional in the forward-facing model, i.e. the direction of effort (torque) is opposite to the direction of flow (speed). Additionally, driver model of the forward-facing model is also absent in the backward-facing model

Backward-facing models rely on efficiency maps that were created based on torque and speed data, and usually produced during steady-state real-world testing. This results in the calculation being relatively simpler than forward-facing models (essentially lookup tables instead of state equations), and can therefore be run over relatively larger time steps. However, the use of steady-state maps also limits the ability of backward-facing models to accurately capture the transient performance of the powertrain.

During the optimisation routine, the powertrain component sizing is determined by the ability of the component to address both the speed and torque imposed on the component (i.e. the power requirements).

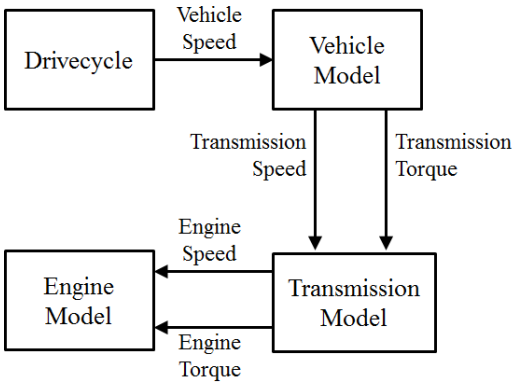


**Figure 5: Backward-facing (quasi-static) vehicle model**

### 2.1.3 Comparison of Forward-facing vs Backward-facing models

The backward-facing modelling approach is well documented for the study of the fuel consumption and emissions of vehicle powertrains. Nevertheless, the computational costs remain relatively low because of the map-based modelling approach. The main drawback of this method is that the physical causality is not respected and the speed profile of the drivecycle has to be known apriori. Therefore, this method is not able to handle feedback control problems or to correctly deal with state events; neither which are required to address the aims of this research.

In contrast, the forward-facing approach is desirable for hardware development and detailed control simulation, but the expense of the relatively high computational costs. A pure forward approach is therefore less suitable for preliminary powertrain design [38]. Table 1 summarises the key differences between the forward-facing and backward-facing modelling approach for the requirements of this research.

**Table 1: Comparison between forward-facing and backward-facing modelling methods**

| Criteria | Modelling approach | | Comment |
|---|---|---|---|
| | Forward-facing | Backward-facing | |
| Simulation time step | ~1 millisecond | ~1 second | Backward facing have shorter simulation times |
| Physical causality | Causal | Non-causal | Backward facing models are not suitable for HIL implementation |
| Model type | Dynamic | Quasi-static | Backward-facing models are map based and quicker to compute |
| Driver model | Required | Unnecessary | Backward-facing models assumes ideal driver model and vehicle speed trajectory is known apriori |

## 2.2 Review of Powertrain Architectures

Vehicle powertrains can be divided into two main categories; single source powertrain architecture and hybrid powertrain architectures. A hybrid powertrain is defined as having two or more power sources to propel the vehicle [3]. Hybrid powertrains can be broken down further into the following architectures:

- Series hybrid powertrain architecture (Section 2.2.2)
- Parallel hybrid powertrain architecture (Section 2.2.3)
- Compound hybrid powertrain architecture (Section 2.2.4)

### 2.2.1 Single Source Powertrain Architecture

CVs and EVs are examples of vehicles with single source powertrain architectures. These two powertrain architectures are represented as schematic diagrams in Figure 6 and Figure 7 respectively. The abbreviations shown in Table 2 apply to these figures.

In these schematic diagrams, the power flow is from left to right; it begins at the energy source and flows into the "wheel". For simplicity, the energy source from the electrical grid (battery charger) has been omitted in Figure 7.

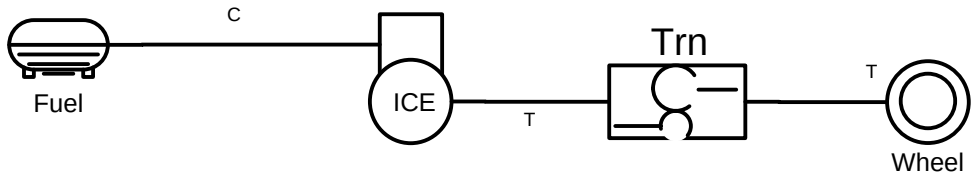


**Figure 6: Conventional ICE powertrain with transmission** [39]

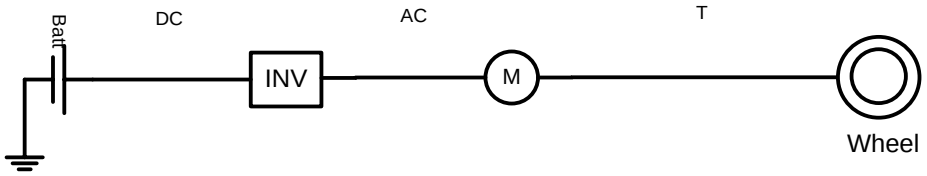


**Figure 7: Battery electric vehicle powertrain** [39]

**Table 2: Abbreviations used in the powertrain schematic diagrams**

| Term | Definition |
|---|---|
| C | Chemical energy |
| DC | Direct Current |
| AC | Alternating Current |
| T | Torque |
| Trn | Transmission |
| INV | Inverter |
| M | Electrical Machine |
| Batt | Battery Pack |

### 2.2.2 Series Hybrid Architecture

The series hybrid architecture is defined as having two (or more) power sources that are connected electrically, via a high-voltage electric bus or "DC bus" [40]. Similar to an EV powertrain, a series HEV usually has a battery and an Electrical Machine (EM) that

is mechanically connected to the wheels to provide tractive force. For the benefit of the discussion in this section, this will be referred to as the "primary" power source.

However, unlike the EV powertrain, a series HEV also has a "secondary" power source, which generally consists of system that converts stored chemical energy into electrical power. This electrical power then feeds into the DC bus. Hence, the secondary power source usually comprises a fuel tank and an ICE. However, it is also possible to replace the ICE with a fuel cell, thus forming a new topology within the series hybrid architecture. It should be reiterated that the secondary power source is not mechanically connected to the wheels in a series HEV powertrain architecture.

Figure 8 and Figure 9 show examples of possible topologies as part of the series hybrid architecture. In the first topology, the secondary power source comprises of a hydrogen tank ($H_2$), and a fuel cell. In the second topology, the secondary power source comprises of a fuel tank with an ICE and a generator.

Similarly, the primary power source also differs between those two topologies. In Figure 8, the primary power source contains an ultracapacitor (Cap) whilst in Figure 9 the primary power source contains a battery.

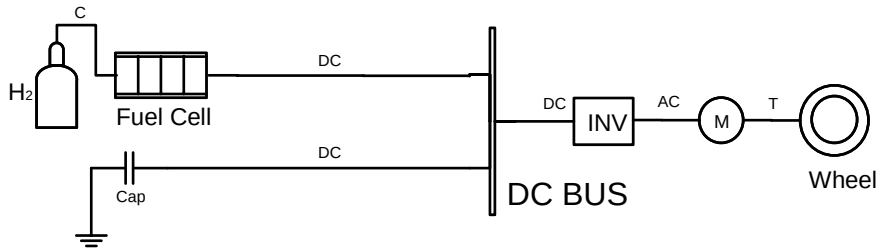


**Figure 8: Fuel cell hybrid powertrain topology**

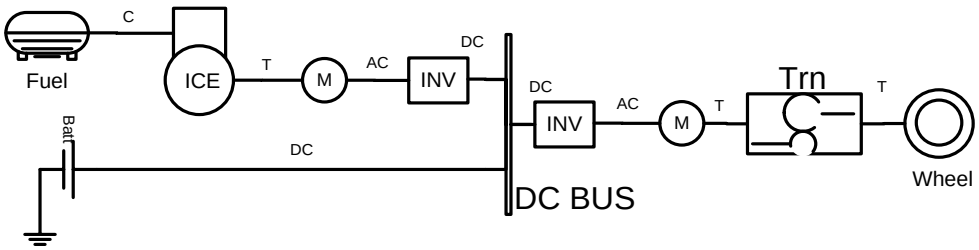


**Figure 9: Petrol-electric series hybrid powertrain topology**

Nevertheless, the drive system for both these topologies (downstream of the DC bus) is an EM coupled with power electronics (INV). Figure 9 also includes a transmission. This is an optional component, but may be required for high-speed applications.

### 2.2.3 Parallel Hybrid Architecture

Commonly, parallel hybrid architecture comprises of an ICE and an EM mounted to the output shaft, which draws power from a battery via power electronics. The combined torque is normally passed through a transmission, such as the topology shown in Figure 10. An example of a vehicle that uses this topology is the Infiniti M35h [41].

A parallel hybrid architecture is defined as having two (or more) power sources that are connected mechanically, via a "torque bus" [39]. This is in contrast to the DC bus in the series hybrid configuration.

One or more clutches are often required to implement this type of powertrain architecture. If the vehicle is in EV mode, the ICE would be switched off and disconnected from the torque bus (via an open clutch between the ICE and the EM). If the vehicle is at rest, the ICE can be run to charge the battery. In this instance, the transmission must be disconnected from the torque bus (via an open clutch upstream of the transmission).

However, depending on the vehicle class and design requirements, the battery and EM could potentially be replaced with a mechanical flywheel [4], thus forming a new topology within the parallel hybrid architecture. This is shown in Figure 11. The mechanical flywheel system also contains a CVT to provide step-less torque arbitration between the flywheel and the drivetrain, and a clutch to disengage the system, for example when the vehicle is stationary. The CVT and clutch could also potentially be replaced by an Infinitely Variable Transmission (IVT) [42]. The IVT offers the ability to have a "geared neutral", thus decoupling torque transfer between the input and output shafts without the use of a clutch.

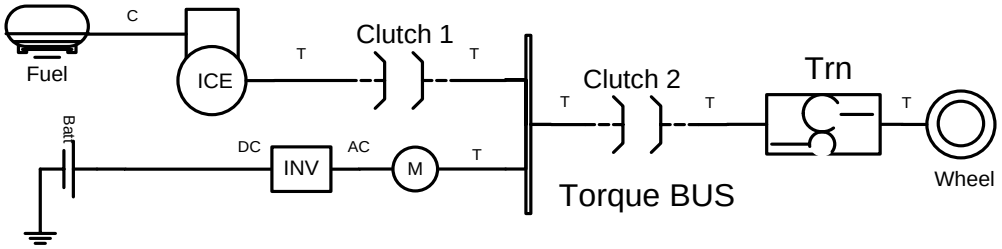


**Figure 10: Petrol-electric parallel hybrid powertrain topology**

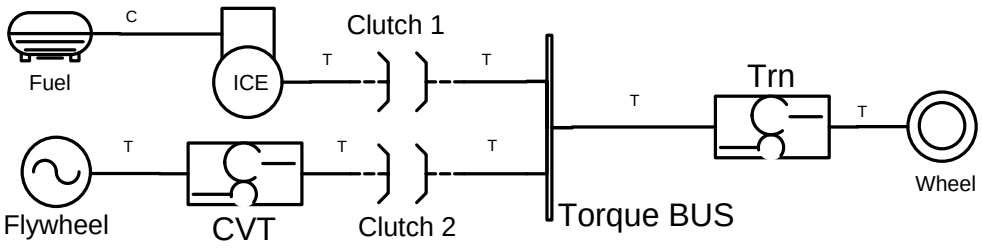


**Figure 11: Flywheel-based mechanical hybrid powertrain**

### 2.2.4 Compound Hybrid Architecture

The compound hybrid architecture is sometimes referred to as a series-parallel architecture, because of its ability to emulate both layouts. This architecture contains two (or more) power sources that are connected both mechanically and electrically. In most instances there is one DC bus and one (or more) torque bus.

Famous examples of the compound hybrid architecture include the Toyota Prius [43], and more recently, the Chevrolet Volt [44]. In the Toyota Prius, the core of the system comprises of a planetary gearset, which has three input/output shafts. The ICE is connected to the first shaft, and an EM (acting like a generator by directing ICE power into the battery) is connected to the second shaft. The third shaft is connected to the wheels together with a second EM, which propels the vehicle. This configuration is presented in Figure 12, where the torque bus on the left represents the power split device. In high demand scenarios both EMs can generate positive drive torque.

Another potential compound hybrid topology is shown in Figure 13. This layout is similar to the Toyota system, but only utilises one EM, and includes a CVT and a clutch to completely decouple the ICE from the rest of the powertrain. The energy storages comprise of a battery and ultracapacitor to buffer the electrical power. A similar system was also proposed by Salisa *et al.* as the UTS PHEV [11].

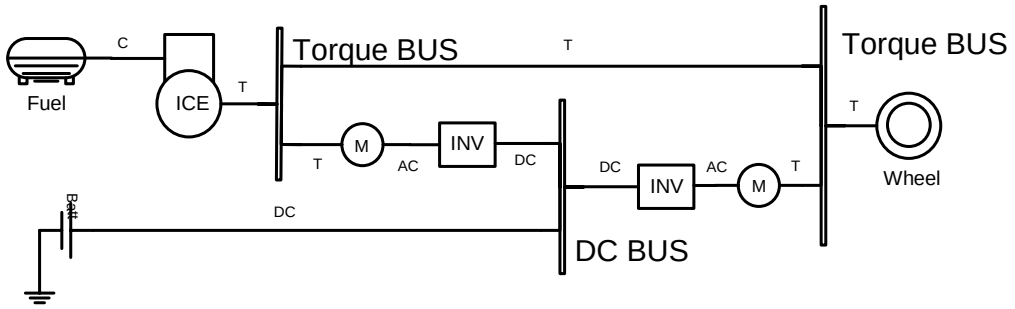


**Figure 12: Compound hybrid topology used by Toyota Prius**

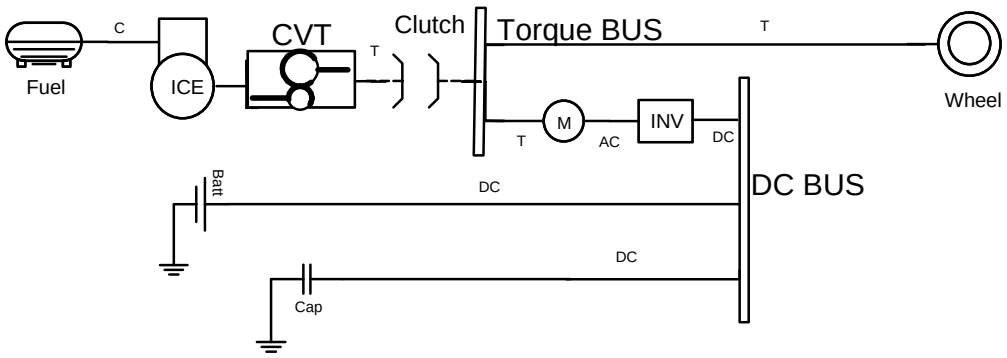


**Figure 13: An alternative compound hybrid topology**

### 2.2.5 Powertrain Mass

The mass of a hybrid powertrain will depend, among other factors, on its topology. For example, in a series hybrid topology, the EM has to be designed for peak power and the generator designed for peak ICE power [2]. Hence, this could potentially increase the mass of the system due to the need for a larger EM and ICE, for example.

Conversely, the size of the ICE and EM could be made smaller for a similar vehicle with a parallel hybrid topology, as both these components work in tandem to provide peak power [2]. Hence parallel hybrid could potentially offer weight savings over a series hybrid topology.

Powertrain mass contributes to the overall vehicle weight, and plays a vital role in fuel and energy consumption [45]. From a 1$^{st}$ order of approximation point of view, Miller and Nicastri estimates that an extra 50kg of vehicle mass is equivalent to 100W of power losses [46].

## 2.3 Defining Performance Criteria

Performance criteria provide a systematic and objective approach to comparing different hybrid powertrain topologies. It enables powertrain topologies to be compared based on criteria that are defined by vehicle class and usage profile. As a result, this potentially enables powertrain topologies to optimised for a given vehicle application.

The following criteria have been used in literature for powertrain optimisation:

- Fuel economy and emissions [47]
- Powertrain mass [48; 49]
- Estimated powertrain costs [50; 51]
- Longitudinal acceleration performance [15; 50]

Fuel economy and emissions is a major driver for pushing alternative powertrain technologies. This is compounded by the rising costs in fuel and increased concern of global warming caused by $CO_2$ emissions. In tandem with alternative powertrains, lowering the overall vehicle mass also aids in reducing emissions. Amongst the approaches that are being used to reduce vehicle mass includes using lighter materials, such as aluminium and composites. However, as the focus of this research is specific to powertrains, the investigation will be on optimising the powertrain to minimise its mass.

There would also appear to be a trade-off between lowering emissions and powertrain costs; for example, EVs, which have lower tailpipe emissions when compared to CVs, are more expensive to manufacture. Therefore, this area will be investigated to identify such trade-offs.

These performance criteria will form the basis of the cost functions and the constraints used in the powertrain optimisation routine, as demonstrated by way of case studies in the upcoming chapters.

### 2.3.1 Tank-to-wheel Emissions

Tank-to-wheel emissions is a measure of comparing only the tail-pipe emission of the vehicle. This criterion was largely driven by the goal set by the European Automobile Manufacturers Association (ACEA) with the European Commission (EC) in 1998. This goal called for manufacturers to produce more fuel-efficient and lower emission vehicles. They voluntarily agreed to limit the fleet specific $CO_2$ emission produced by new passenger vehicles to 140g $CO_2$/km by 2008 [52].

Additionally, EU $CO_2$ targets are predicted to drive a dramatic shift in the types of powertrain produced over the next decade [53]. In the short term, a new European (EU) fleet average target for less than 130g/km of $CO_2$ emission has been set for all new vehicles produced after 2015, as per the ACEA agreement [52]. This is a further 7% reduction from the 2008 levels. Hence, it can be assumed that tank-to-wheel emission performance will be a growing concern and therefore of high importance to compare various powertrain topologies. Additionally, if the fleet average $CO_2$ emissions of a manufacturer exceeds this limit, a penalty is imposed on the excess emissions for each car registered. This penalty amounts to a premium of €5 for the first g/km that is exceeded, €15 for the second g/km, €25 for the third g/km, and €95 for each subsequent g/km thereafter. From 2019, the cost will increase to a flat rate of €95 for every g/km exceeded.

There are also additional incentives given to manufacturers that to produce vehicles with extremely low emissions (below 50g/km). Each low-emitting car will be counted as 3.5 vehicles in 2012 and 2013, 2.5 in 2014, 1.5 vehicles in 2015 and then 1 vehicle from 2016 to 2019. This approach will help manufacturers further reduce the average emissions of their new car fleet [54].

### 2.3.2 Well-to-wheel Emissions

The tank-to-wheel analysis is a subset of the well-to-wheel analysis, which is used to determine the energy consumption and greenhouse gas (GHG) emission of a system [28]. The "system" is defined as every stage involved from fuel production (''well'') to its end use in a vehicle (''wheel''). Well-to-wheel studies in general form the basis for assessing the impacts of future fuel and powertrain options, particularly in terms of energy use and greenhouse gas emissions [28]. In order to assess the well-to-wheel $CO_2$ emissions of various powertrain topologies, it is necessary to consider $CO_2$ emissions associated with production of the fuel/source of energy (well-to-tank).

One example of well-to-wheel $CO_2$ emission for various energy sources is summarised in Table 3. In this table, each energy source is paired with its respective powertrain type, such as CV, EV, and Fuel Cell EV (FCEV). Offer *et al.* estimated hydrogen $CO_2$ emissions to be 76.9g $CO_2$ $MJ^{-1}$, based upon a value of 11 $kgCO_2$ $kgH_2^{-1}$ for steam reforming natural gas and a calorific value of 143MJ $kgH_2^{-1}$ [10]. Electricity $CO_2$ emissions are assumed to be 150 $gCO_2$ $MJ^{-1}$ based upon the 2008 UK average electricity emissions of 540 $gCO_2$ $kWh^{-1}$, which included 5.5% of electricity generation from renewable sources [10] (in 2011, this figure was increased to 594 $gCO_2$ $kWh^{-1}$, according the Department for Environment, Food and Rural Affairs (DEFRA), a public UK body [55]). Well-to-tank conversion factor for petrol is 14.10 $gCO_2$/MJ [55].

The vehicle type used in the example shown in Table 3 is assumed to be a "medium vehicle" as defined by the National Travel Survey (NTS) [56]. After completing a drivecycle, the amount of electrical energy consumed by an EV or PHEV is determined by replenishing the charge in the battery back to its initial state from the electric grid. Subsequently, the amount of well-to-wheel $CO_2$ emitted is then calculated by converting this consumed electrical energy into gram-$CO_2$ using the data published by DEFRA. For a PHEV, its well-to-wheel $CO_2$ output combines emissions from both its electrical and fossil fuel energy sources.

The purpose of this example is to clarify distinctions and significance of the well-to-tank, tank-to-wheel, and well-to-wheel $CO_2$ emissions. The vehicle type is used to serve as an illustration, and won't be used any further in this thesis.

It ought to be mentioned that this estimate does not include the following:

- emissions from construction and decommissioning of the infrastructure that is used to create and process the fuel
- emissions that result from commissioning and decommissioning of the electrical power plant, transmission lines, and charging station [57]
- manufacture and end-of-life disposal of the powertrain components within the vehicle.

These factors, although important, are considered beyond the scope of this research.

**Table 3: Example of well-to-wheel $CO_2$ emissions for each fuel type (adapted from** [10]**)**

| Powertrain Type | **CV** | **FCEV** | **EV** |
|---|---|---|---|
| Energy Source | **Petrol** | **Hydrogen** | **Electricity** |
| Well-to-tank emissions / $gCO_2\ MJ^{-1}$ | 14.1 | 76.9 | 150 |
| Tank-to-wheel emissions / $gCO_2\ MJ^{-1}$ | 77.6 | - | - |
| Well-to-wheel emissions / $gCO_2\ MJ^{-1}$ | 91.7 | 76.9 | 150 |
| Given fuel consumption / $MJ\ mile^{-1}$ | 2.93 | 1.46 | 0.73 |
| Well-to-wheel emissions / $gCO_2\ mile^{-1}$ | 267 | 112 | 110 |
| Well-to-wheel emissions / $gCO_2\ km^{-1}$ | 167 | 70 | 68 |

## 2.4 Review of Powertrain Simulation Tools

To evaluate the performance of the powertrain architectures, modelling and simulation tools are indispensable. This is particularly true as prototyping and testing each design combination is cumbersome, expensive, and time consuming [26]. New hybrid powertrain configurations and controllers are also continuously being developed, thus the ability to simulate a powertrain before prototyping is important.

Simulating vehicle powertrain requires dedicated simulation software [26]. To that end, this research was inspired by the work carried out by Argonne Labs and the National Renewable Energy Laboratory (NREL) in the area of powertrain simulation and optimisation. Advanced powertrain researches from these two institutes have resulted in the creation of two simulation tools respectively; PSAT (PNGV System Analysis Toolkit) and ADVISOR (Advanced Vehicle Simulator)

Both tools have been frequently cited in literature for the purpose of system-level powertrain simulation and optimisation. Other powertrain simulation tools such as AVL Boost and GT-Suite are also available; however they have been noted to be more suited for simulation of detailed ICE attributes with the expense of greater computational time [58-60]. This includes the simulation of combustion mechanisms, exhaust after-treatment systems, and acoustics, which are not the intent of this research.

There are fundamental differences in the approach used by PSAT and ADVISOR; the former uses forward-facing models [61], whilst the latter uses a hybrid approach. In ADVISOR, the models are primarily backward-facing, with forward-facing methods only active when component performance limits are encountered; when they are not, ADVISOR operates strictly as a backward-facing model [32]. Another proponent of the backward-facing modelling method is the QSS toolbox, developed at ETH Zurich by a

team led by Lino Guzzella [27; 31; 62]. Unlike ADVISOR, the QSS toolbox is strictly backward-facing only.

Table 4 shows a list of reviewed publications that have used these simulation tools for the purpose of powertrain size optimisation. This table summarises the simulation tools employed and the types of powertrains that were analysed. Findings revealed that each simulation tool has a modular approach to powertrain modelling, and therefore provided the flexibility of simulating a wide variety of topologies. This literature survey also gave insights to the functional aspects of each simulation toolbox, which will be discussed further.

The development of PSAT was backed by the U.S. government [30] for the PNGV (Partnership for a New Generation of Vehicles) initiative. This initiative included a comprehensive forward-facing HEV simulation environment developed by a consortium of three U.S. automotive manufacturers: Ford, GM, and Daimler-Chrysler [61]. One fundamental strength of PSAT is the fact that it features modular implementation of powertrain components within a powertrain architecture. This provides the flexibility to scale the powertrain components, as well as replacing the models with different model blocks (such as proprietary blocks) if the need arises. This was made possible by strong reference to "power bonds" as seen in Bond Graph modelling techniques [63; 64].

In comparison, ADVISOR is a hybrid vehicle simulator which incorporates both forward-facing and backward-facing methods. ADVISOR compares the required values (backwards-facing results), with achievable values (forward-facing results). Nevertheless, this approach requires the definition of two models for each powertrain component, leading to larger programming overheads for introducing new components [65]. Finally, the QSS toolbox is a fully backward-facing model, and is capable of utilising a relatively larger time-step, generally in the order of 1 second.

Similar to PSAT, both ADVISOR and the QSS toolbox also follow a modular approach. The user can alter both the model inside the block as well as the MATLAB m-files associated with the block to suit their modelling needs. For example, the user may need a more precise model for the electric motor subsystem [26]. A different model can replace the existing model as long as the inputs and the outputs are the same. On the other hand, the user may leave the model intact and only change the MATLAB m-file associated with the block diagram. This is akin to choosing a different manufacturer of the same powertrain component. Therefore, all three software packages provide modelling flexibility for the user.

**Table 4: Review of utilisation of powertrain simulation software in literature**

| | References | | | | | | | | |
|---|---|---|---|---|---|---|---|---|---|
| | [49] | [66] | [67] | [68] | [69] | [27] | [70] | [71] | [72] |
| **ADVISOR** | | * | * | | * | | * | | * |
| **PSAT** | * | | | * | | | | * | |
| **QSS Toolbox** | | | | | | * | | | * |
| Single source | | | | | | * | * | | |
| Series Hybrid | | * | * | | | * | | * | * |
| Parallel Hybrid | * | | * | * | * | | | | * |
| Compound Hybrid | | | * | | | | | | * |
| CV | | | | | | * | * | | |
| HEV/PHEV | * | | * | * | * | | | * | * |
| HEV – Fuel Cell | | * | | | | * | | * | |

An example of component modularity was described by Assanis *et al.*, who used ADVISOR for simulating a hybrid powertrain, but required a customised engine model instead of the one supplied by ADVISOR. Because of its modularity, they could swap the engine module with one of their own, which included a higher fidelity turbocharged model. In contrast, if ADVISOR were to have a fixed list of components, it may cause some difficulties for the design engineer who desires to evaluate the impact of using a different, non-existing component, or wants to continuously vary component sizes in search for an optimum combination.

In addition to being modular, the powertrain components within ADVISOR are scalable. This was achieved by including routines that allow variation of component size through scaling of maps [30]. ADVISOR also follows an open-source model, and thus receives support from the industry and academia to validate and improve the model database [32]. Several publications have also used ADVISOR for powertrain simulation and validated its results favourably against real-world experiments [67; 73; 74], and ADVISOR itself has been used as a source for validation [75].

The key similarity in all three simulation tools is that they use MATLAB and Simulink as their underpinnings to run the simulations. According to Wipke *et al.*, MATLAB and Simulink were chosen for their nearly self-documenting graphical programming environment and their wide acceptance by researchers in academia and industry [32].

However, though modular, the powertrain architecture in all three simulations tools was fixed during simulation. As a result, trying to compare the results from optimising different powertrain architectures, such as a pure EV with a PHEV, would require running two sets of optimisations separately. This is because the structure of the powertrain architecture is fixed during the optimisation run. For example, ADVISOR requires reconfiguration when comparing series and parallel hybrid, as shown by Same *et al.* [38] for optimising a Formula Student vehicle.

A similar modular powertrain simulation tool with aggregated powertrain components was developed by Imperial College London in 2002 [65]. It also compares a few other backward-facing simulation tools, and mentioned that one common trait of these tools were the fixed powertrain layouts. This meant that each powertrain type had to be optimised individually. The paper above also mentions the importance of powertrain component modularisation for the purpose of comparing different powertrain architectures, thus strengthening the aims of this research.

## 2.5 Chapter Discussions and Conclusions

The ability to compare multiple types of powertrain is important because a significant number of advanced vehicle configurations are available. Because of time and money constraints, it is impossible to build and test every one of these configurations. In addition, for each configuration, users need to be able to choose among different component models. To be able to make the right decisions, practitioners would benefit from a flexible simulation tool that allows for easier manipulation of different powertrain architectures and component size optimisations.

Additionally, literature survey has indicated that there are no tools at present that has the ability to simultaneously select the most appropriate powertrain architecture from a list of components, and then optimising the size of the components within the architecture, for a given cost function. Therefore, to pursue the creation of a better methodology for comparing different powertrain architectures, a simulation toolbox will be created as part of this research.

It has been identified that there are two methods for carrying out vehicle powertrain modelling: forward-facing and backward-facing models. Based on the literature, it is deduced that forward-facing models are is computationally more costly due to the need for smaller time-steps and higher order integration, and could be an issue in the context of iterative optimisation runs.

Modularity is important because this toolbox will need to offer the flexibility for completely defining the layout of the powertrain configuration. One approach to this can be seen by Hofman *et al.* [33], who described the usage of the QSS toolbox and ADVISOR for the purpose of comparative analysis of three types of hybrid powertrain;

series, parallel and series-parallel, albeit running three independent simulations for achieving those results.

Practitioners, who will ultimately use the toolbox developed in this research, will have specific requirements. Thus, the proposed toolbox will need to have an open architecture and provide availability of source code to allow a significant amount of customisation. Users can replace the existing component models with more detailed models if necessary. Additionally, using MATLAB/Simulink as the backbone makes it possible to link to other software packages for component models [64]. Proprietary models can be compiled and linked to Simulink to protect intellectual property.

A deeper understanding of powertrains at the component level will need to be achieved. Therefore, discussions on fundamental understanding and underlying equations of the powertrain components will be carried out in the next chapter.

Finally, it is important to reiterate that this proposed tool is used to obtain a first-hand approximation for the type of powertrain that is most likely suitable or a given vehicle type and duty cycle. Thus, this research aims to produce a tool suitable for powertrain analysis, rather than specific powertrain design. It can be used to predict measures such as fuel consumption and emissions; however, it cannot be used to study details that require smaller time-steps, such as vibrations and NVH. Nevertheless, based on the results of the simulation using this tool, practitioners can then incorporate the findings into more appropriate simulation software to pursue such investigations.

Therefore, based on the finding of the literature survey, the aims of this research will be directed towards the following:

- Develop a toolbox, which contains a novel methodology that combines both powertrain topology and component size optimisations
- Utilise this toolbox to carry out novel comparative investigations, such as multi-objective optimisations for identifying trade-offs between cost functions by way of powertrain topology selection.

# 3 MODEL DEVELOPMENT

The previous chapter covered several simulations tools that are used for the purpose of powertrain simulation and optimisation. This chapter uses those findings to proceed with creating the powertrain component models, which will then be utilised in the forthcoming chapters for demonstrating the workings of the proposed methodology. The motivations behind developing the models in-house were two-folds; it enabled understanding of fundamental principles in powertrain modelling and it provided the flexibility to implement the models more intrinsically within the proposed powertrain optimisation algorithms.

The models will be created in the MATLAB/Simulink environment, consistent with the modelling environment that were utilised by the commercial powertrain simulation tools discussed in the previous chapter. To address the hypothesis set forth in the introduction, this research will focus on developing a methodology that facilitates the comparative analysis of multiple powertrain architectures. The powertrain component models that are described in this chapter will be used to illustrate the workings of this methodology. Additionally, the use of uniform power-based interface between the models will allow for flexibility in incorporating other types of powertrain components that are not described here, such as different battery chemistries or different types of ICEs.

To enable powertrain architectures to be categorised as shown in Section 2.2, the powertrain components will be modular in implementation, in order to allow for interchangeability across different topologies. To allow such levels of interchange-ability, it is determined that the communication between each energy storage and energy converter device also has to be standardised. This is achieved using power bonds, similar to the concept of bond graphs [76]. The Modular Powertrain Structure (MPS), which then facilitates the interchangeability between powertrain components, is discussed further in Chapter 4. In addition to being modular, the powertrain models will also need to be scalable and have sufficient fidelity to capture the efficiency and operating envelops of the respective powertrain component.

Therefore, each powertrain component is treated as a module and is designed to be both modular and scalable in implementation, an example of which was shown by Mason *et al.* [77]. Methodology for sizing powertrain components as a part of an optimisation routine has been covered in literature [66; 78], and a similar approach will be employed in this research.

Powertrain components can be divided into three main categories [62]; energy storage, energy converter, and power transformers. The fundamental understanding and underlying equations of the powertrain models will be discussed in the rest of this chapter.

## 3.1 Energy Converters

Energy converters are defined as devices that convert energy form one domain to another [62]. One such example is the ICE, which converts chemical energy from fossil fuel into mechanical energy, heat, and noise. The following energy converters will be investigated in more detail:

- Internal Combustion Engines
- Electrical Machines
- Auxiliary Power Unit.

This list of powertrain components has been narrowed down based on the availability and quality of data gathered from literature and work carried out by Cranfield University for the following funded projects:

- Low Carbon Vehicle Technology Project (LCVTP) [40]
- Smart Move Electric Vehicle Trial conducted by Cenex [79]
- FUTURE Vehicle consortium (EPSRC grant number EP/I038586/1).

### 3.1.1 Internal Combustion Engines

The EU states that the ICE will remain as a significant feature of road transport for the foreseeable future [80; 81]. For this research, the aim of this model is to be scalable and sufficiently capture the operation and efficiency envelopes of an ICE. Developing a scalable ICE model, however, was challenging due to myriad of possible variations. In this research, a baseline ICE model that is naturally aspirated and spark ignited was selected, as it is widely available on the market today [28; 82]. Other configurations, such as forced induction and compression-ignited ICEs are possible; however they were not investigated further due to lack of experimental data. Nevertheless, as mentioned previously, the modular approach for the interface between powertrain models will allow practitioners to add further variations of ICEs as required.

In the previous chapter, it was discussed that commercial software such as ADVISOR and PSAT give the option of scaling the powertrain components. In the case of the ICE, this was achieved by way of scaling the efficiency map and inertia of the engine. According to Bohac *et al.* [83], there are variations in the level of fidelity that can be applied to creating the scalable ICE model. In this research, the Willans ICE model, as proposed by Guzzella [62] and Rizzoni [31] was utilised. This approach was chosen because of the simplified formulations of the dependency of ICE efficiency, $\eta_e$ with its rotation speed, $\omega_e$, and output torque, $T_e$. The variables $T_e$ and $\omega_e$ have a clear physical interpretation, which is suitable for the modular approach of creating the ICE model. Nevertheless, their range also depends on the type and size of the ICE that is modelled. Therefore, the normalised variables described below will allow the ICE size to be used

as an optimisation parameter. The background behind the Willans ICE model lies in the assumption that the piston mean effective pressure, $p_{me}$, and the mean piston speed, $c_m$, are similar for a given ICE type (in this case naturally aspirated and spark ignited). Table 5 shows the terms used as part of the calculation for engine power and instantaneous fuel consumption.

**Table 5: Terms used for ICE calculations**

| Term | Definition | Units |
|---|---|---|
| $p_{me}$ | Piston mean effective pressure | $N/m^2$ |
| $p_{mf}$ | Fuel mean effective pressure | $N/m^2$ |
| $p_{loss}$ | Mean mechanical losses pressure | $N/m^2$ |
| $c_m$ | Mean piston speed | m/s |
| $T_e$ | Engine torque | Nm |
| $\omega_e$ | Engine speed | rad/s |
| $\eta_e$ | Overall engine efficiency | - |
| $e$ | Thermodynamic efficiency | - |
| $S$ | Piston stroke length | m |
| $N_{stroke}$ | Combustion cycle type (2/4 stroke) | - |
| $V_d$ | Engine displacement | $m^3$ |
| $\dot{m}_{fuel}$ | Fuel mass flow rate | kg/s |

Equations relating $p_{me}$ and $c_m$ with ICE torque $T_e$ and ICE speed $\omega_e$ are given in equations (3-1) and (3-2) respectively.

$$p_{me} = \frac{N_{stroke} \cdot \pi}{V_d} \cdot T_e \quad \textbf{(3-1)}$$

$$c_m = \frac{S}{\pi} \cdot \omega_e \quad \textbf{(3-2)}$$

For a given mechanical power output ($T_e \cdot \omega_e$) we can then calculate the fuel power ($P_{fuel}$) delivered for an overall engine efficiency of $\eta_e$, with equation (3-3).

$$P_{fuel} = \frac{T_e \cdot \omega_e}{\eta_e} \tag{3-3}$$

To rewrite equation (3-3) in terms of mean pressures, $\eta_e$ can be rewritten as equation (3-4), where $p_{me}$ is the mean effective pressure output per cylinder, and $p_{mf}$ is the input fuel mean effective pressure per cylinder.

$$\eta_e = \frac{p_{me}}{p_{mf}} \tag{3-4}$$

The term $p_{me}$ was calculated in equation (3-1). To calculate the value of $p_{mf}$, the thermodynamic efficiency, $e$, and the mechanical losses, $p_{loss}$, are used in equation (3-5). Both these terms are expressed in terms of mean piston speed, $c_m$, shown in Figure 14. These values were obtained experimentally to capture the efficiency of the ICE at various operating points [62]; however, it ought to be mentioned that it is sourced from a particular engine, and will be used to demonstrate the workings of the proposed toolbox in the subsequent chapters. The applicability of this measurement for scaling into different engine sizes are demonstrated in Section 3.1.1.1. The relationship between mean piston speed and engine speed was given in equation (3-2).

$$p_{mf} = \frac{p_{me} + p_{loss}}{e} \tag{3-5}$$

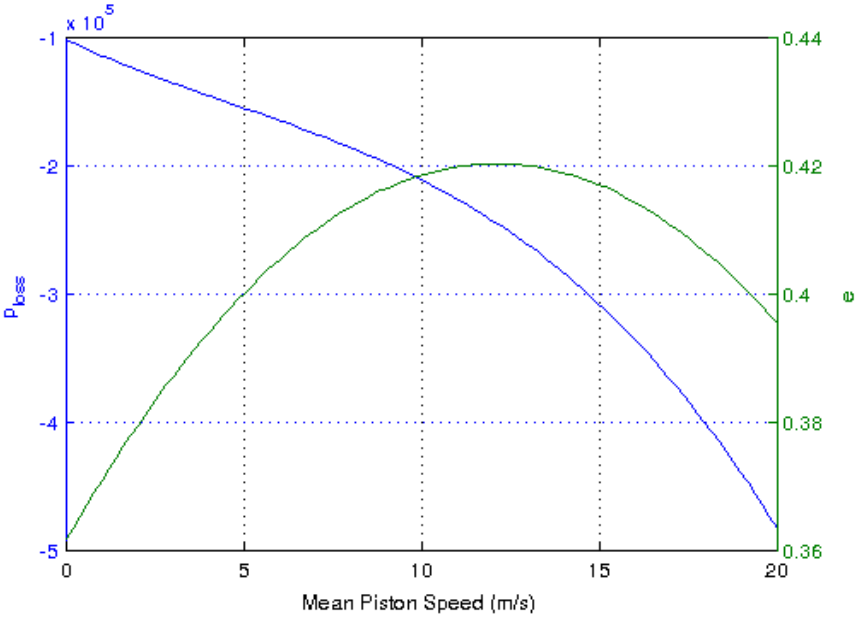


**Figure 14: Estimated thermodynamic efficiency ($e$) and mechanical losses ($p_{loss}$) as a function of mean piston speed ($c_m$)**

After calculating $\eta_e$, $P_{fuel}$ was then calculated based on equation (3-3). Finally, the mass flow rate of the fuel, $\dot{m}_{fuel}$, is simply given as,

$$\dot{m}_{fuel} = \frac{P_{fuel}}{H_l} \tag{3-6}$$

where $H_l$ is the fuel's lower heating value. The total fuel used in a drivecycle is the integration of $\dot{m}_f$ over time, and this calculation will be carried out in the fuel tank model, described later in Section 3.2.1.

Figure 15 shows the efficiency $\eta_e$ of the engine for various values of $p_{me}$ and $c_m$. Figure 16 shows the fuel map for the ICE model with a 1 litre displacement as an example.

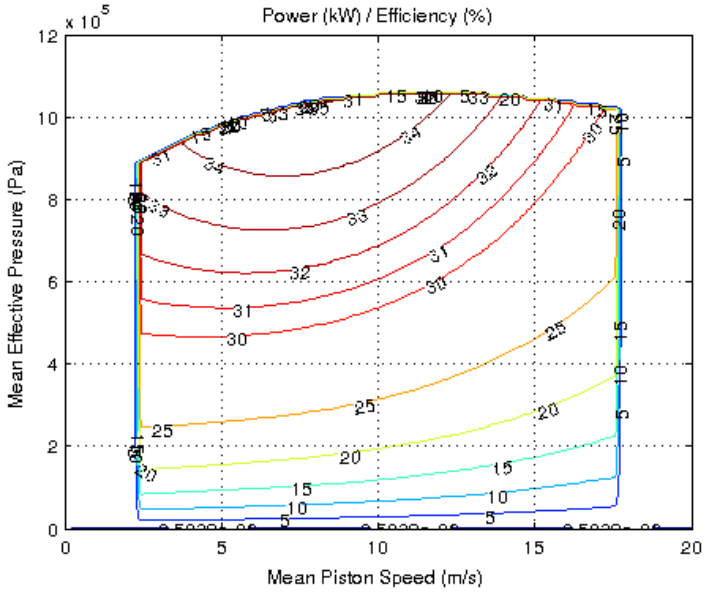


**Figure 15: Efficiency of the Engine based on $p_{me}$ and $c_m$**

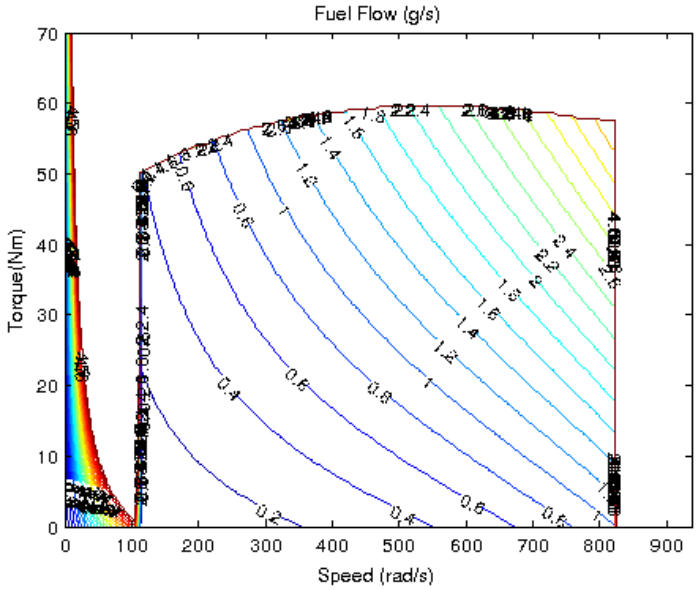


**Figure 16: Fuel flow map as a function of ICE torque and speed**

#### 3.1.1.1 ICE Scaling and Verification

During the optimisation, the required ICE power is determined by specifying the engine displacement variable, $V_d$. The resultant mass of the engine is then calculated based on the work by Guzzella and Sciarretta [62], where a mass-to-displacement ratio of 67.6kg/l was suggested. As mentioned previously, the data used to create the scalable ICE model is sourced from a particular engine type [62]; therefore, to verify its validity, it was compared to the fuel consumption of two vehicles that were made available to this research; the Smart ED and the Jaguar XJ. The ICE model was first verified by connecting it to the existing Smart ED vehicle model (described in Section 3.1.2.4), and then comparing the simulated fuel consumption with published data. To accomplish this, the EV powertrain was replaced with the ICE engine and conventional transmission. The transmission ratios are listed in Appendix C.2. The simulation was run using the New European Driving Cycle (NEDC), which is the same cycle used to carry out the tests for the official emissions figures. Therefore, the shift schedule of the transmissions was based on the shift point defined on the NEDC [84] and shown in Figure 31.

Based on the simulation, the fuel consumption was 5.49 L/100km. The manufacturer's published data for the Smart Fortwo is 5.64 L/100km, or 3% greater than the simulated value [85]. Similarly, another test was performed using the Jaguar XJ, which was the vehicle used as a case study for the LCVTP project. The vehicle data and transmission ratios are shown in Appendix C for the Jaguar XJ. The NEDC was again used in this test. Based on the simulated data, the fuel consumption was 12.1 L/100km, whist the published data was 11.3 L/100km [86], or about 6.6% lower than the simulated model. This discrepancy was attributed primarily to the following:

- variation between the assumed efficiency of the Willans ICE model and the ICE used in the Jaguar XJ (5.0L).
- assumption that the combustion constantly occurs at the stoichiometric ratio
- Extra loads from ancillaries on the actual vehicle that were not considered.

Nevertheless, as the focus of this research is not specific to detailed engine modelling, the scalable Willans line engine model was deemed sufficient for the purpose of demonstrating the functionality of the proposed methodology. Additionally, future work may wish to investigate on incorporating models that have more elaborate scaling functions.

### 3.1.2 Electrical Machines

The EM is the only energy converter in this research that has reversible power flow. EMs are becoming a very common feature in the automotive industry and come in several types [87; 88]. The most common type of EM for vehicle traction applications is the Permanent Magnet (PM) brushless DC [89]. The other types of EM that are used for traction applications include the induction motor and the switched reluctance motor [90]. Each type of EM can be described by its dynamic response, its subsystem limits (power, torque, or speed) and efficiency.

The EM is modelled based on a speed-torque curve, which defines its power and efficiency. The EM model was developed using data obtained from a Smart ED electric vehicle, as part of the Smart Move Electric Vehicle Trial [79]. A cut-away model of the Smart ED is shown in Figure 17, and technical specifications in Table 6. The powertrain of the Smart ED consists of a 16.5kWh Lithium-Ion Battery, which has a peak power rating of 30kW, and an EM with a peak power rating of 55kW and continuous power rating of 42.5kW. However, the peak power of the overall powertrain is limited to 30kW.

The goal of the EM model was to be scalable to meet varying power demands. The EM is a PM brushless DC type, and its model is based on data provided by Zytek Automotive [91], who supplies the EM for the Smart ED.

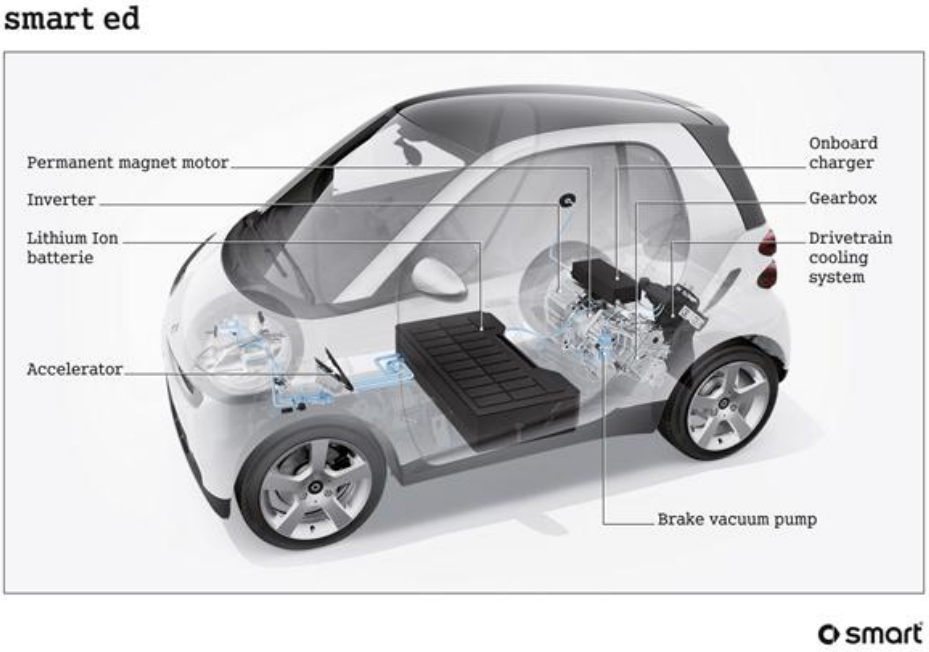


**Figure 17: The Smart Electric Drive (ED)** [92]

**Table 6: Data from the Smart ED**

| | |
|---|---|
| Make | Smart (Mercedes-Benz) |
| Model | Fortwo ED (Electric Drive) |
| Electrical Machine | Zytek Automotive 55kW (limited to 30kW propulsion, 10kW regenerative braking) |
| Battery Pack | 16.5 kWh Li-ion (Panasonic NCR18650 cells) |
| Top Speed | 27.7 m/s (62 miles/hour) |
| Weight | 965 kg unladen weight |
| Range | 135 km (NEDC Drivecycle) |

#### 3.1.2.1 The Smart ED

The Smart ED was made available to Cranfield University during participation in the Smart Move Trial programme, which is managed by Cenex (the UK's Centre of Excellence for low carbon and fuel cell technologies) and funded by the UK Department for Business, Innovation and Skills (BIS).

The Smart ED was fitted with an on-board CAN logger that recorded the activities of the car. Data harvested from the CAN logger gave opportunities for analysing the performance of the EV in real-world usage, and provided information that is valuable for the purpose of this research.

When the vehicle is being driven, key parameters are automatically recorded from the CAN bus and uploaded to a central database for analysis. Amongst the key parameters used in this study are vehicle speed, EM speed, EM torque, battery voltage, and battery current.

The CAN logger has a sampling rate of 1 Hz. Recording of data is initiated as soon as the ignition key is switched on. Unfortunately, the sampling rate is fixed; therefore, it was not possible to increase the resolution of the data. However, drivecycles like the NEDC and ARTEMIS were also formulated based on sampling frequencies of 1 Hz [93]. Hence, it has been assumed that the data sampling rate is acceptable for the purpose of this research. The logged data on the vehicle is stored as Comma Separated Values (CSV) files. The CSV files were then imported into MATLAB for analysis.

A schematic of the locations where some of the parameters are recorded on the vehicle is given in Figure 18. Each recorded parameter is assigned a channel number (shown in parentheses). A summary of the channel numbers and associated parameters captured

by the CAN logger is given in Table 7 [94]. Some of the parameters are directly measured by sensors whilst others are calculated by the on-board ECU. The CAN logger also has an inbuilt GPS system which records the GPS coordinates of the vehicle.

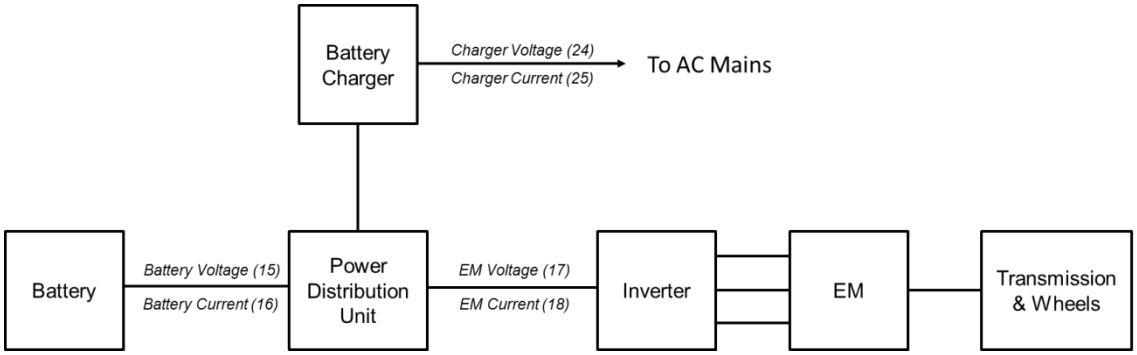


**Figure 18: Location of measurement points for electrical voltages and currents**

The electrical currents and voltages were measured at three different points on the drivetrain. Figure 18 shows the points where they were measured. These measurements were then used to calculate the electrical power at these points.

For calculating the battery power, the electrical current and voltage was measured at the battery terminals, where it connects to the high-voltage DC bus. It is the product of Battery Current (Table 7, channel 16) and Battery voltage (Table 7, channel 15). Similarly, the EM power was measured at the input side of the inverter terminals of the DC bus. It is the product of Motor Current (Table 7, channel 18) and Motor Voltage (Table 7, channel 17).

**Table 7: List of channels and parameters captured by CAN logger**

| | Parameter | Unit | Description |
|---|---|---|---|
| 1 | Segment ID | | |
| 2 | IMEI | | International Mobile Equipment Identity number used to identify GSM device in logger |
| 3 | Time | | YYYY-MM-DD HH:MM:SS |
| 4 | Interval | secs | Time interval between current and previous point |
| 5 | Latitude | deg | Decimal degree. Northern hemisphere is positive |
| 6 | Longitude | deg | Decimal degree. Eastern hemisphere is positive |
| 7 | Altitude | m | Height above mean sea level in meters |
| 8 | Ignition | 0/1 | Ignition status 0 = Off 1 = On |
| 9 | Temperature | deg C | Ambient temperature |
| 10 | Speed | kph | Vehicle speed calculated from motor speed |
| 11 | Energy Transferred Key On | kWh | Total energy transferred during battery drive. Starts at key on. Stops at key off |
| 12 | Energy Transferred Charging | kWh | Total energy transferred during charging. Charging started - contactors closed. Charging finished - contactors opened |
| 13 | SOC | % | State of charge of HV battery |
| 14 | Charging Lead | 0/1 | Battery being charged by HV battery charger |
| 15 | Battery Voltage | volts | HV battery voltage as measured by the BMS at the battery HV connection |
| 16 | Battery Current | amps | HV battery current as measured by the BMS at the battery HV connection. Negative current is energy being delivered from the battery |
| 17 | Motor Voltage | volts | HV battery voltage as measured by the drivetrain at the HV connector on the drivetrain |
| 18 | Motor Current | amps | HV battery current as measured by the drivetrain at the HV connector on the drivetrain. This signal includes motor demands and DC-DC converter demands |
| 19 | Drive Battery Temperature | deg C | Maximum temperature within the HV Battery. Accuracy up to a degree |
| 20 | Cooling Request | % | Cooling request from the battery to the EVCM. 0 % = No cooling / 100% = maximum cooling. The cooling of the system is provided by the AC system. |
| 21 | Motor Speed | rpm | Motor speed at measured by the Drivetrain |
| 22 | Motor Torque | Nm | Motor torque as requested from the Drivetrain |
| 23 | Auxiliary Power | kW | Power used for cabin heating/cooling and battery cooling. This includes cabin heating and cooling plus battery cooling demands. |
| 24 | Charger Voltage | volts | AC Mains voltage as measured by the charger |
| 25 | Charger Current | amps | AC Mains current as measured by the charger |

### 3.1.2.2 Obtaining the EM Efficiency Map

The speed, torque, voltage, and current data of the EM were obtained from the Controller Area Network (CAN) interface of the Smart ED, and this data was used to construct an efficiency map for an EM with 30kW peak power. The values of the EM terminal voltage ($U_{L(em)}$), the EM current ($I_{em}$), the rotational velocity of the EM ($\omega_{em}$), and the EM torque demand ($T_{em(dmd)}$) were recorded under a number of different operating conditions during the vehicle evaluation. This data was later verified using a hub dynamometer at the automotive lab in Cranfield University under steady-state conditions. The corresponding CAN messages were listed in Table 7 as channels 17, 18, 21, and 22 respectively.

The vehicle evaluation consisted of a predefined route between Cranfield University and Milton Keynes. The route is shown in Figure 19, where points A and C refer to the start/stop points in Cranfield University, and point B is a checkpoint in Milton Keynes. This route was devised such that a variety of different road types are encountered, including urban, A-road, B-road and motorway sections.

Six volunteers from the Department of Automotive Engineering were asked to drive the Smart ED along this route at two-hour intervals; between 8:00 AM and 6:00 PM. This interval was chosen so that the vehicle would be driven in varying traffic conditions and there is sufficient time to recharge the battery. The total distance logged from this test is 688 km.

To verify the data logged from the real-world tests, the Smart EV was run in speeds between 10km/h and 80km/h (the limits of the dynamometer), in steps of 10 km/h. The road load was replicated by the dynamometer and includes rolling resistance and aerodynamic drag. The data for the road load was provided by Millbrook, which also participated in the Smart Move Trial [79].

The data acquired from the vehicle were used in Equation (3-7) to calculate the efficiency of the electric drive system and build the EM efficiency map, which is shown in Figure 20.

$$\eta_{em} = \frac{T_{em(dmd)} \cdot \omega_{em}}{U_{L(em)} \cdot I_{em}} \quad \textbf{(3-7)}$$

The Smart ED consists of a single stage reduction gearbox coupled to a final drive unit with a combined gear ratio ($\varphi_{gb}$) of 8.67 [94]. The efficiency of this combined unit, $\eta_{gb}$, was estimated to be 0.95, which provided the closest correlation between the measured and simulated EM torque, as shown in Figure 22.

To produce the comparison in Figure 22, the torque of the EM, $T_{em}$, was calculated from $T_w$ using Equation (3-8), where $T_w$ is the torque at the wheels (discussed further in

Section 3.4). Similarly, the EM speed is determined from the wheel speed ($\omega_w$) in Equation (3-9).

$$T_{em} = \frac{T_w}{\eta_{gb} \cdot \varphi_{gb}} \tag{3-8}$$

$$\omega_{em} = \omega_w \cdot \varphi_{gb} \tag{3-9}$$

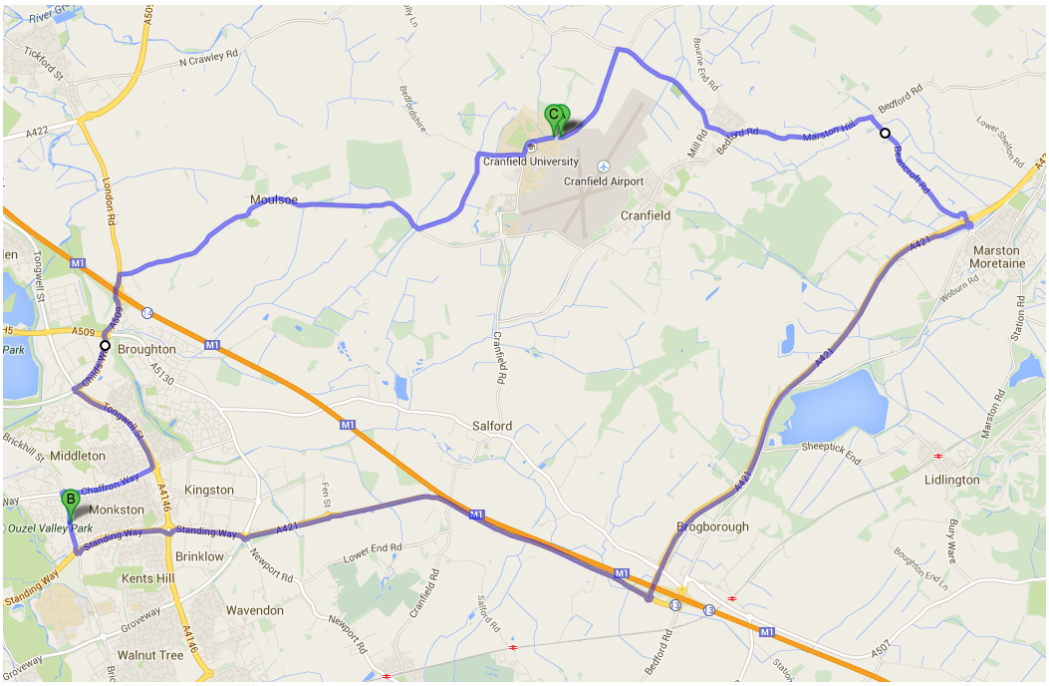


**Figure 19: Route used to record the performance of the EM and battery**

The validity of the gear efficiency is checked by comparing the simulation with the data recorded form the CAN logger. It is noteworthy that the torque data obtained from the CAN logger is the "demand" torque ($T_{em(dmd)}$) sent to the EM, and therefore it is expected to have been filtered when it was recorded.

The efficiency of the EM and its power electronics was combined, similar to the approach by Amrhein and Krein [95]. The combined EM and inverter are represented as an efficiency map and as a function of torque and speed, as shown in Figure 20.

### 3.1.2.3 EM Scaling

As suggested by Guzzella and Sciarretta [62], a similar approach, as used for the ICE, can be applied for the scaling of the EM. Table 8 shows the terms used as part of the EM calculation.

**Table 8: Terms used for EM calculations**

| Term | Definition | Units |
|---|---|---|
| $\omega_{em}$ | EM rotation speed | rad/s |
| $T_{em}$ | EM torque | Nm |
| $\eta_{em}$ | Overall EM efficiency | - |
| $P_{em}$ | EM output power | W |
| $e_{em}$ | Indicated EM efficiency | - |
| $P_0$ | Mechanical and thermal losses | W |
| $p_{me}$ | Equivalent mean effective pressure | $N/m^2$ |
| $p_{ma}$ | Equivalent available mean pressure | $N/m^2$ |

For the EM, the Willans approach take the following form:

$$T_{em} \cdot \omega_{em} = \begin{cases} e_{em} \cdot P_{em} - P_0, & if\ P_{em} > 0 \\ \dfrac{P_{em}}{e_{em}} - P_0, & if\ P_{em} < 0 \end{cases} \quad \textbf{(3-10)}$$

Unlike the ICE, the EM has two separate equations to represent propulsion ($P_{em} > 0$) and power generation ($P_{em} < 0$). For a given EM speed and torque, its overall efficiency can then be calculated as Equation (3-11).

$$\eta_{em}(\omega_{em}, |T_{em}|) = \frac{e_{em} \cdot \omega_{em} \cdot |T_{em}|}{\omega_{em} \cdot |T_{em}| + P_0} \quad \textbf{(3-11)}$$

However, the value of $P_0$ is also deemed to be relatively low compared to the overall power of the EM (less than 1kW for a 32kW permanent magnet EM [62]). Additionally, the EM efficiency, as derived from the data recorded from the vehicle, combines both the efficiency and losses from the EM and inverter. Therefore, it can be approximated that the indicated and overall EM efficiency is comparable in this instance, as shown in Equation (3-12).

$$\eta_{em} \approx e_{em} \quad \textbf{(3-12)}$$

Similar to the ICE, the overall EM efficiency is also a function of the equivalent "mean effective pressure" and "available mean pressure",

$$\eta_{em} = \frac{p_{me}}{p_{ma}} \tag{3-13}$$

where $p_{me}$ in this instance is given as [62],

$$p_{me} = \frac{T_{em}}{2 \cdot V_r} \tag{3-14}$$

while $p_{ma}$ is given as [62],

$$p_{ma} = \frac{P_{em}}{2 \cdot V_r \cdot \omega_{em}} \tag{3-15}$$

By solving Equations (3-10) to (3-15), the following relationship is derived,

$$P_{em} = \begin{cases} T_{em} \cdot \omega_{em} \cdot \eta_{em}, & if\ T_{em} < 0 \\ \dfrac{T_{em} \cdot \omega_{em}}{\eta_{em}}, & if\ T_{em} > 0 \end{cases} \tag{3-16}$$

where for a given EM rotational speed, the increase in EM output power is equal to the increase in EM torque multiplied by its overall efficiency. Therefore, the EM power can be approximately scaled up or down by extending or shortening the torque axis on its efficiency map. The speed axis remains the same, and the efficiency map is extrapolated as required. This approach has been successfully applied in a number of comparable optimisation studies reported in the literature [31; 96]. A case study using this approximation was also verified by Guzzella and Sciarretta ([62], page 91, Figure 4.19) for a permanent magnet EM between a relatively large range from 1kW to 32kW.

The relation between $\omega_{em}$, $T_{em}$ and $\eta_{em}$ is given by the EM efficiency map. Equation (3-17) shows how the maximum torque ($T_{em(max)}$) of the EM can be scaled as a function of the peak power requirements of the powertrain ($P_{em(max)}$), where $T_{em(max)(base)}$ is the maximum torque of the baseline EM (from the Smart ED), as shown in Figure 20. This equation is represented as the EM scaling function, where 30 kW is the maximum power of the baseline EM.

$$T_{em(max)} = T_{em(max)(base)} \cdot \frac{P_{em(max)}}{30{,}000W} \tag{3-17}$$

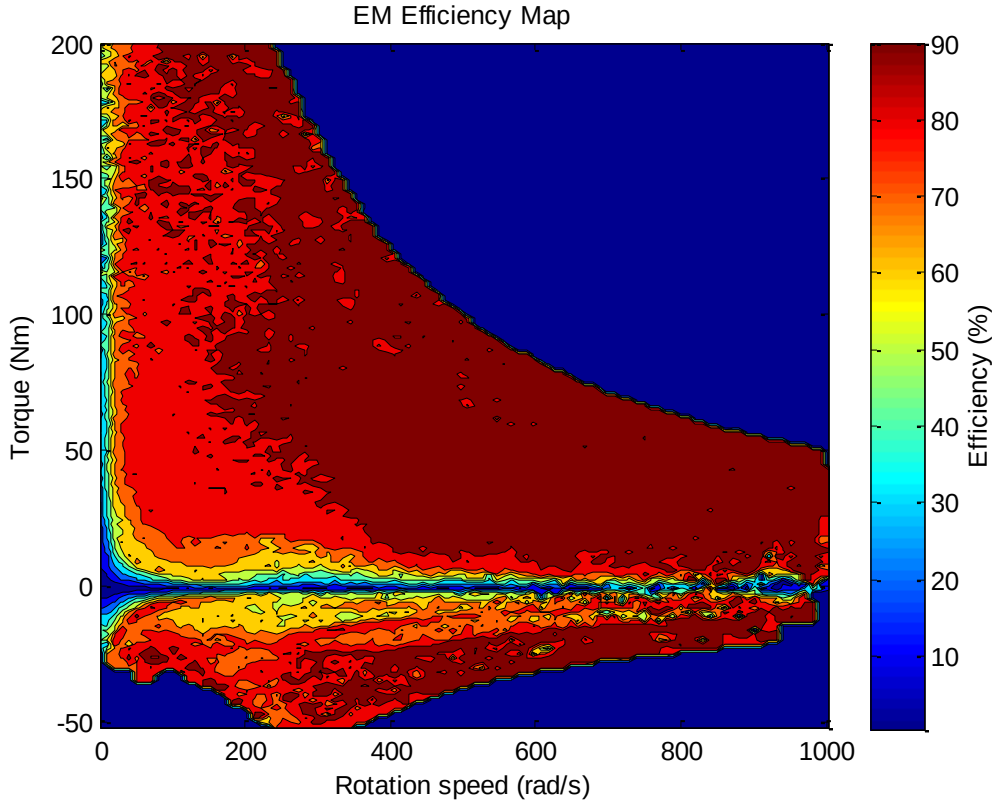


**Figure 20: Efficiency map from Simulink EM model**

When scaling the torque and efficiency characteristics of the EM, the ratio of the regenerative braking power (30% of the maximum propulsion power) is maintained. It is acknowledged that the regenerative braking strategy would affect the amount of recovered energy; however, sufficient knowledge of the braking system within the Smart ED, such as front to rear braking ratio or percentage of regenerative braking for a given demand was not known. It ought to be mentioned that the Smart ED is also a rear-wheel drive vehicle, and therefore the EM is at a disadvantage for recuperating energy under braking due to the longitudinal weight transfer. Therefore, a sensitivity study with regards to the regenerative braking percentage will be carried out to identify its impact on component size optimisation.

The mass of the Zytek system is given for different power ratings [91], as shown in Table 9. A linear trend line for mass was then formed by connecting these different power ratings, to estimate the EM mass, as shown in Figure 21. The mass values for two other manufacturer, YASA and EVO are also provided [97; 98] for comparison purposes. It is noteworthy that the increment of the EM mass as a function of its power is relatively small compared to the overall mass of a typical EV. This is shown in Figure 62 and is discussed further in Chapter 6 under Section 6.2.

**Table 9: EM data sourced from Zytek**

| Model Name | Power Rating (kW) | EM Type | Inverter Type | Combined Mass (kg) |
|---|---|---|---|---|
| Zytek 25kW | 25 | 3-phase PM | IGBT 3-phase bridge | 20.4 |
| IDT-120-55 | 55 | 3-phase PM | IGBT 3-phase bridge | 62 |
| IDT-300-70 | 70 | 3-phase PM | IGBT 3-phase bridge | 105 |

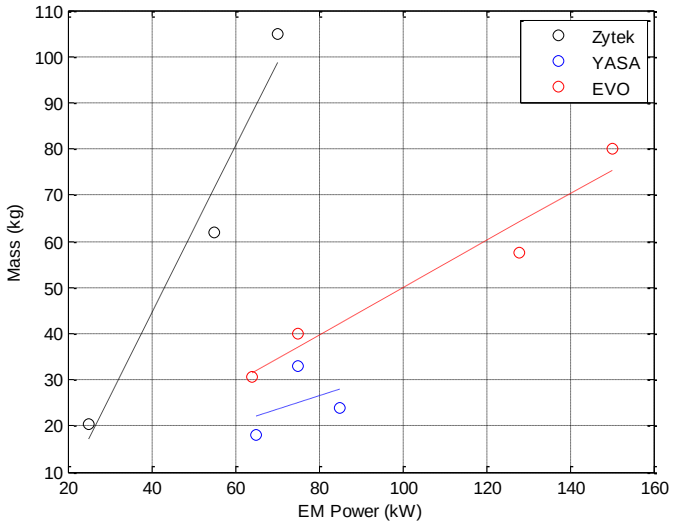


**Figure 21: Trend line used to estimate EM mass**

### 3.1.2.4 EM Verification

To verify the EM model, a backward-facing model of the Smart ED was created to simulate a driving cycle recorded from the actual car. The data for the Smart ED is listed in Table 6 and Table A2 (Appendix C). The torque measurements from the EM during that cycle was extracted from the CAN bus, and this was compared to the torque input to the EM on the backward-facing model. This comparison is shown in Figure 22. After calculating the cumulative error between the simulated and measured EM torque, it was determined that the accuracy of the simulated torque was 78%. This discrepancy was attributed primarily to the following:

- assumed drivetrain efficiency
- road inclinations
- effects of cross-winds

Road inclinations during the test drive were not included in the model because of inaccuracies in the on-board GPS measurements with regards to changes in elevation. Although the test was carried out on a calm day, any effects of cross-wind were also not captured in the simulated model, which could add to the error between the simulated model and measured data. The purpose of Figure 16 is to determine the accuracy of the vehicle model (which combines the resistance forces, inertial forces, and gear ratios) prior to calculating the output power of the EM. The accuracy of the output power of the EM is also a test for the accuracy of the combined EM and inverter efficiency map.

Based on the simulated torque input into the EM model, a comparison of the power output between the measured data and the simulated data was compared for each time step, and the scatter of these various operating points are shown in Figure 23.

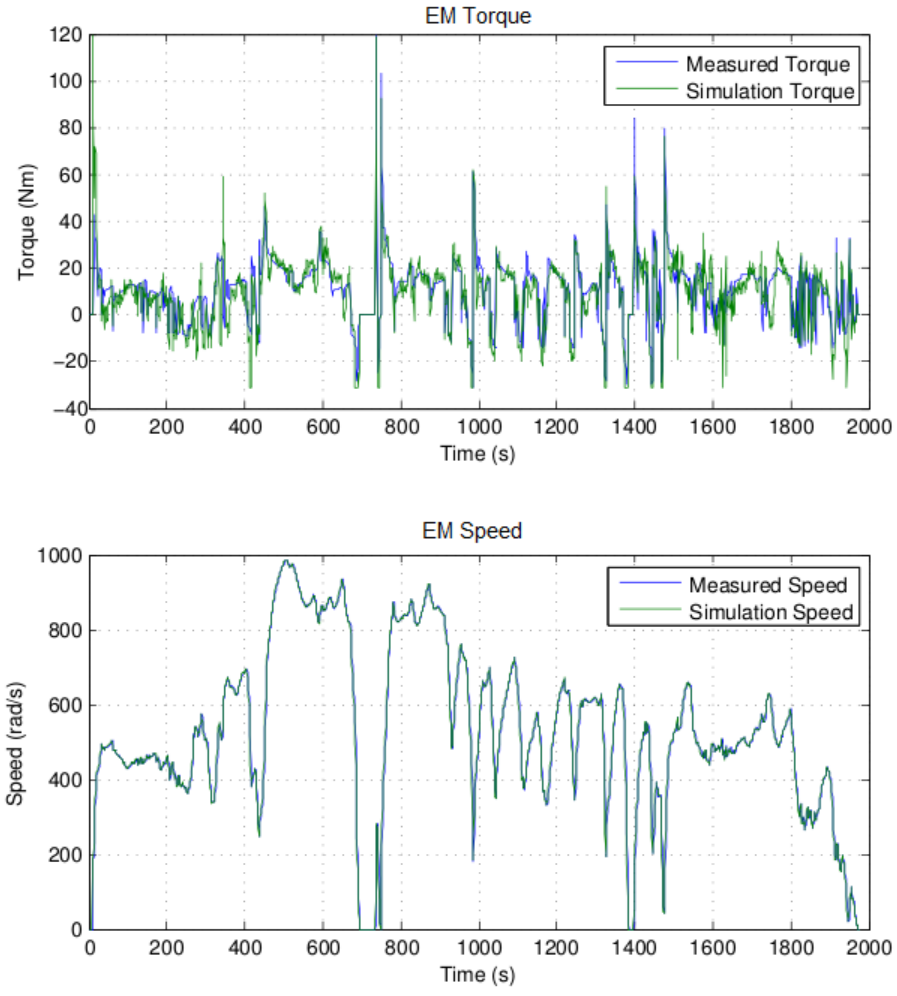


**Figure 22: Comparison of measured and simulated torque at the EM**

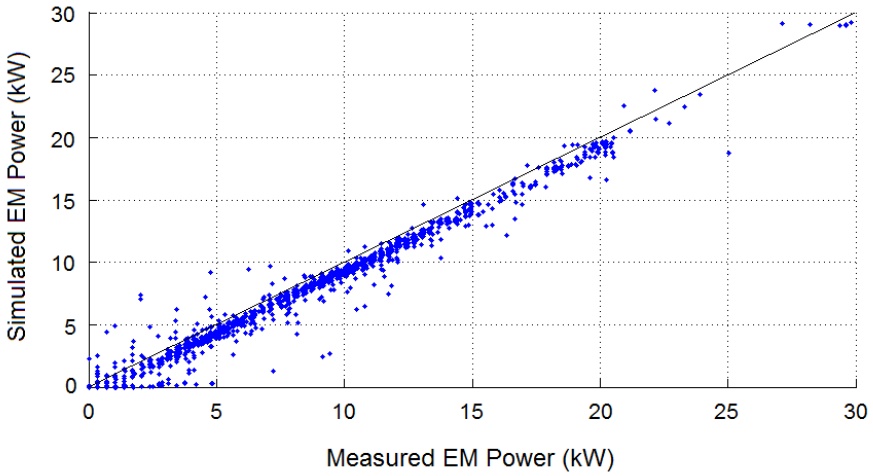


**Figure 23: Comparison of measured and simulated EM power**

### 3.1.3 Auxiliary Power Unit

The APU (also called "Range Extender" [99]) is used in the series hybrid architecture, and it is formed by connecting an ICE to an EM [39]. The series hybrid architecture was covered in Section 2.2.2. A practical example of an APU is the Lotus Range Extender [100], which was investigated as part of the LCVTP project. This APU forms the basis of numerical analysis in LCVTP. It combines a 1.3L 3-cylinder petrol ICE with a permanent magnet EM. This APU has a power output between 15KW – 35KW.

The Brake Specific Fuel Consumption (BSFC) is a measure of fuel efficiency for an internal combustion ICE [101]. It is the rate of fuel consumed for a given power output. As a power-specific measure, BSFC could be used to calculate emissions of an ICE according to the amount of power required to propel the vehicle based on the drivecycle. As the ICE within the APU is decoupled from the wheels of the vehicle, it can potentially be operated continuously along its best BSFC region.

To create the best BFSC line, a discrete set of BSFC points were first identified over a spectrum of ICE power outputs. The specific ICE speed and the torque point (with the highest efficiency) that produced each level power output were then identified. Next, an EM is paired to the ICE with a power rating that is able to work across the entire BSFC line. Figure 25 shows the BSFC line for a 1 litre ICE. The overall efficiency of the APU is the combined efficiency of the ICE and the EM, as shown in Equation (3-18).

$$\eta_{bsfc}(\omega_{apu}, T_{apu}) = \eta_{eng}(\omega_e, T_e) \cdot \eta_{em}(\omega_e, T_e) \quad \textbf{(3-18)}$$


**Figure 24: The Lotus Range Extender (left) for the Jaguar Limo Green (right)** [100]

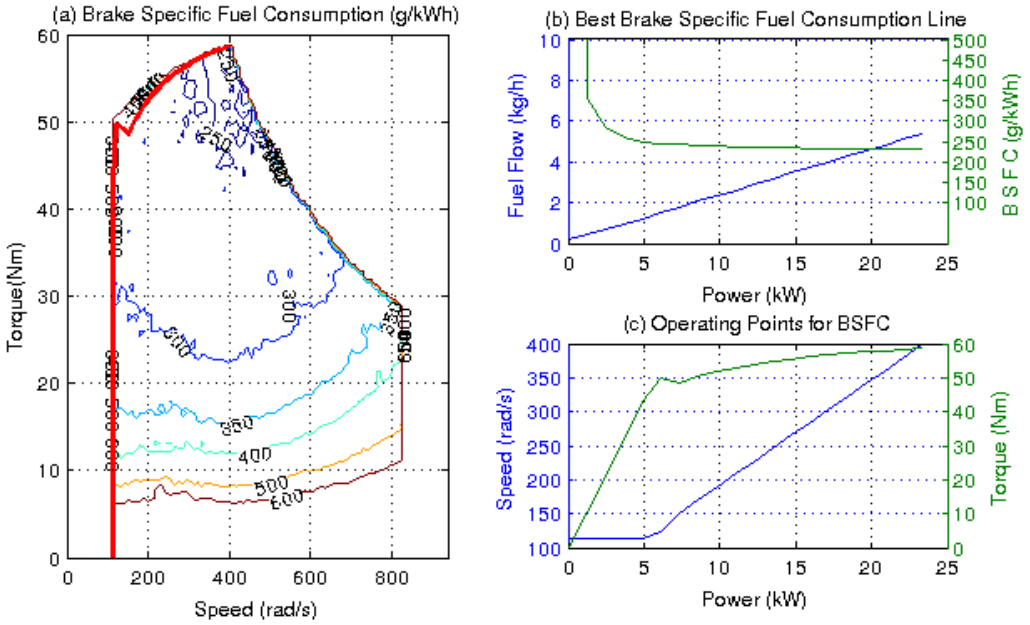


**Figure 25: Operating line for BSFC**

## 3.2 Energy Storages

Energy storage devices are defined as a system that stores energy in one form, for example as a combustible liquid, electric charge, or potential energy [62]. This stored energy is then converted into kinetic energy by one or more energy converters to propel the vehicle.

### 3.2.1 Batteries

Batteries are currently the most common form of mobile energy storage for low carbon vehicles. Lead acid, along with Nickel and Lithium-based chemistries, are the most common. Early electric vehicles, such as the GM EV1, utilised lead acid batteries, but this chemistry was considered too heavy [102]. Nickel Metal Hydride (NiMH) has been used for production in vehicles such as the Toyota Prius and the Honda Insight [103; 104].

However, it is acknowledged that Lithium-based batteries provide the best power and energy density to weight (compared to the other chemistries), with cell costs declining in recent years [12]. Other battery technologies, such as Nickel-Chloride, Lithium-Air, and REDOX were considered in several publications, but were mostly deemed unfeasible for automotive applications [12; 103; 105]. Therefore, the battery model will be narrowed down to Lithium-based batteries, and this research will be based on this chemistry.

For modelling purposes, the internal resistance of the battery can be approximated as a resistor in series with an Equivalent Electrical Circuit (EEC) model [106]. The advantage of the EEC battery model is that it provides good balance between accuracy, complexity, and runtime performance for automotive simulation applications [107]. The battery model was created based on the work by Tremblay *et al.* [108]. The schematic representation of a single Li-ion cell within the battery model is shown in Equation (3-19) and consists of the open circuit voltage, $U_{OCV(cell)}$, connected in series with a single resistor, $R_0$. To calculate the cell terminal voltage, $U_{L(cell)}$, the following equation is used

$$U_{L(cell)} = U_{OCV(cell)} - I_L R_0 \quad \textbf{(3-19)}$$

where $I_L$ is the current flowing through the battery. This relatively simple layout, also known as the "Rint" battery model [109], was adopted because the higher transient characteristics of the battery (< 1 Hz) was not captured, given the comparatively large sampling rate when measuring the battery data from the Smart ED. This negates the necessity to include capacitive elements (such as those found in the Thevenin and PNGV battery models [109]), and hence reduces the overall simulation time. Figure 26 shows the schematic diagram of the Rint battery model.

Data for parameterisation of the battery model was also obtained from the CAN interface of the Smart ED. The Open Circuit Voltage (OCV) was estimated based on the battery terminal voltage, temperature, and State-of-Charge (SOC). Figure 27 shows the relationship between the OCV, SOC, and temperature.

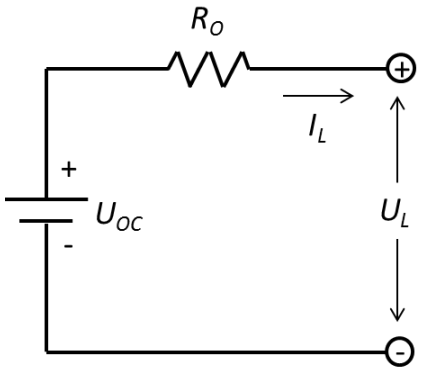


**Figure 26: The "Rint" battery model**

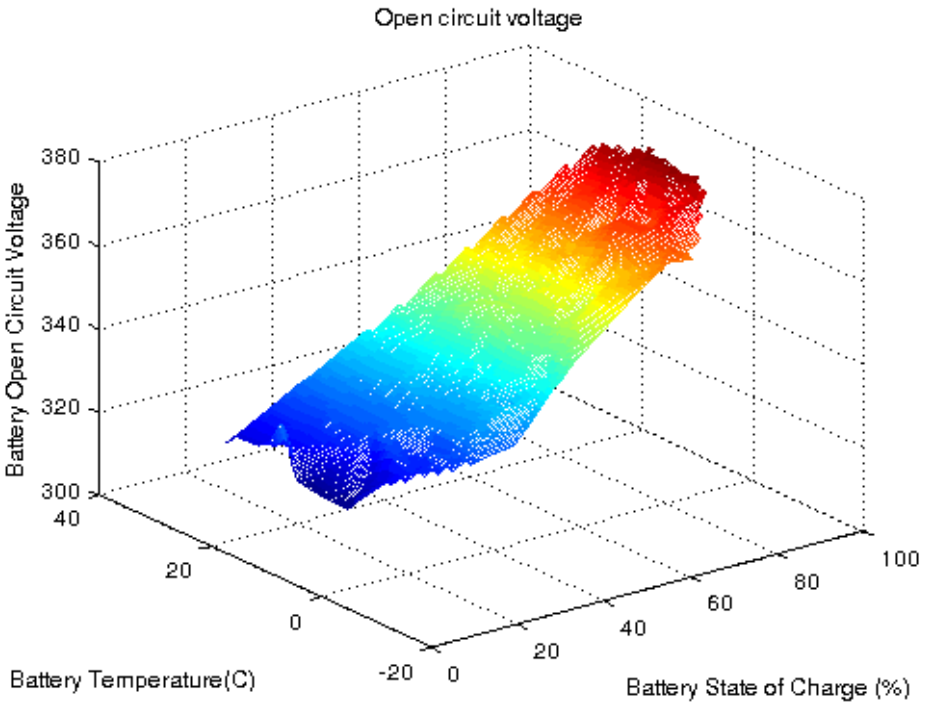


**Figure 27: The battery OCV map derived from the Smart ED**

### 3.2.1.1 Battery Model Scaling

The battery pack in the Smart ED is rated at 16.5 kWh and contains Panasonic NCR18650 cells [94]. According to the datasheet supplied by Panasonic, each cell has a capacity of 2.9Ah and mass of approximately 45g [110]. Each parallel string of cells has a capacity of approximately 1kWh. Therefore, a battery pack rated at 20kWh, for example, contains approximately 20 strings in parallel. It is estimated that each string contains 94 cells in series, after dividing the measured battery pack voltage from the Smart ED with the published cell voltage from Panasonic.

During simulation runtime, the SOC is quantified using the generic method of coulomb counting, in which $SOC_{init}$ defines the initial condition of the battery SOC and $Q_b$ the capacity of the battery expressed in Ah:

$$SOC(t) = \frac{SOC_{init} \cdot Q_b \cdot 3600 - \int_0^t I_b \cdot dt}{Q_b \cdot 3600} \quad \textbf{(3-20)}$$

where $I_b$ is the current flowing through the battery pack.

Figure 28 shows an example of the arrangement of cells in series and in parallel within a battery pack. In this example, there are two cells in series and three strings of cells in parallel. Referring to this example, and continuing on from Equation (3-19), the sum of the electrical currents in each string is shown in Equation (3-21), where $I_1$, $I_2$, and $I_3$ are the electrical currents passing through each string respectively.

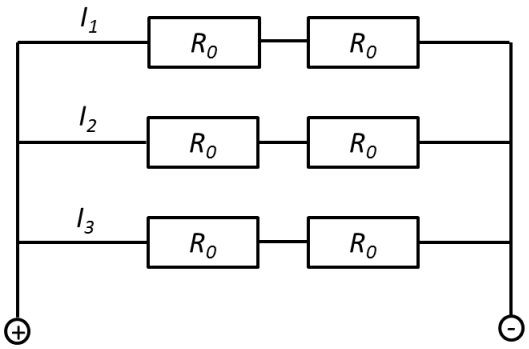


**Figure 28: Example of cell arrangements in a battery pack**

$$I_L = I_1 + I_2 + I_3 \quad \textbf{(3-21)}$$

The electrical current passing through each string of cells (two per string in this example) can then be calculated as shown in (3-22), where $U_{string}$ is the potential difference for each string of cells.

$$I_{1,2,3} = \frac{U_{string}}{2R_0} \quad \textbf{(3-22)}$$

Expanding further to three strings in parallel, the following equation applies:

$$I_L = 3\left(\frac{U_{string}}{2R_0}\right) \quad \textbf{(3-23)}$$

Given that $R_b$, the total internal resistance of the battery, is based on the following,

$$R_b = \frac{U_{string}}{I_L} \quad \textbf{(3-24)}$$

the following then applies by combining Equations (3-23) and (3-24),

$$R_b = R_0 \frac{2 \cdot U_{string}}{3 \cdot U_{string}} \quad \textbf{(3-25)}$$

Replacing "2" and "3" with $n_s$ (number of cells in series) and $n_p$ (number of strings in parallel) respectively the following generalised equation is obtained:

$$R_b = R_0 \cdot \frac{n_s}{n_p} \quad \textbf{(3-26)}$$

Equations (3-26) to (3-28) present how the battery is scaled by altering the number of parallel strings, $n_p$. This set of equations is executed to create the OCV map. The number of cells in series, $n_s$, is fixed during simulation to maintain the bus voltage. In these equations, $R_b$ is the battery internal resistance, $U_{OCV(batt)}$ is the battery OCV, and $Q_{cell}$ is the capacity of each cell.

$$U_{OCV(batt)} = U_{OCV(cell)} \cdot n_s \quad \textbf{(3-27)}$$

$$Q_b = Q_{cell} \cdot n_p \quad \textbf{(3-28)}$$

The value of $R_b$ will be discussed in Section 3.2.1.2. The cells within the battery pack are assumed to be homogeneous in operation, which allowed for scaling the battery pack size by changing the number of parallel strings. In reality, temperature gradient and disproportionate aging may affect the performance of individual cells [111].

### 3.2.1.2 Battery Model Verification

The value of the battery pack internal resistance, $R_b$, was estimated so that it performed as close as possible to the recorded SOC trajectory from the vehicle, during a charge-depleting cycle. This is similar to the approach shown by Rodrigues *et al.*, for measuring impedance of a Li-ion battery [112]. Using an optimisation routine, the value of $R_b$ was identified, such that the SOC trajectory of the battery model and the measured data was as close as possible. A comparison of the measured SOC and the estimated SOC (from the battery model) is shown in Figure 29.

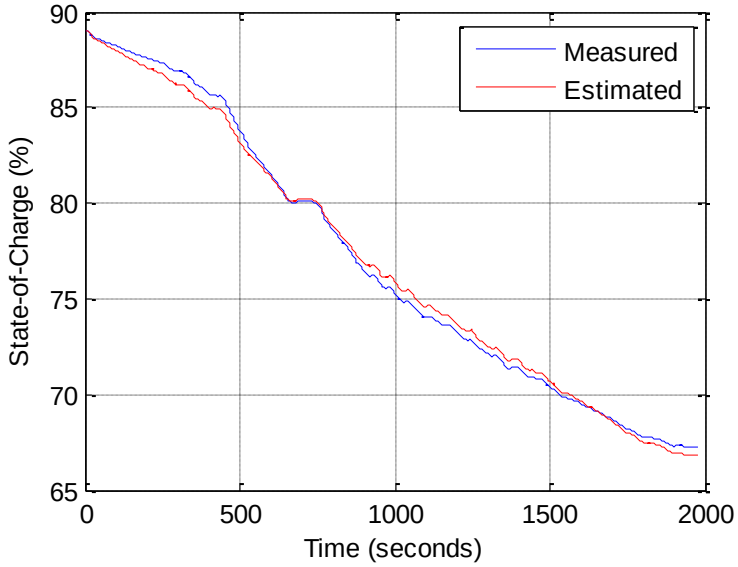


**Figure 29: Comparison of measured and estimated battery SOC**

Based on this optimisation routine, the value for $R_b$ was identified to be 0.43 ohms. The author acknowledges that variations in the resistance under charge and discharge conditions, as well as in different thermal operating conditions, were inherently averaged using this approach. Furthermore, any additional resistances from the battery contactors have also been lumped using this approach. However, without a controlled test environment on a battery test rig, it was difficult to extract the specific resistance values. Future work could investigate on improving this area.

### 3.2.2 Fuels

Fuels represent liquid or compressed gaseous fuels stored in sealed tanks, and to be later used as part of a combustion or chemical reaction process to produce energy that propels the vehicle.

At present, fossil fuels are the dominant energy source for ground transportation, primarily as petrol and diesel [113; 114]. Alternative fuels, such as hydrogen, are also available. However, the ability of hydrogen production and utilisation to remain sustainable in the long term is being debated [115; 116].

The tank's volume and mass is parameterised to compute sizing. The fuel tank connects to the ICE or the APU and calculates the amount of fuel consumed. Table 10 shows the terms used for calculating the amount of fuel used when the tank is connected to the ICE or the APU.

**Table 10: Terms used for fuel tank calculations**

| Term | Definition | Units |
|---|---|---|
| $m_{fuel}$ | Fuel mass | kg |
| $\dot{m}_{fuel}$ | Fuel mass flow rate | kg/s |
| $TtW\_CO_2$ | Tank-to-Wheel $CO_2$ | kg |
| $WtW\_CO_2$ | Well-to-wheel $CO_2$ | kg |
| $WtT\_CO_2$ | Well-to-tank $CO_2$ | kg/J |
| $H_l$ | Fuel calorific heating value | J/kg |

To calculate the total amount fuel used, the mass flow rate of the fuel consumed by the ICE or the APU is integrated over the length of the simulation time:

$$m_{fuel} = \int_0^{t_{end}} \dot{m}_{fuel}\, dt \tag{3-29}$$

The tank-to-wheel $CO_2$ emission is then calculated, where $mass\_ratio_{CO_2}$ is the mass of $CO_2$ emitted per unit mass of petrol that undergoes combustion at the stoichiometric ratio (3.17 kg$CO_2$/kg petrol) [117; 118]:

$$TtW\_CO_2 = mass\_ratio_{CO_2} \times m_{fuel} \tag{3-30}$$

Finally, the well-to-wheel $CO_2$ emission is calculated based on the well-to-tank conversion factor of 14.10 kg$CO_2$/MJ of petrol used [55]:

$$WtW\_CO_2 = m_{fuel}(H_l \times WtT\_CO_2) + TtW\_CO_2 \tag{3-31}$$

### 3.2.3 Flywheel

A flywheel is a mechanical storage medium, with energy and power density figures comparable to ultracapacitors [119]. The flywheel model is based on the mechanical flywheel system by Flybrid Automotive Limited [120]. In this system, the flywheel is connected to the final drive via a CVT and a clutch. This arrangement classifies the vehicle as a parallel hybrid. The flywheel system is only used to provide power assist during vehicle acceleration and to recover energy during vehicle braking.

The rotary inertia of the flywheel is used to store energy. The higher the rotational velocity, the more energy is stored. This energy, $E_f$, is defined by,

$$E_f = \frac{1}{2} J_f \omega_f^2 \tag{3-32}$$

where $J_f$ is the rotary inertia and $\omega_f$ the rotational speed. In order to maximise the energy stored, it is more efficient to raise $\omega_f$ (because it is squared) than to increase $J_f$. For this reason, many flywheel systems utilise Carbon Fibre Reinforced Plastic (CFRP) to limit mass and rotational inertia, but increase rotational speed up to 64000 rpm [4]. CFRP also has the advantage of being a low density material with high stiffness, and therefore has minimal expansion at high rotational speeds (around 1 mm at 64000 rpm in the example given by Cross and Hilton [4]).

Figure 30 shows the flywheel system investigated in this research, which is manufactured by Flybrid. They produce a range of flywheel systems with energy storage capacities from 150 kJ to 600 kJ [4].

To size the flywheel, the maximum required energy, $E_{f(max)}$, has to be decided first. The maximum energy of the flywheel is obtained when $\omega_f = \omega_{f(max)}$, where $\omega_{f(max)}$ is the maximum flywheel speed limit at 64,000 rpm.

The flywheel can then be sized by determining the required inertia given by,

$$J_f = \frac{1}{2} m_f (r_i^2 + r_o^2) \tag{3-33}$$

where $m_f$ is the mass of the flywheel, and $r_o$ and $r_i$ are the outer and inner radii of the flywheel respectively. The energy capacity of the flywheel is defined by scaling the outer radius.

The flywheel system's losses are contributed by the friction torque from bearing ($T_{loss}$) and the efficiency of the CVT ($\eta_{CVT}$). For each time increment of the simulation, the energy dissipated due to these losses, $E_{loss}$, can be calculated as,

$$E_{loss} = \left[T_{loss}\omega_f + P_f(1 - \eta_{CVT})\right] \cdot t_s \tag{3-34}$$

where $t_s$ is the time increment of the simulation and $P_f$ is the power demand to the flywheel system. The value of $T_{loss}$ is based on a lookup table, which was made available to the authors by Flybrid, whilst the efficiency of the CVT is fixed at 85% [121]. The net energy content of the flywheel system is then provided by the equation,

$$E_k^t = E_k^{t-1} - E_{loss} \tag{3-35}$$

Where $E_k^t$ is the flywheel energy at time *t*. The flywheel model was validated using data provided by Flybrid.

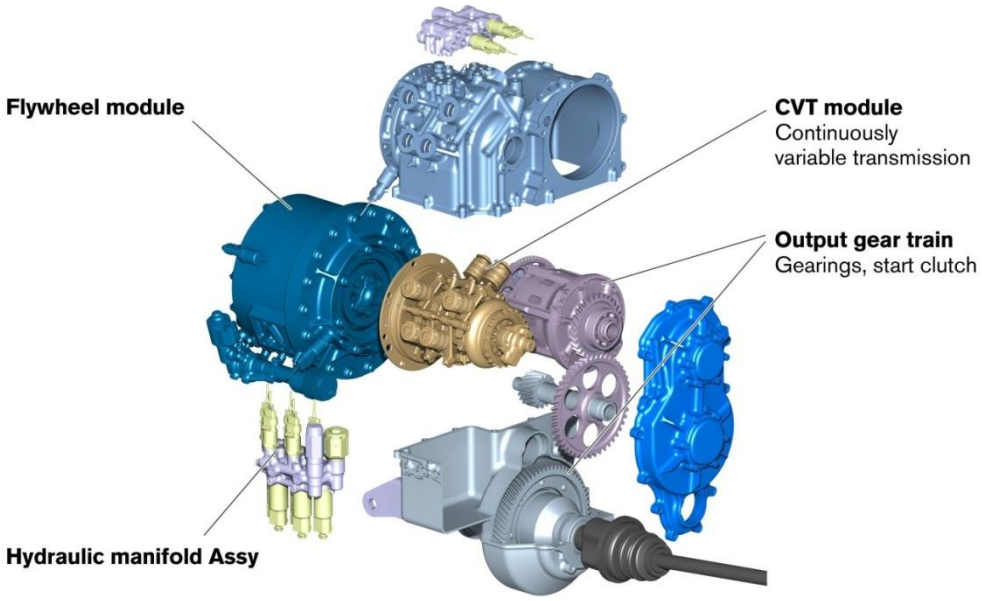


**Figure 30: Flywheel energy storage from Flybrid** [122]

## 3.3 Power Transformers

Power transformers are defined as devices that convert the ratio of the efforts and flows within a power domain. For example, a mechanical transmission will multiply the input torque and divide the input speed by a given ratio (or vice-versa). Ignoring losses, the power in will be equal to the power out of a mechanical transmission.

### 3.3.1 Mechanical Transmission

For the purposes of this research, a simple discrete controllable transmission was utilised [123]. The final drive offers a further gear reduction, and will be lumped into the overall ratio. The implementation of the mechanical transmission models in Simulink are shown in Appendix D.

In this research, the 8-speed transmission from the Jaguar XJ saloon is utilised when the ICE is the prime mover. This transmission was chosen because of the familiarity with the vehicle as a result of the work carried out for the LCVTP project. Due to the lack of experimental data, a nominal efficiency value of 0.9 was assumed for the transmission, using the work by Irimescu *et al*. [124] as a guideline. In contrast, when the EM is the primary mover, the single-speed transmission ratio from the Smart ED is utilised. The data for all gear ratios are shown in Appendix C.2.

The equation for the mechanical transmission is given by Equations (3-36) and (3-37),

$$T_{gb} = \frac{T_w}{\eta_{gb} \cdot \varphi_{gb}} \quad \textbf{(3-36)}$$

$$\omega_{gb} = \omega_w \cdot \varphi_{gb} \tag{3-37}$$

where $\eta_{gb}$ is the transmission efficiency, $\varphi_{gb}$ is the gear ratio, $T_{gb}$ and $T_w$ are the input and output torque of the transmission shafts, and $\omega_{gb}$ and $\omega_w$ are the input and output speeds of the transmission shafts. The output torque of the transmission shaft is also the torque at the wheels, as will be discussed in Section 3.4. Likewise, the output speed of the transmission shaft is the same as the wheel speed.

For the NEDC, the gear shift schedule is based on the procedures laid out by the Economic Commission for Europe [84]. The shift points are shown in Figure 31.

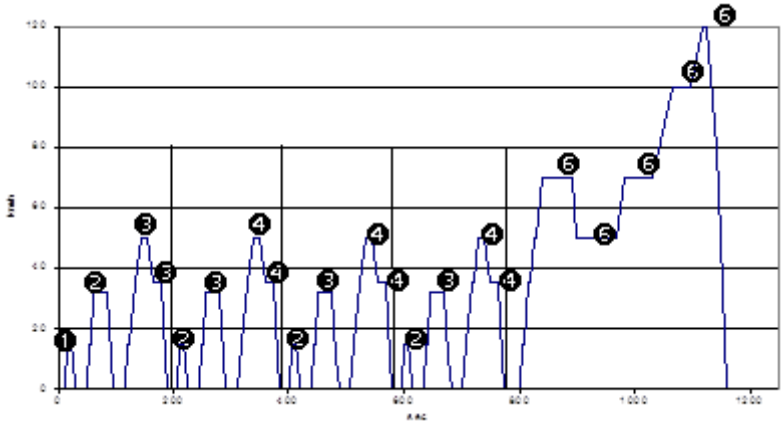

**Figure 31: Gear shift points on the NEDC** [84]

For other drivecycles, the shift schedules for the transmission are controlled by a rule-based strategy such that the engine speed is maintained between 200 and 400 rad/s for a given vehicle speed. This range was chosen because it contains a region of higher BSFC points based on the Willans ICE model and also based on the suggestions by [125]. In the forward-facing model, an further rule is added such that the transmission shifts into a lower gear if the torque demand is more than 90% of the maximum ICE torque ($T_{e(max)}$) and if the ICE speed limits are not exceeded. This is akin to the kick-down switch in an automatic transmission.

The author would like to make an assertion that the transmission shift strategies proposed here, though simple, are sufficient for the purpose of this research. Further research on optimal shift strategies, as proposed by Viet [126], could be implemented as part of future work.

### 3.3.2 Power Electronics

Power electronics mainly comprise of buck-boost converters that step voltage up or down, and inverters that convert DC electrical power to AC electrical power [127]. Similar to mechanical transmissions, the magnitude of power flowing in and out of the system is constant (ignoring losses).

Electrical interfaces with energy storages will be at power levels to simplify calculations within the proposed simulation tool. Therefore, the power electronics will not be explicitly modelled for the purpose of this research; instead, the efficiency of such converters will be lumped with the efficiency maps of the respective energy converters and storages.

## 3.4 Vehicle Model

The vehicle model is described by the following information:

- Glider mass (mass of the vehicle without powertrain components)
- Aerodynamic properties
- Tyre rolling resistance characteristics.

The opposing forces to the motive effort provided by the powertrain are calculated based on the sum of the aerodynamic drag, rolling resistance, inertial forces, and road inclination. These are shown in Equations (3-38) to (3-41) respectively, where $C_D$ is the drag coefficient, $A_f$ is the frontal area of the vehicle, $v$ is the velocity of the vehicle, $\mu_{RR}$ is the rolling resistance coefficient of the tyre, $m_v$ is the mass of the vehicle, $g$ is the acceleration due to gravity, $\rho$ is the density of air, $a$ is the acceleration of the vehicle, and $\theta$ is the angle of road inclination.

$$F_D = \frac{1}{2}\rho C_D A_f v^2 \quad \textbf{(3-38)}$$

$$F_{RR} = \mu_{RR} m_v g \quad \textbf{(3-39)}$$

$$F_A = m_v a \quad \textbf{(3-40)}$$

$$F_{inc} = m_v g \cos\theta \quad \textbf{(3-41)}$$

Therefore, the total force at the contact patches of the tyres, $F_T$, is,

$$F_T = F_D + F_{RR} + F_A + F_{inc} \quad \textbf{(3-42)}$$

And the torque at the wheels, $T_w$, is then given as,

$$T_w = F_T \cdot r_w \quad \textbf{(3-43)}$$

where $r_w$ is the rolling radius of the tyre. Detailed information of the relevant vehicle parameters is included in Appendix C. A small test case was carried out in Section 6.4.4 to investigate the influence of road inclination on the optimisation results.

## 3.5 Estimating Financial Costs of Components

Including monetary costs into this research was challenging due to the diversity of factors involved. From a powertrain component standpoint, this encompassed the following [69; 78]:

- manufacturing costs
- operating costs
- residual values at the end of the vehicle's life.

Based on the quality of data from literature and to maintain focus on the aims of this research, a decision was made to simplify the costs of the components based on the financial costs at the point of sale to the consumer. To that end, research published by the NREL [128-130] was utilised to quantify system costs of the battery, EM, and ICE, whereas data from Flybrid was used to quantify the system cost of the flywheel. A full derivation of the financial weightings was discussed by the NREL [128]; therefore, it will not be repeated here. However, it is noteworthy that factors such as market segmentation, vehicle class, and the expected profitability were included within their analysis. Validations of the empirical relationships were provided, where the authors verified the financial cost equations for EVs and HEVs that are currently on the market. This validation has been reproduced in Figure 32.

Equation (3-44) defines the installed cost of the battery pack as a function of peak power, $P_{b(max)}$, and capacity, $Q_{b(max)}$. Equations (3-45) and (3-46) define the financial cost of both the EM and the ICE as a function of their respective peak power requirements, $P_{em(max)}$ and $P_{e(max)}$. Equation (3-47) is used for the flywheel, where $E_{f(max)}$ is the maximum energy capability of the flywheel.

$$Battery\ Cost = \frac{\$22.00}{kW} \cdot P_{b(\max)} + \frac{\$700.00}{kWh} \cdot Q_{b(max)} + \$680.00 \quad \textbf{(3-44)}$$

$$EM\ Cost = \frac{\$21.70}{kW} \cdot P_{em(max)} + \$480.00 \quad \textbf{(3-45)}$$

$$ICE\ Cost = \frac{\$14.50}{kW} \cdot P_{e(max)} + \$531.00 \quad \textbf{(3-46)}$$

$$Flywheel\ Cost = \frac{\$4.40}{kJ} \cdot E_{f(max)} + \$1833.00 \quad \textbf{(3-47)}$$

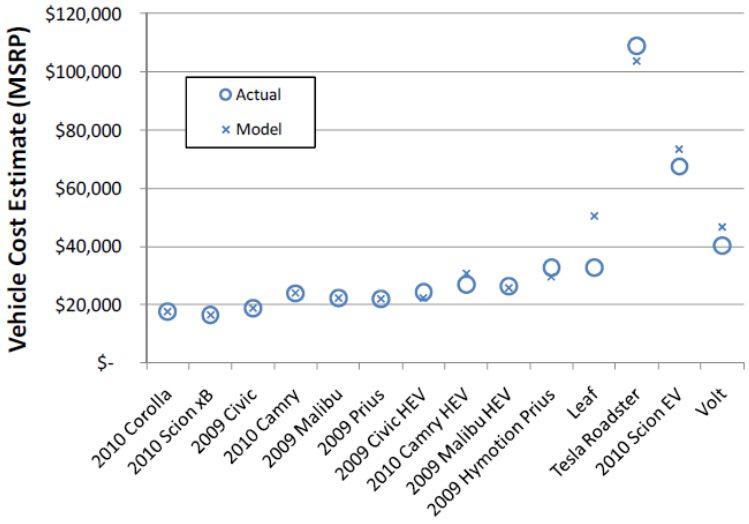


**Figure 32: Validation of the estimated costs** [128]

It ought to be mentioned that at the point of developing the models for running the simulations, validation was carried out using data published by the NREL in 2010 [128]. Component prices, particularly newer battery chemistries, will have variations in their costs. Additionally, based on equations (3-44) to (3-47), the battery plays a significant role in the overall costing of the vehicle powertrain (estimated to be $12,320 for the Smart ED based on equation (3-44)). In 2013, the state of Lithium-ion battery cost has been reported to be $500 per kWh [131].

## 3.6 Modelling Assumptions and Limitations

The models of the powertrain components described in Sections 3.1 and 3.2 were developed to be scalable for inclusion into the optimisation framework contained within the proposed toolbox. It ought to be mentioned that the models will not be able to capture certain variations in efficiency of the system, particularly with regards to external factors such as changes in operating temperature. Sensitivity analyses will be carried out where necessary to ascertain the severity of the model assumptions towards the optimisation results.

Data for the scalable model of the ICE was obtained from previously published research [62]. While the data in [62] have been experimentally validated, it is acknowledged that ICE technology in general has continued to advance [132]. Hence, if more complex models were included within the proposed toolbox, it is envisaged that the ICEs would operate at higher efficiencies, thus leading to further downsizing.

The methods for scaling the powertrain components were demonstrated within literature [62; 69; 133], and these studies have provided experimental validation for those

methods. However, one assumption made with the models is the near-linear relationship between the powertrain component mass and its capacity (or peak power). In practice, the addition or removal of relevant ancillary devices may cause a compounding effect and result in further non-linearity in this relationship. Nevertheless, the aim of this research is to demonstrate the framework of simultaneous powertrain optimisation, in which powertrains are assessed at the system level. Focus is given to the transition from one powertrain to the other, as opposed to the absolute accuracy of the model. In this respect, the models have to be sufficiently valid to demonstrate this capability, and further research may wish to explore the integration of higher-fidelity models into the toolbox. As discussed previously, the use of uniform power-based interface between the models will allow practitioners to incorporate other types of powertrain components as needed.

Additionally, further considerations may need to be given for the physical size and volume of the powertrain components and the associated packaging constraints within the vehicle. The vehicle glider mass is assumed to remain constant although the powertrain component sizes will be varied during the optimisation routine.

For hybrid powertrains, it should also be noted that the output of the proposed tool is independent of level of hybridisation, (such as micro, mild and full hybrid). Additionally, EVs and PHEVs will require inclusion of an on-board charger which has not been explicitly modelled, but will be included in the overall $CO_2$ emission calculations for replenishing the battery to its initial SOC at the end of the drivecycle.

## 3.7 Drivecycles

Drivecycles are used to simulate the driving conditions that the vehicle will encounter. In this research, only the longitudinal speeds and acceleration will be evaluated. To that end, three types of drivecycles were used as examples of vehicle duty cycles; the NEDC [134], the combined ARTEMIS cycle [93; 135], and the “Cranfield cycle” [136].

Drivecycles can be classified into two categories based on their formulation; modal cycles and transient cycles [137]. A modal cycle is created using a repetitive series of vehicle operating conditions [138]. The NEDC, developed by the Economic Commission of Europe, is an example of a modal cycle. Based on Figure 33, it is observed that there are a number of repeating smaller cycles and constant speed sections. The NEDC represents the test cycles for Europe, and it is the first type of drivecycle considered for this research.

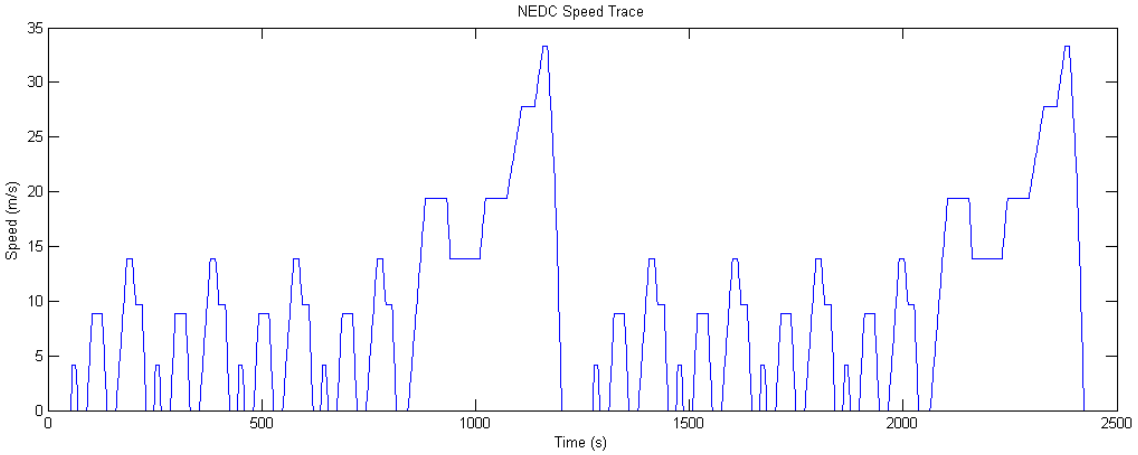


**Figure 33: The NEDC (repeated twice)**

Modal cycles are often adopted by legislative bodies because of the ease of performing standardised emission tests on vehicles using a dynamometer. However, modal cycles do not adequately describe the underlying distribution of speeds and acceleration which would be encountered in real-world driving scenarios. The NEDC, for example, was formulated when the average power output of the engine was relatively lower, therefore the acceleration rates on the NEDC is comparatively lower than the acceleration rates encountered in the real-world [52]. The acceleration levels encountered in real-world scenarios are higher, thus implying higher power and energy requirements. The work done by Lund University [139] suggests that real-world acceleration levels would lead to increased fuel consumption and emissions between 20 to 40 percent in a conventional vehicle.

Conversely, transient cycles contain actual simulation of typical road routes. Legislative bodies in the USA, Canada, Australia, and Switzerland use such cycles. Since the test cycle emulates real-world driving, it has more speed variations when compared to modal cycles. As transient cycles are more representative of real-world driving, tests performed with these drivecycles give a better representation of fuel consumption and emission figures [140]. In Europe, an example of a representative transient cycle is the ARTEMIS drivecycle. This cycle is represented in Figure 34. A background on formulation of these representative cycles can be found in the work by André [93]. The ARTEMIS is the second drivecycle considered for this research.

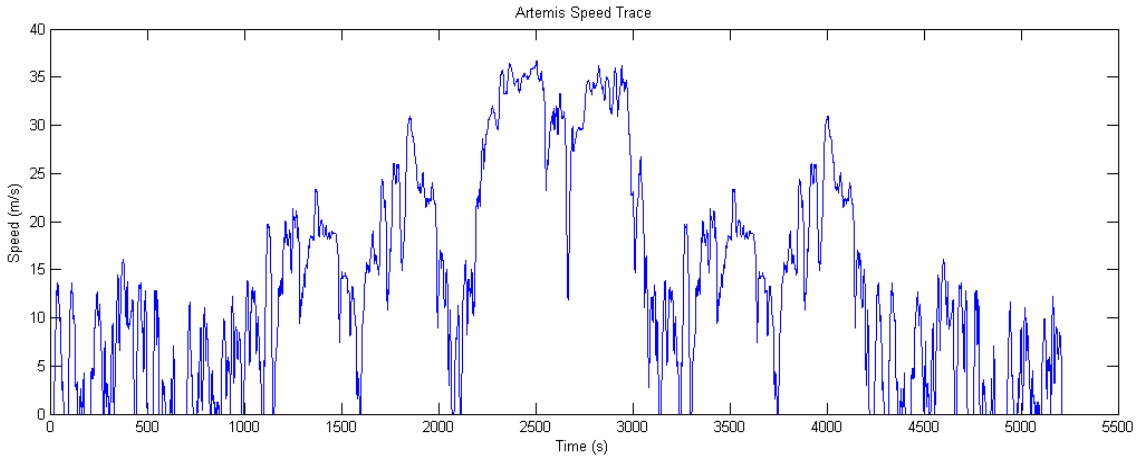


**Figure 34: The ARTEMIS cycle**

The third drivecycle considered for this research was derived from series of real-world usage studies undertaken by Cranfield University and recorded with the Smart ED, as discussed in Section 3.1.2.2. It combines speed traces from usage in urban, A-road, B-road and motorway sections. This cycle, called the "Cranfield cycle" is shown in Figure 35.

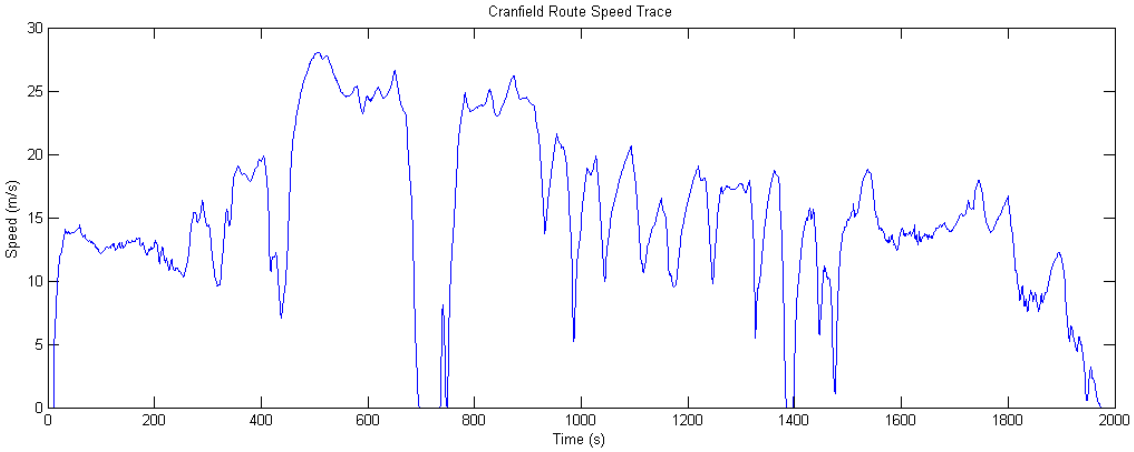


**Figure 35: The Cranfield cycle**

The detailed characteristics of these drivecycles will be discussed further in Chapter 5.

## 3.8 Sensitivity Analysis

Several assumptions were made during the creation of the powertrain component models. One such example is the regenerative braking strategy, which was derived from the rear-wheel driven Smart ED and limited to 30% of the maximum propulsion power, as seen in Figure 20. Therefore, a sensitivity analysis was carried out to identify the severity of variation in the vehicle parameters towards energy consumption for each of the drivecycle. The sensitivity equation is given by the following [62]:

$$S = \lim_{\Delta U \to 0} \frac{[E_{Traction}(B + \Delta B) - E_{Traction}(B)] / E_{Traction}(B)}{\Delta B / B} \quad \textbf{(3-48)}$$

where $B$ is a given vehicle parameter, $\Delta B$ is the change in that parameter for sensitivity analysis, and $E_{Traction}$ is the energy consumed to complete the drivecycle.

An EV powertrain was used as a case study for this sensitivity analysis. It uses the following parameters as nominal points, which are similar to a Nissan Leaf, a typical EV [141]:

- EM peak power: 80kW
- Battery size: 24kWh
- Glider Mass: 1000kg
- Drag coefficient: 0.3
- Cross sectional area: 2.3 $m^2$

The sensitivity analysis was based on the variation of the following parameters:

- Glider mass (potential variation caused by passenger and luggage)
- Aerodynamic drag (open window, sunroof, or retracted convertible roof)
- Regenerative braking % (change based on front-wheel drive, rear-wheel drive, or variation in brake blending configuration).

The first two points were included based on similar investigations by Guzzella and Sciarretta [62]. The last point was included due to the uncertainty in the assumptions for the regenerative strategy, as discussed in Section 3.1.2.1. The effects of the changes of these parameters are shown in Figure 36.

It is observed that at the nominal points (shown by the black circles), the ARTEMIS cycle demands the highest energy usage per 100km, followed by the Cranfield cycle and then the NEDC. This was expected, given the variations in acceleration levels between those drivecycles. The variations in acceleration are also made more evident with the sensitivity result of the regenerative braking strategy. The energy consumed in the ARTEMIS cycle almost constantly declines when more braking energy is recuperated. For the Cranfield cycle, there is a sharper decline up to the nominal point, and then it tapers off thereafter. This is because the regenerative braking percentage is oversized after the nominal point for the Cranfield cycle, and therefore energy recuperation hits a point of diminishing returns. For the NEDC, there was hardly a variation in the energy consumption with respect to changes in the regenerative braking strategy. Being a modal cycle, as described previously, the NEDC does not saturate the limits of the energy recuperation due to its lower deceleration levels. Detailed analysis of the cycles will be covered further in Section 5.1.

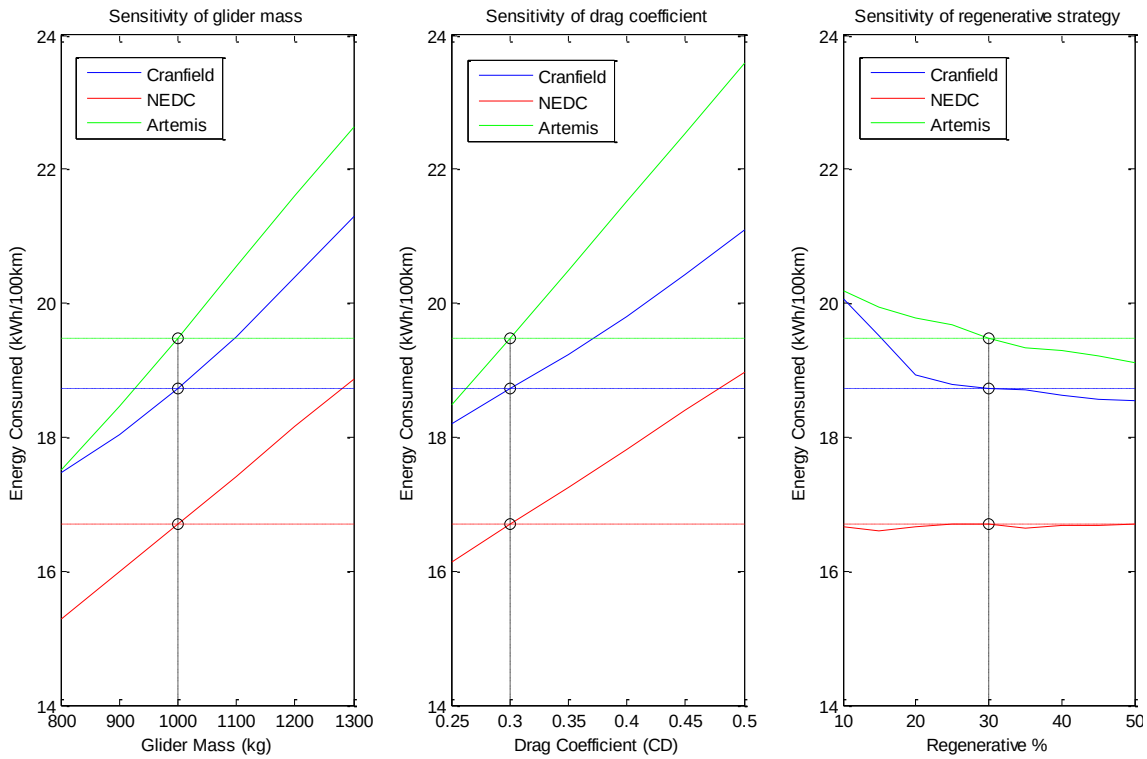


**Figure 36: Change in energy consumption as a function of parameter changes**

Figure 37 shows the normalised sensitivity based on Equation (3-48). Here, the relative sensitivities of the different parameters are more evident. The sensitivity for each parameter from each drivecycle is obtained by taking the derivative at the nominal points in Figure 36.

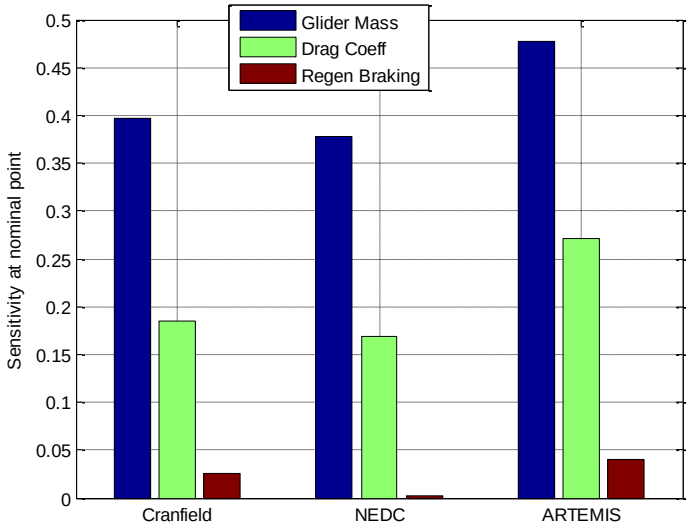


**Figure 37: Sensitivity at the nominal point for each drivecycle**

It can be deduced that changes in vehicle mass has the highest effect towards overall energy consumption, followed by drag coefficient and regenerative strategy. The ratio between the sensitivity of the glider mass and drag coefficient also parallels the trend seen in the same analysis carried out by Guzzella and Sciarretta [62]. The regenerative braking percentage is the least sensitive in comparison to the other parameters.

## 3.9 Chapter Conclusions

This chapter described the creation of powertrain components that will be used in subsequent chapters for simulating and optimising various powertrain topologies. To allow the proposed toolbox to switch between different types of powertrain architectures, the powertrain components had to be modularised. This entailed classifying the components into three main types: energy converters, energy storages, and power transformers. These components and their classifications are shown in Table 11.

**Table 11: Classification of powertrain components**

| | |
|---|---|
| Energy Converters | ICE |
| | EM |
| Energy Storages | Fuel Tank |
| | Battery Pack |
| | Flywheel |
| Power Transformers | Mechanical Transmission |
| | Power electronics |

This list of powertrain components was narrowed down based on the availability and quality of data gathered from literature and work carried out by Cranfield University for funded projects. Whilst the components were verified against data from real vehicles, several assumptions were made with regards to their scaling for peak power. Additionally, the scaling of financial costs and component mass was based on linear functions. Nevertheless, this level of fidelity was deemed sufficient for the purpose of this research. The modularity of the toolbox will allow for higher fidelity models to be included as part of future work.

The financial cost equations presented in this chapter represents the installed cost of the main powertrain components. While the underlying financial cost trends between the

respective components were discussed, it is noteworthy that the absolute values may vary amongst manufacturers and across different component technologies.

The duty cycles that will be used to simulate the various powertrain will consist of three drivecycles. They are the:

- NEDC
- ARTEMIS
- Cranfield cycle

Lastly, a sensitivity analysis was carried out to identify the severity of the uncertainties of several parameters in the model. Based on the EV powertrain that was analysed, it was found that changes in glider mass had the most pronounced effect towards changes in energy consumption. The trends from the sensitivity analysis were noted and will be taken into account during the optimisation study later in this thesis.

# 4 MODULAR POWERTRAIN STRUCTURE

The MPS was developed to facilitate the switching of powertrain topologies and scalable powertrain components during optimisation runtime. The MPS forms one half of the framework within the proposed toolbox; the other half is the optimisation algorithm. The high-level structure of this framework is shown in Figure 38. In this chapter, the novel methodology within the proposed toolbox, which is built upon the backward-facing method, is discussed. Sections 4.1 to 4.3 will address the first claim of novelty by discussing the workings of the MPS. Section 4.4 will partly address the second claim of novelty by discussing the implementation of multi-objective optimisation with the MPS.

## 4.1 Framework of the Proposed Toolbox

As discussed previously, all powertrain architectures have at least one type of energy storage and energy converter respectively [39]. Using the powertrain components that were discussed in Chapter 3, the energy storages and energy converters are organised within the MPS, and based on the arrangement shown in Figure 38. The optimiser, interfaced with the MPS, selects and sizes the powertrain components. The optimiser utilises a Genetic Algorithm (GA), which will be elaborated later. The MPS also holds information on the various configurations of the powertrain architectures and topologies. If the "MPS" block in Figure 38 (highlighted in red) were to be expanded further, it will relate back to the powertrain architectural hierarchy shown in Figure 2 on page 5.

### 4.1.1 Modular Powertrain Structure

The key feature of the MPS is the layout of the powertrain component placeholders, which can be seen in the high-level block diagram in Figure 39. This feature allows permutations of different energy converters and energy storages. This was made possible by having a clear distinction between the energy storage, energy converter, and power transformer. Using the CV and PHEV as examples, the full implementation of the MPS in Simulink can be found in Appendix D.

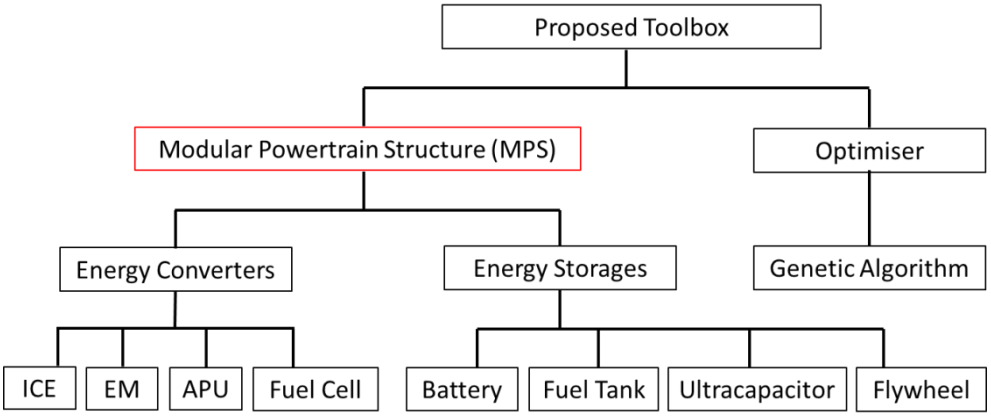


**Figure 38: The structure of the framework within the proposed toolbox**

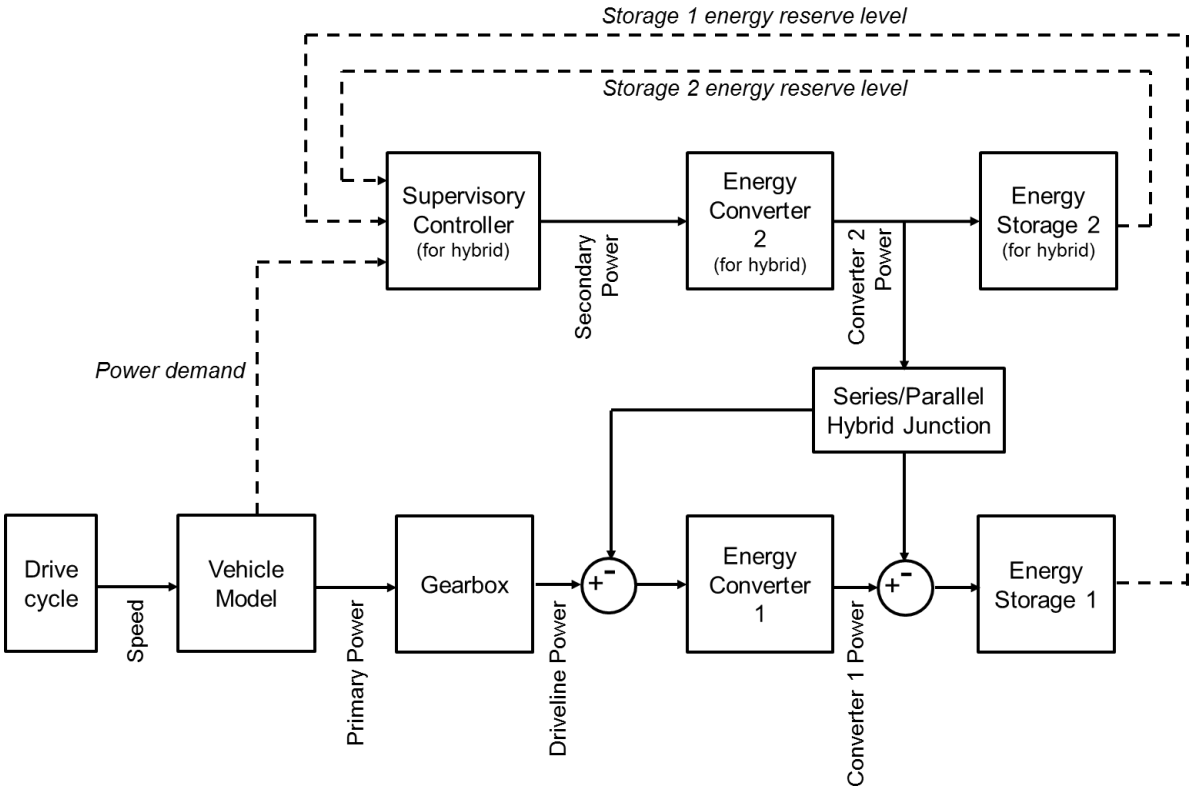


**Figure 39: High-level block diagram for layout of the powertrain component placeholders in the MPS**

To investigate the workings of the MPS, several powertrain topologies were created based on the available powertrain components that were discussed in Chapter 3. These topologies are shown in Table 12. As seen in the last row of this table, each powertrain

topology is assigned a "Powertrain Variant", which is an integer used by the optimiser to select the appropriate powertrain during the optimisation runtime.

**Table 12: Powertrain architectures to investigate the model framework**

| Architecture | Single Power Source | | Series Hybrid | Parallel Hybrid |
|---|---|---|---|---|
| Topology | CV | EV | PHEV | MHV |
| Energy Converter #1 | ICE | EM | EM | ICE |
| Energy Storage #1 | Fuel Tank | Battery | Battery | Fuel Tank |
| Energy Converter #2 | - | - | APU | - |
| Energy Storage #2 | - | - | Fuel Tank | Flywheel |
| Powertrain Variant | 1 | 2 | 3 | 4 |

However, it ought to be mentioned that the layout of the MPS will allow the implementation of many more types of powertrain components (and thus creating a larger selection of powertrain topologies), as long as the power "bond" between each powertrain component is observed. The power "bond" is essentially the communication line between the energy storage, energy converter, and power transformer. Each power bond is modelled in terms of effort and flow. This is based on the same distinctions used for Bond Graph modelling, as discussed in Chapter 3.

The following are examples of efforts and flows for their respective energy domains:

- Mechanical: torque and angular velocity
- Electrical: voltage and current
- Hydraulic: pressure and volume flow rate.

The switching mechanism within the framework is facilitated by the "Variant Subsystem" feature of Simulink [142]. Each energy storage and energy converter subsystem acts as a placeholder which contains a library of components. When the optimiser assigns a powertrain variant to the MPS, the respective energy converters and energy storages are populated. Depending on the powertrain configuration selected by the optimiser, the variant subsystem selects the correct energy converter and energy storage, as defined by the respective Powertrain Variant shown in Table 12.

For example, when the optimiser selects "Variant 1" as the desired powertrain topology, the corresponding energy converter and energy storage is the ICE and fuel tank. Similarly, if the optimiser selects "Variant 2" as the desired powertrain topology, the respective energy converter and energy storage is EM and battery. This is shown in Figure 40 and Figure 41 respectively. In both these non-hybrid topologies, only the

primary energy converter and storage are activated; the secondary energy converter and storage are not applicable and subsequently greyed out. The placeholders for the switching components are outlined in red, and the differences in the components between Variants 1 and 2 can be seen here.

Variants 3 and 4 are the series and parallel hybrid architectures, shown in Figure 42 and Figure 43 respectively. In Variant 3, both sets of energy converters and storages are enabled. The switchable component placeholders are once again highlighted in red to aid clarity when comparing the different topologies. For Variant 4, however, the secondary energy converter is once again greyed-out, because there is no conversion of energy domain between the flywheel and the ICE (both in the mechanical domain).

Another key enabler for the modular powertrain structure is the power split junction box, which can be seen located between the primary and secondary energy converters and storages. The purpose of this junction box it to regulate the power flow between these two systems, depending on the prevailing hybrid powertrain type. For example, in a series hybrid configuration (Variant 3, Figure 42), the junction box switches into series mode, and the power connection between the EM and the battery is enabled. Therefore, the APU supplements electrical power to the EM, in addition to the battery, in this configuration.

Similarly, in a parallel hybrid configuration (Variant 4, Figure 43), the junction box switches into parallel hybrid mode, and the power connection between the gearbox and ICE is enabled instead. Therefore, the flywheel supplements mechanical power between the gearbox and ICE. By controlling the state of the junction box or by disabling it entirely, the modular powertrain structure is capable of simulating series, parallel, and compound hybrid powertrains, as well as non-hybrid powertrains.

The modular structure described so far ensures that the energy domains between the storage and converters are compatible. For example, the EM will only connect to a battery, and not to a fuel tank. The parameterisation of each powertrain component is stored in individual MATLAB m-files. Although not considered in this thesis, Appendix B shows other possible powertrain topologies that could be created using the MPS for future work.

Structures, which are MATLAB arrays with data fields, are used to store information regarding the inputs and outputs of the simulation. The fields of a structure can contain any kind of data. For example, one field might contain a text string representing a name, another might contain a scalar representing a fuel economy result, and so on. The use of structures allowed the toolbox to be better organised and, consequently, provided convenient access to information. The use of structures in handling data is shown in the m-file in Appendix F, which also details the link between powertrain topology and component parameterisation in MATLAB and the MPS in Simulink.

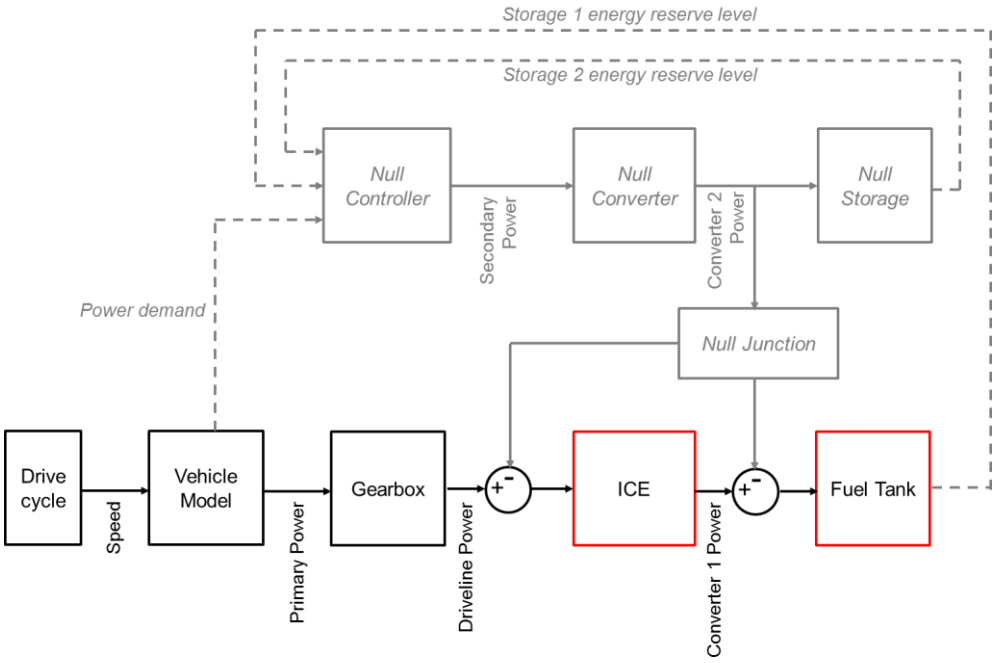


**Figure 40: MPS layout switched to a CV (Variant 1)**

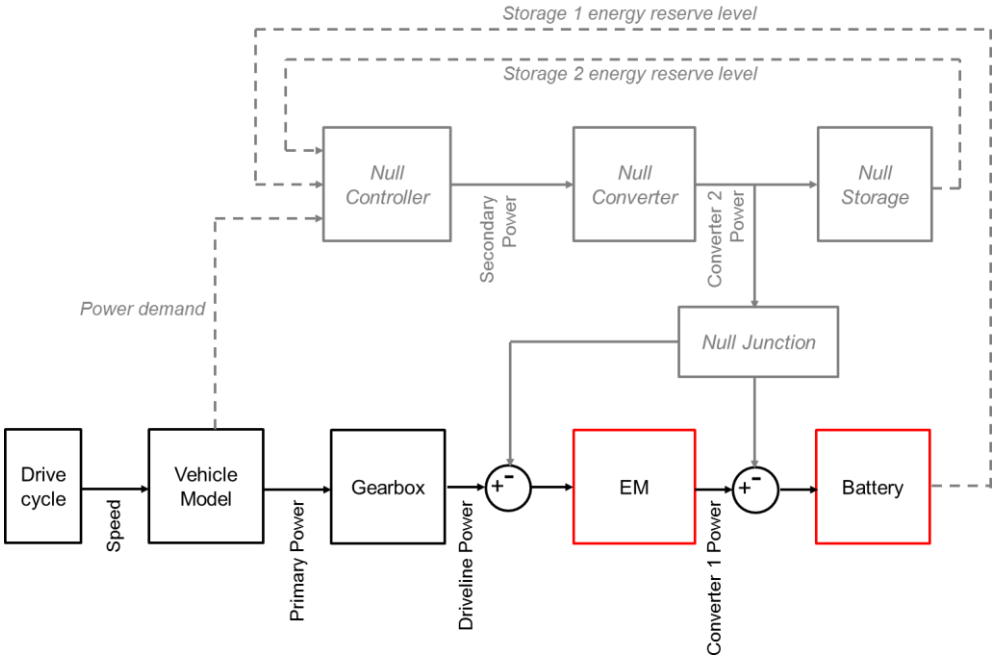


**Figure 41: MPS layout switched to an EV (Variant 2)**

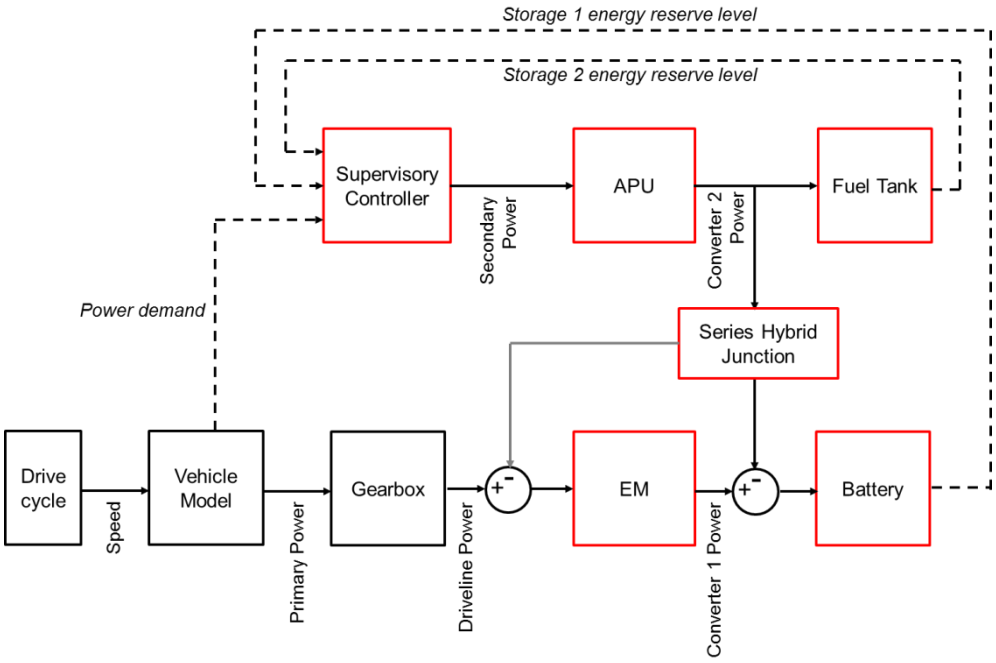


**Figure 42: MPS layout switched to a series PHEV (Variant 3)**

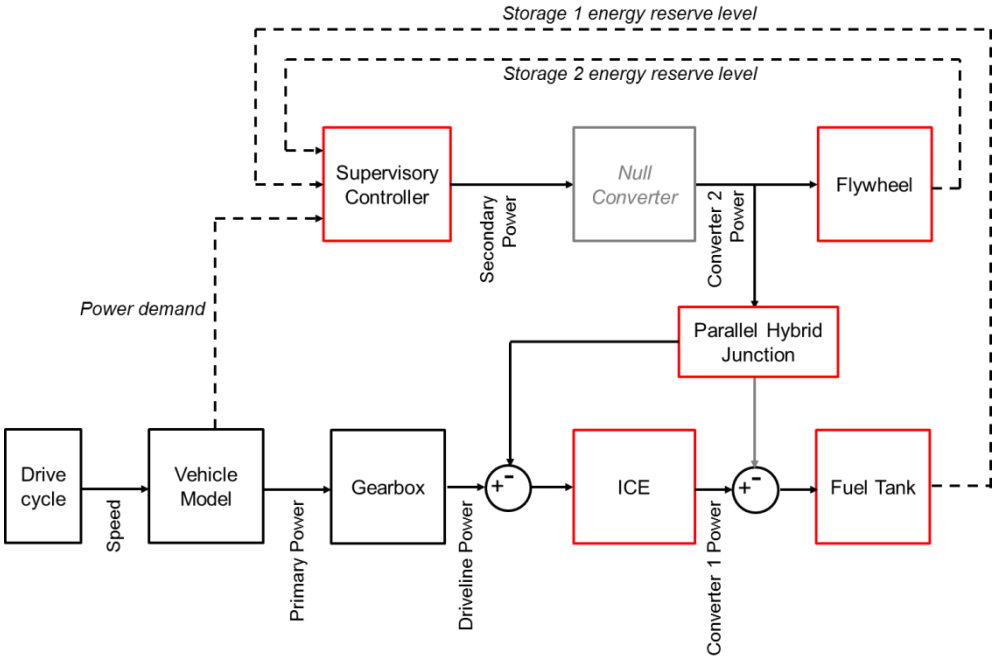


**Figure 43: MPS layout switched to a parallel MHV (Variant 4)**

### 4.1.2 Optimiser

Discontinuities and non-linarites will inevitably be present during the optimisation problem because of switching between different powertrain topologies. For instance, when considering an optimal size between a conventional powertrain and an EV powertrain with regards to minimisation of well-to-wheel $CO_2$ for a given drivecycle, there are two possible solutions or minima. A gradient–based method is less suitable for handling discontinuities in the optimisation problem. Analysis of the existing literature has evidenced that evolutionary computing-based optimisation techniques, such as GA [143] and swarming theory [144], are widely applied to solve complex engineering problems characterised by non-linear and non-convex objective functions [145-147].

As automotive researches are varied, many different kinds of optimisation problems have been successfully approached by employing a genetic-based methodology. These include control of active suspension systems [148], autonomous guidance [149], and automated vehicle control [150]. In the context of powertrain optimisation in particular, GA has been observed to be used for such complex constrained non-linear problems [13; 151-154]. The main advantage of using GA in this application is that, unlike the traditional calculus-based search techniques, GA does not require strong assumptions for the objective function, such as continuity and differentiability. Therefore, based on these findings, a GA-based optimiser was utilised for this purpose. It is noteworthy that other methods, such as simulated annealing, could have also been used in place of GA; however, the aim of this research is on the application of optimisation techniques in the domain of simultaneous optimisation of multiple powertrain architectures, rather than finding the best optimisation algorithm for the problem at hand.

## 4.2 Implementation of the Genetic Algorithm

The optimisation routine can be represented in a standard form [155; 156]. Given a set of decision variables, $X$, and a cost function, $\phi(X)$, the optimiser aims find $X^*$ to minimise $\phi(X)$, within bounds of $G$, where $G$ represents a set of design constraints. This can be represented as,

$$\min_{X_i,G} \emptyset(X) \tag{4-1}$$

where $X_i$ contains the decision variables and can be represented. The GA will be used for optimising the size of the powertrain components and for selecting the most appropriate powertrain architecture to minimise a given cost function. A description of the GA was covered in detail by Goldberg [145], and this technique will be extended for the use of powertrain selection and sizing.

This algorithm was inspired by Darwin's theory of evolution and natural selection, where weak individuals are eliminated, leaving only the fittest ones to survive [145;

157]. Using the optimisation of an EV powertrain as an example, the same technique will be applied, where inferior EV powertrain configurations are discarded, leaving only good and feasible configurations to be selected. The GA initiates by seeding a population of a predetermined number of "individuals", spread homogenously over a solution space that is bounded by the constraints of the decision variables. Each individual can therefore be represented in the form of

$$X_i \equiv \begin{bmatrix} X_1 \\ X_2 \\ \vdots \\ X_n \end{bmatrix} \tag{4-2}$$

where "*i*" represents each decision variable. For example, in an EV powertrain, there are two decision variables per individual:

- EM power (kW)
- Battery size (kWh)

Additionally, each decision variable $X_i$ will have its own bound such that,

$$X_{i_{lower}} < X_i < X_{i_{upper}} \tag{4-3}$$

Based on Equation (4-2), if the index $i_1$ represents the EM and the index $i_2$ represents the battery, the array form for each individual in the EV powertrain optimisation problem will look like,

$$X_i \equiv \begin{bmatrix} EM\ power \\ Battery\ size \end{bmatrix} \tag{4-4}$$

Therefore, each individual can be denoted as an array such as $\begin{bmatrix} 55\ kW \\ 25\ kWh \end{bmatrix}$, $\begin{bmatrix} 40\ kW \\ 60\ kWh \end{bmatrix}$, and so on.

Each "population" will then be a collection of individuals. Each "generation" contains one population. Over each passing generation, inferior powertrain configurations are discarded, leaving only good and feasible configurations to be selected into the next generation, thus adhering to the principles of evolution and natural selection in the GA.

Beginning with an *initial population*, the GA solver then imposes a string of functions such as "mutation" and "crossover". In mutation, an individual is altered to form a new individual. In crossover, two individuals from the initial pool (parents) are reproduced to form two new individuals (children). The inferior individuals are then eliminated from the population, leaving the good individuals ready for the next generation of population. This process continues for subsequent generations to improve the fitness of the individuals towards minimising the cost function. The process terminates after a predefined number of generations, or when the variation of the fitness amongst the individuals is very small (the solution converges). For the EV powertrain example that

will follow in the subsequent sections, the maximum number of generations has been specified as 50 generations for this instance.

### 4.2.1 The Initial Population Generator

The initial population generator is an algorithm used to create an initial population of individuals for the GA solver. In this research, a custom initial population generator was written. This custom generator will be used in lieu of the default one supplied by the MATLAB Global Optimisation toolbox. There are two reasons for this:

- Creating a homogenous spread of individuals within the initial population space
- Verifying that each individual is *feasible*, and therefore can complete a drivecycle.

In this research, the following distinctions are made:

- A population *space* is defined as the area between the largest and smallest bounds for the powertrain configuration. In the case of an EV powertrain, it is essentially the solution space for the component sizes between the upper and lower limits of the scalable EM and battery.
- A *feasible* individual is defined as an individual that is able to complete a given drivecycle successfully. For example, a heavy vehicle with a large EM may not be able to complete a vigorous drivecycle with a small battery pack, due to the possibility of exceeding the battery's power limits. Hence, each individual from the initial population undergoes a simulation run to ensure that they are *feasible*.

By ensuring that each initial individual is feasible, the entire population spread can be used in the GA solver, thus maximising on the solution space and minimising on the potential for the solution tending towards a local minima. This will be verified in Section 4.5.4 by way of repeatability tests in the optimisation results and comparison against an exhaustive search method.

### 4.2.2 Initial Homogeneous Spread of Individuals

To achieve this, the lower and upper bounds of the EM power and battery size are defined. This results in the following inequalities:

$$40kW \leq EM\ size \leq 100kW \quad \textbf{(4-5)}$$

$$10kWh \leq battery\ size \leq 150kWh \quad \textbf{(4-6)}$$

Another constraint is also imposed within the optimiser, which is the maximum vehicle mass,

$$0 < vehicle\ mass \leq 2000kg \quad \textbf{(4-7)}$$

Furthermore, the resolution of the spread of each decision variable across the population space has to be defined. This can be denoted as:

$$iniPopDist = [N_{i1}\ N_{i2}] \quad \textbf{(4-8)}$$

where "*iniPopDist*" is an array containing the resolution of spread for each decision variable (denoted by *N*). If the resolution of the EM size were to have a nominal value of 5 and the resolution of the battery size were to have a nominal value of 10, the array *iniPopDist* will now look like:

$$iniPopDist = [5\ 10] \quad \textbf{(4-9)}$$

The population size can now be defined as:

$$iniPopDist(i_1) \times iniPopDist(i_2) \times iniPopDist(i_3) \times iniPopDist(i_n) \quad \textbf{(4-10)}$$

Therefore, in this example, the population size would be:

$$iniPopDist(i_1) \times iniPopDist(i_2) = 5 \times 10 = 50 \quad \textbf{(4-11)}$$

The matrix for population space, *IP*, is then defined as:

$$IP(population\ size, number\ of\ decision\ variables) \quad \textbf{(4-12)}$$

In this example, "*IP*" will return a matrix the size of 50 rows and 2 columns, as shown in 8.1A.2.1.

This allows the initial population to have a homogenous spread of individuals between the upper and lower bounds of each decision variable, and with the resolution specified in *iniPopDist*. The homogeneous spread of individuals in the population space is further illustrated in Figure 44.

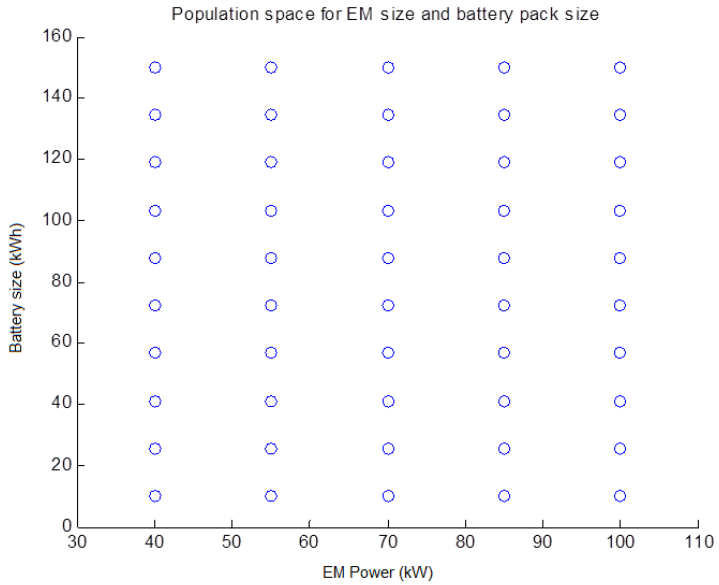


**Figure 44: Initial population spread**

### 4.2.3 Ensuring Each Individual is Feasible

To ensure that each individual is *feasible*, a vehicle model containing each individual is simulated over the specified drivecycle. If the particular vehicle is unable to complete the drivecycle (for example, because maximum EM power is exceeded) or meet the vehicle constraints (for example, exceeding the mass limit), then the individual is tagged with an "inf" value.

However, if the vehicle is able to complete the drivecycle successfully, then the result of the simulation is returned, and this result is the "fitness" of that individual. Individuals that have a fitness value are deemed *feasible*. Conversely, individuals that have been tagged with an "inf" value are regenerated using a "mutation" function, and are re-evaluated. This process repeats until all individuals in a given population are feasible. The mutation function is discussed further in Section 4.5.2.

With the example being used so far, the initial population now looks like Figure 45.

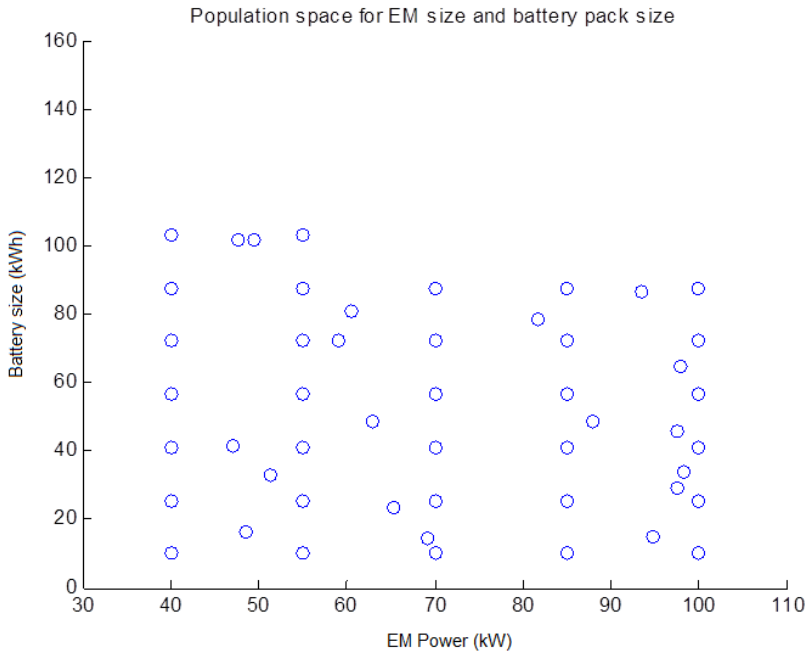


**Figure 45: Initial feasible population spread**

When observing the differences between Figure 44 and Figure 45, there is a noticeable limit with regards to the maximum battery size. The reason for this is that the vehicle mass limit of 2000 kg was exceeded with certain combinations of EM power and battery size.

This initial population can now be input into the GA optimiser, which will further alter the population for up to 50 generations, to estimate the global minimum with respect to the cost function. A flowchart of the complete workings of the GA, as implemented into the proposed framework, is shown in Figure 46.

The m-file script for the generating the initial population is shown in Appendix A, Section A2.

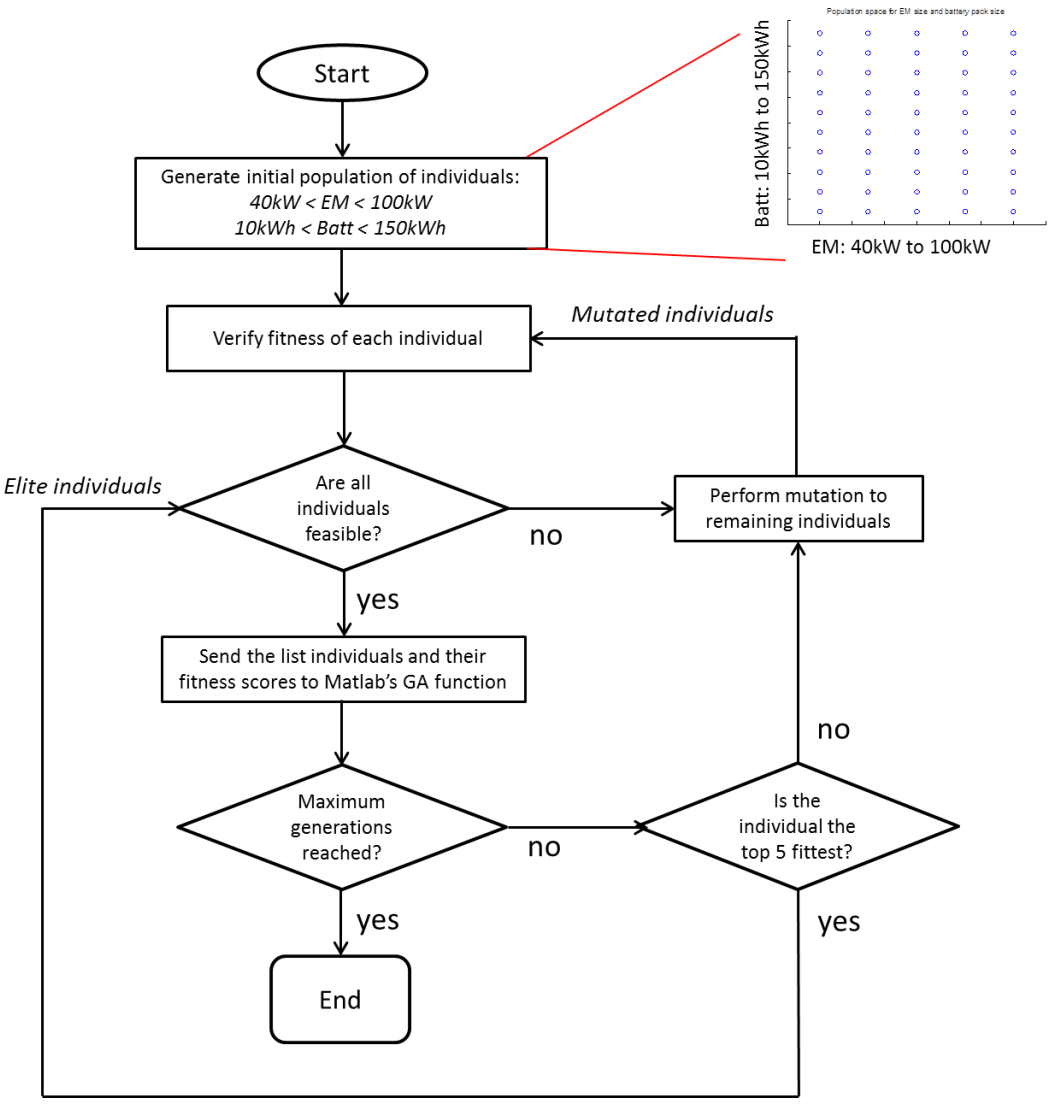


**Figure 46: Flowchart of the implementation of GA in the proposed framework**

## 4.3 Extending the Optimiser to Support Multiple Powertrain Topologies

As discussed in Section 4.2.1, the GA initiates by seeding a homogeneous population of "individuals", spread over a solution space that is bounded by the constraints of the decision variables. In the example of the EV powertrain optimisation shown previously, the decision variables were the EM power and battery size.

In order to extend the optimiser to support more than one type of powertrain topology, the representation of the decision variables will have to be more generic. Therefore, instead of specifying "EM power" and "battery size", the decision variables will now be "energy converter size" and "energy storage size" respectively. This will allow the

inclusion of powertrain topologies that do not contain an EM or a battery, such as the CV powertrain.

Additionally, a third decision variable will need to be added to the individual; the "Powertrain Variant". Hence, the new set of decision variables is:

- Energy converter size (normalised into an integer scale from 1 to 100)
- Energy storage size (normalised into an integer scale from 1 to 100)
- Powertrain variant (discrete selection of 1 to 4, as shown in Table 12).

Therefore, each individual, *X*, now contains three decision variables, which can be denoted by,

$$X = [\text{energy converter size, energy storage size, powertrain variant}] \quad \textbf{(4-13)}$$

By normalising the energy converter and energy storage sizes into a scale from 1 to 100, the optimiser will be able to handle different types of powertrain topologies during a single optimisation routine, while preserving the scaling limits of the associated powertrain components. An example of the normalisation of the powertrain components are shown in Table 13.

**Table 13: Normalisation of the scalable powertrain component sizes for the optimiser**

| Powertrain component | Dimension | Minimum size (scaled to 1) | Maximum size (scaled to 100) |
|---|---|---|---|
| ICE | displacement | 0.5L | 3L |
| EM | power | 40kW | 100kW |
| Battery | capacity | 10kWh | 150kWh |
| APU | power | 10kW | 100kW |
| Fuel Tank | capacity | 10L | 100L |

The value of the decision variable "Powertrain Variant" determines the topology of the powertrain during the optimisation runtime. This interfaces with the MPS, which switches to the appropriate powertrain topology according to this value. Hence, by adding the powertrain variant as a decision variable in the individual (in addition to the components sizes), both the powertrain topology and powertrain components can be optimised simultaneously to minimise a given cost function. This addresses the first novelty of this research, of creating a methodology to simultaneously select a powertrain topology and optimise its component sizes for a given cost function.

## 4.4 Multi-objective Optimisation

For the purpose of multi-objective optimisation, a Non-dominated Sorting-based Genetic Algorithm (NSGA-II) is utilised. This algorithm was developed by Srinivas and Deb [158]. Unlike the single-objective optimisation algorithm discussed so far (i.e. single cost function), it is possible to have more than a single optimal solution in a multi-objective optimisation routine. This is true if the solution to the objectives is in conflict. Therefore, improving one objective (i.e. minimising one of the cost functions) may deteriorate another. A balance in trade-off solutions is achieved when a solution cannot improve any objective without deteriorating one or more of the other objectives. These solutions are called the Pareto optimal solutions. When plotting these solutions, the Pareto optimal curve is created, as shown in Figure 47. Identifying the solutions lying on or near the Pareto-optimal front allows, for example, finding the trade-offs between cost and $CO_2$ emissions.

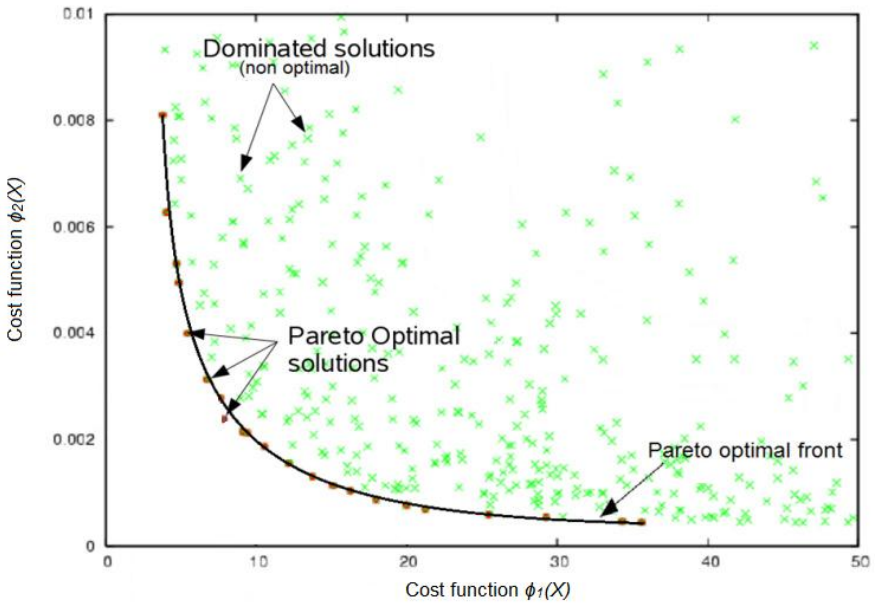


**Figure 47: Pareto solutions example (adapted from** [153]**)**

The use of multi-objective optimisation will be demonstrated in Chapter 7. To carry out the multi-objective optimisation routines, the Global Optimisation toolbox for MATLAB was used via the function *gamultiobj* and is based on the NSGA-II algorithm. This Similar to the single-objective optimisation routine, NSGA-II the sorts the population according to its ranking, where the ranking attribution is performed by comparing the solutions with each other regarding its non-domination level [158]. The objective is to "build" a non-dominated solution set. Further discussions on the NSGA-II algorithm were carried out by Srinivas and Deb [158]; therefore, it will not be repeated here.

## 4.5 Further Additions to the MATLAB Toolbox

In addition to the initial population generator discussed in Section 4.2.1, several modifications were performed to the MATLAB toolbox to cater for the needs of the powertrain selection and sizing optimisation routine. This included the custom rounding function, custom mutation function, and additional considerations for parallel computing.

### 4.5.1 Custom Rounding Functions

Given the variety of the powertrain topologies and corresponding powertrain components, the numerical value of each decision variable may have different significant figures. For example, when optimising the size of the battery pack, the number of strings in parallel will have to be a round number. Conversely, when sizing an ICE, its displacement is rounded to the nearest 0.1 litres. A custom rounding function was created to address the need for each decision variable to have different rounding requirements. By default, MATLAB does not apply any rounding to decision variables.

With the inclusion of the rounding function, the GA will be able to achieve convergence in the fitness of the individuals quicker, and hence terminate the simulation with fewer generations. This is shown in Figure 48, where the optimisation run with the custom rounding function achieves convergence in the fitness function at an earlier generation when compared to the optimisation run using the default MATLAB GA toolbox settings. The fitness values in this example refer to well-to-wheel $CO_2$ per kilometre, for an EV running one increment of the ARTEMIS cycle. The m-file script for the custom rounding function is shown in Appendix A.3.

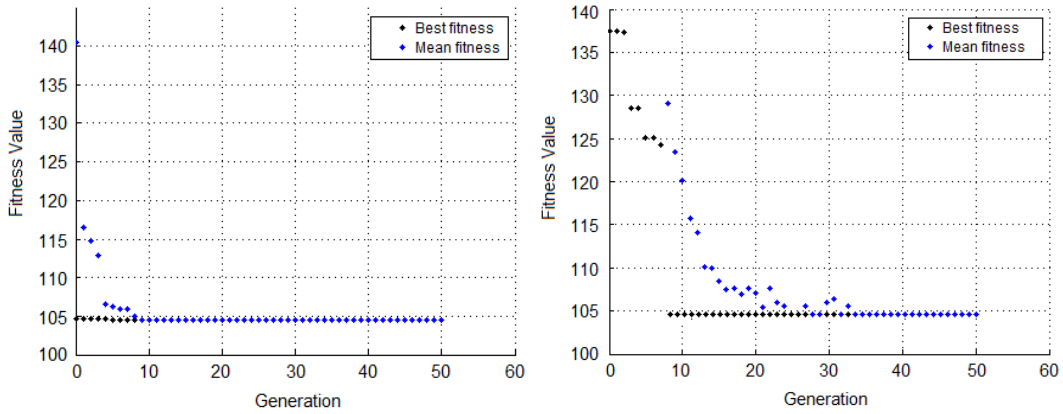


**(a)** **(b)**

**Figure 48: Convergence of solution to obtain the global minimum: (a) Using custom rounding function; (b) Using default MATLAB settings**

### 4.5.2 Custom Mutation Function

The average distance between the individuals of a population is called "diversity". The populations would have a larger diversity in the initial generations than in the final generations. The reduction in diversity as the generation progresses is an indication of the optimiser converging to a solution.

In each generation, five of the best individuals are carried forward to the next generation unaltered. These individuals are called the "elite" individuals. The purpose of this is to reduce the simulation time (increase the performance of the GA), and also to prevent loss of good solutions once they are found [159].

The remaining individuals are then mutated to find a new individual that will potentially offer a solution that is closer to the optimal. Some individuals will also be eliminated, while other stronger individuals could be allowed to create two or more mutated "children".

The children are created via a random number generator. With each passing generation, the size of the "window" on how different the children are with respect to their parents becomes smaller (the diversity reduces).

The reason for pursuing a custom mutation function is to ensure that more of the solution space is searched. Similar to the initial population generator, each child is also regenerated until a feasible individual is formed. If no feasible individuals are found after 10 regenerations, the original child is returned to the MATLAB GA function discarded from the next generation. The m-file script for the custom mutation function is shown in Appendix A.4.

### 4.5.3 Considerations for Parallel Computing

To maximise the use of the supercomputer at Cranfield University, called "Astral", the optimiser had to be able to utilise parallel computing. The Astral supercomputer has 32-processor cores. However, the MATLAB GA function only runs on a single core by default.

To enable support for parallel processing, the parallel for-loop ("parfor" function) was implemented in the code to splice the optimisation into running one individual per processor core. Each individual then runs the respective drivecycle determine its fitness, and the MATLAB GA function will determine if it will be considered an elite individual, mutated, or discarded for the next generation. In the case of the Astral supercomputer, the optimisation tool is able to evaluate the fitness of 32 individuals concurrently.

### 4.5.4 Verification of Modified GA

The custom GA functions were verified against the default functions in the MATLAB GA toolbox in order to compare the differences in simulation times, and to compare the accuracy and repeatability of the solutions. This is summarised in Table 14, where the results of the optimisation of the EV powertrain are shown.

**Table 14: Verification of custom GA functions**

| | Optimisation run | Value of Decision Variables | | Time taken (seconds) |
|---|---|---|---|---|
| | | EM Power (kW) | Battery Size (kWh) | |
| With Custom GA Functions | 1 | 58.0 | 26.0 | 1000 |
| | 2 | 59.0 | 26.0 | 900 |
| | 3 | 58.0 | 26.0 | 1250 |
| Without Custom GA Functions | 1 | 58.3 | 26.0 | 1900 |
| | 2 | 60.2 | 26.0 | 2000 |
| | 3 | 59.5 | 27.0 | 2050 |
| Exhaustive search | - | 58.0 | 26.0 | 12600 |

It is observed that the optimisation runs that include the custom GA functions achieve conversion quicker than that of the standard MATLAB GA functions. Additionally, the results of the optimisation across the three independent runs were more repeatable. However, it ought to be mentioned that the customisations introduced in the GA is applicable for a particular application; in this instance, the optimisations of powertrain components that have a limited and discrete range of values.

## 4.6 Chapter Conclusions

A methodology was created to facilitate the ability to simultaneously optimise the powertrain topology and components sizes. The MPS encapsulates this methodology, and when combined with the optimiser, forms the framework within the proposed toolbox. This framework underscores the first novelty of this research.

The two key enablers for this methodology were the creation a modular powertrain structure and the addition of the extra decision variable called “Powertrain Variant”. The creation of a modular powertrain structure facilitated the support of multiple types of powertrain topologies and allow for the switching of different powertrain

components. The extra decision variable, “Powertrain Variant”, is incorporated into each individual to select the desired powertrain topology during optimisation runtime.

For the purpose of this research, the GA function that is included as part of the MATLAB Global Optimisation toolbox was utilised. However, the following customisations had to be carried out to adapt the GA for optimising powertrain topology selection and component sizing: rounding function, mutation function, and initial population generator.

The optimisation results from using these custom functions were compared against the exhaustive search method and showed negligible variations. The NSGA-II algorithm for multi-objective optimisation was also adapted for use into the framework, thus partly underscoring the second novelty of this research.

# 5 SENSITIVITY OF POWERTRAIN OPTIMISATION RESULTS TOWARDS VARIATIONS IN COST FUNCTION

In this chapter, an EV powertrain will be optimised for each of the three drivecycles discussed in Section 3.7 while utilising the optimiser that was discussed in the previous chapter. The objective of this chapter is to investigate the sensitivities of the optimisation results with respect to different cost functions [23], and in doing so, improve the understanding of the workings of the optimiser for the benefit of Chapters 6 and 7.

Two optimisation routines were carried out using the following cost functions [31]:

- well-to-wheel $CO_2$
- total vehicle mass.

Within the EV powertrain topology, the EM (energy converter) and the battery (energy storage) will be scaled to minimise those cost functions. Each cost function will be evaluated in a separate investigation, and the optimisation results from each will then be compared. The optimisation parameters are summarised in Table 15.

**Table 15: Decision variables (*X*) and constraints (*G*)**

| Term | Definition | Units |
|---|---|---|
| $\phi_1(X)$ | well-to-wheel $CO_2$ | kg |
| $\phi_2(X)$ | total vehicle mass | kg |
| $X_1$ | 10 ≤ EM power ≤ 100 | kW |
| $X_2$ | 8 ≤ battery size ≤ 80 | kWh |
| $G$ | Drivecycle speed constraints | m/s |

After completing the simulations, there were differences observed in the powertrain sizing as a result of the two different cost functions. This will be discussed at the end of this chapter.

## 5.1 Drivecycle Speed and Acceleration Analysis

As discussed previously, there are three types of drivecycles that are being used to evaluate the powertrain architectures. Each drivecycle has a different range:

- NEDC (11 km);
- Cranfield (29.8 km);
- ARTEMIS (73 km).

To evaluate the vehicle performance over an extended range, each drivecycle was repeated back-to-back. An example was shown in Figure 33 (page 57), where the NEDC was repeated twice.

Based on Figure 49(a), the ARTEMIS cycle has the highest top speed whist the Cranfield cycle has the highest average speed. The NEDC has the largest discrepancy between top speed and average speed.

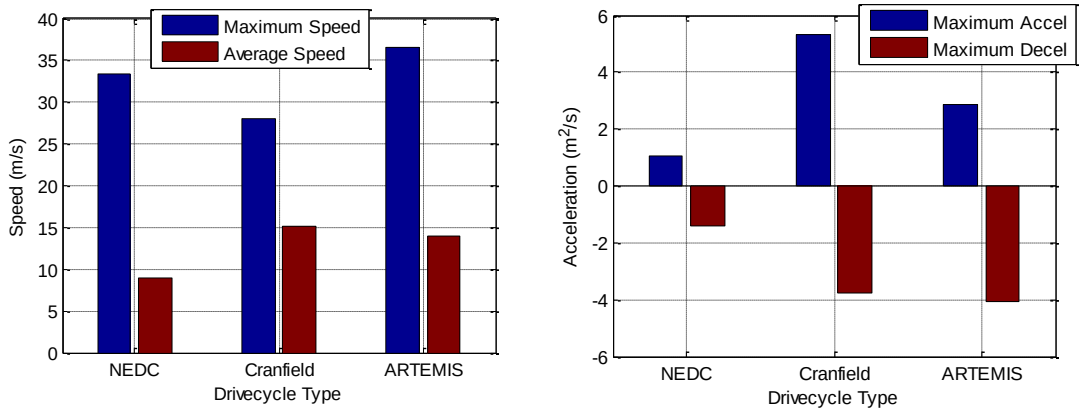


(**a**) (**b**)

**Figure 49: Comparison of speed and acceleration in each drivecycle: (a) maximum and average speeds; and (b) peak accelerations**

When observing the acceleration profiles in Figure 49(b), the Cranfield cycle has the highest acceleration level, whilst the ARTEMIS cycle has the highest deceleration level. The NEDC has the lowest peak accelerations, but has similar average acceleration and deceleration levels to the Cranfield cycle, seen in Figure 50(a).

Based on these acceleration data, it was deduced that the average acceleration of the ARTEMIS cycle varies by more than 8 % when compared to the NEDC, whilst the peak acceleration varies by more than 104 %. This drastic variation in acceleration is one of the primary causes for variation in emissions between the real-world and legislative cycles. From further comparison to the NEDC, it can be argued the ARTEMIS cycle is also more representative of real-world driving conditions.

Figure 50(b) shows the spread of acceleration occurrences for the three drivecycles. It is observed that the NEDC is less transient than the Cranfield and ARTEMIS cycles. Based on Figure 50(b), the Cranfield cycle would require a powertrain with an energy converter (EM or ICE) that has a relatively higher power output when compared to the other drivecycles. This is to allow the vehicle to sustain a larger spread of positive acceleration. In any case, both Cranfield and ARTEMIS cycles provide more opportunity for regenerative braking when compared to the NEDC, due to the larger spread of deceleration events.

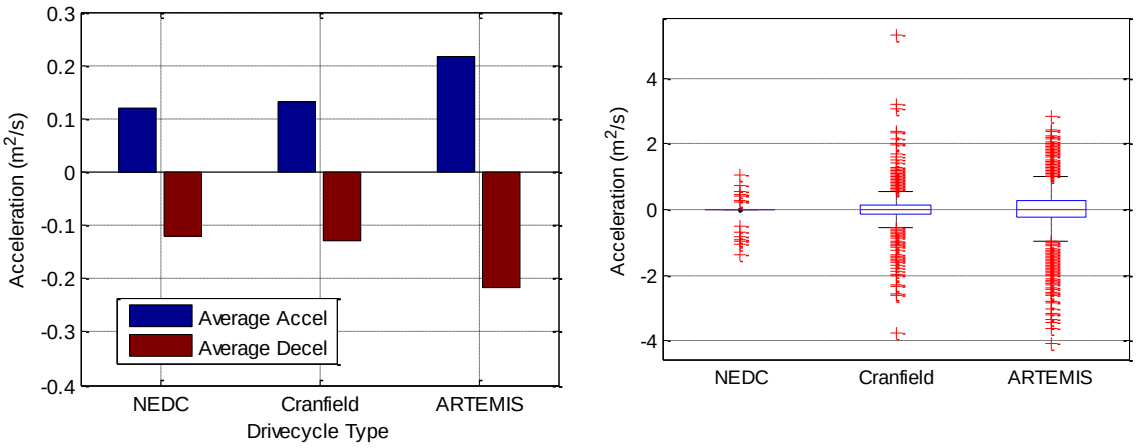


(**a**) (**b**)

**Figure 50: Analysis of accelerations in each drivecycle: (a) average accelerations; and (b) spread of acceleration occurrences**

## 5.2 EV Powertrain Optimised for Lowest Well-to-Wheel $CO_2$

In this investigation, the cost function $\phi_1(X)$ is well-to-wheel $CO_2$. The results of the optimisation are shown in Figure 51 and Figure 52. It is noteworthy that for a given battery pack size, the shortest travel range is achieved during the ARTEMIS drivecycle. Similarly, the highest well-to-wheel $CO_2$ emission also points to the ARTEMIS drivecycle.

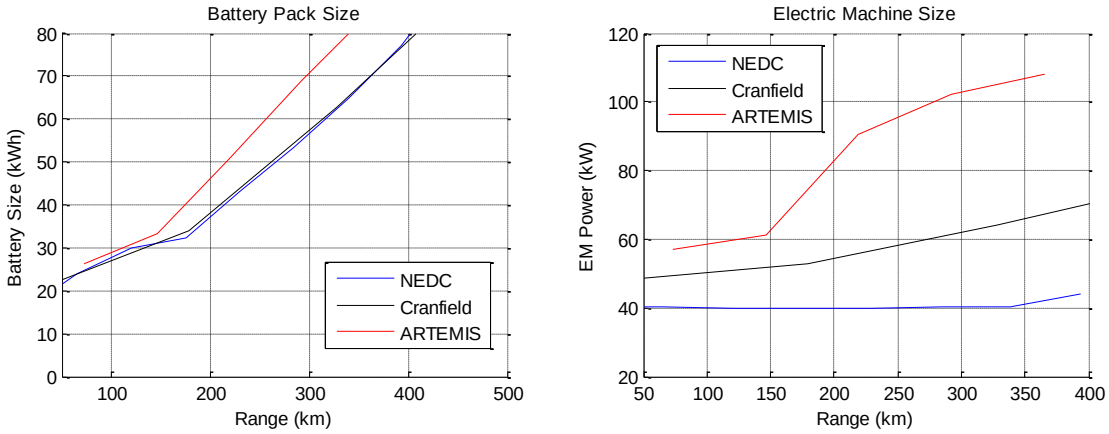


**(a)** **(b)**

**Figure 51: Optimisation results for lowest well-to-wheel $CO_2$: (a) battery pack size; and (b) EM size.**

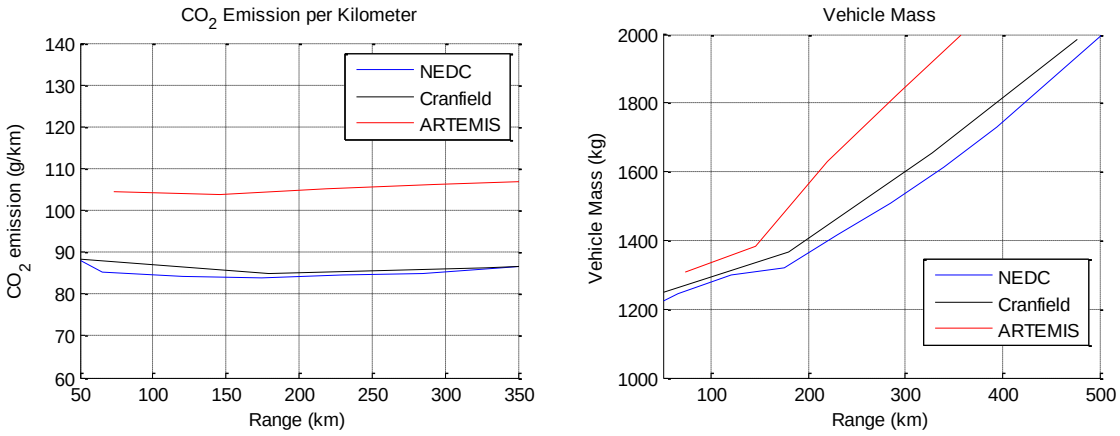


**(a)** **(b)**

**Figure 52: (a) $CO_2$ emission per km; and (b) vehicle mass when optimised for lowest well-to-wheel $CO_2$.**

The battery sizes between the Cranfield cycle and the NEDC were comparable because of similarities in the net amount of energy required to complete these drivecycles for a given range (approximately 600 kJ/km). This correlates with the observation made in Figure 50a, where the NEDC has similar average acceleration and deceleration levels to the Cranfield cycle. Conversely, the size of the EM is different due to higher absolute acceleration level in the Cranfield drivecycle when compared to the NEDC, as seen in Figure 49a.

## 5.3 EV Powertrain Optimised for Lowest Vehicle Mass

In this investigation, the cost function $\phi_2(X)$ is vehicle mass. The two most significant results are shown in Figure 53; battery pack size (a) and total vehicle mass (b). It is noteworthy that the battery start at a lower size in Figure 53a, when compared to that shown in Figure 51a. This will be discussed in the next section. Other trends are observed to be similar between the two cost functions, such as when the vehicle optimised for the ARTEMIS drivecycle once again having the lowest travel range for a given battery size.

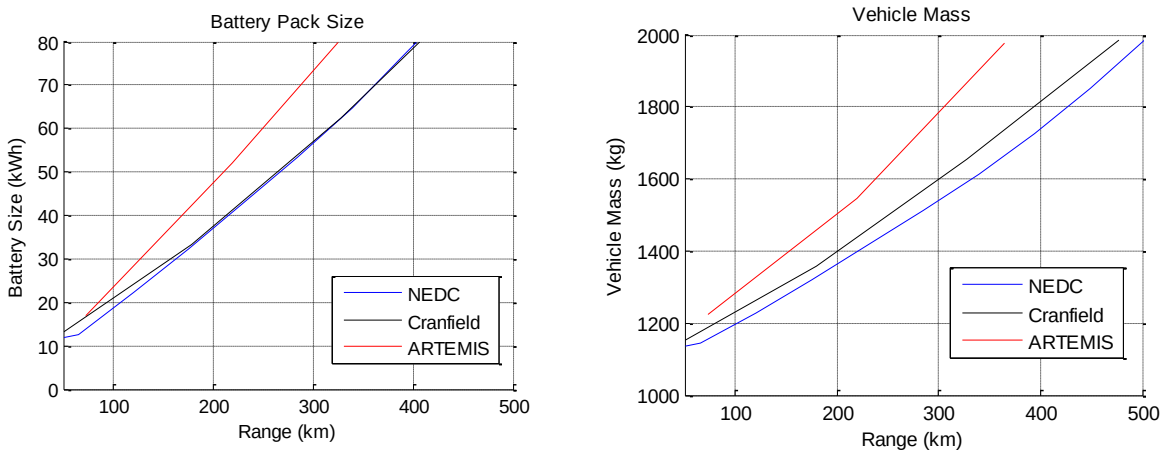


**(a)** **(b)**

**Figure 53: Optimisation results for lowest vehicle mass: (a) battery pack size; and (b) total vehicle mass.**

## 5.4 Comparing the Results of the Two Cost Functions

The first comparison aims to identify the differences observed in the optimised EM size for the two cost functions, using the ARTEMIS cycle as an example. Figure 54a shows the EM sizes with respect to increments in travel range, with blue and red lines reflecting optimised sizes for lowest well-to-wheel $CO_2$ and lowest vehicle mass respectively. When taking a travel range of 200 km as an example (green line in Figure 54a), the resultant efficiency map and scatter of EM power usage over the drivecycle is created (Figure 55). Figure 54b shows the difference in brake regeneration ability between the two different EM sizes. The EM optimised for well-to-wheel $CO_2$ has a higher power rating, and therefore recovers more braking energy when compared to the EM optimised for vehicle mass. This is further illustrated in Figure 55.

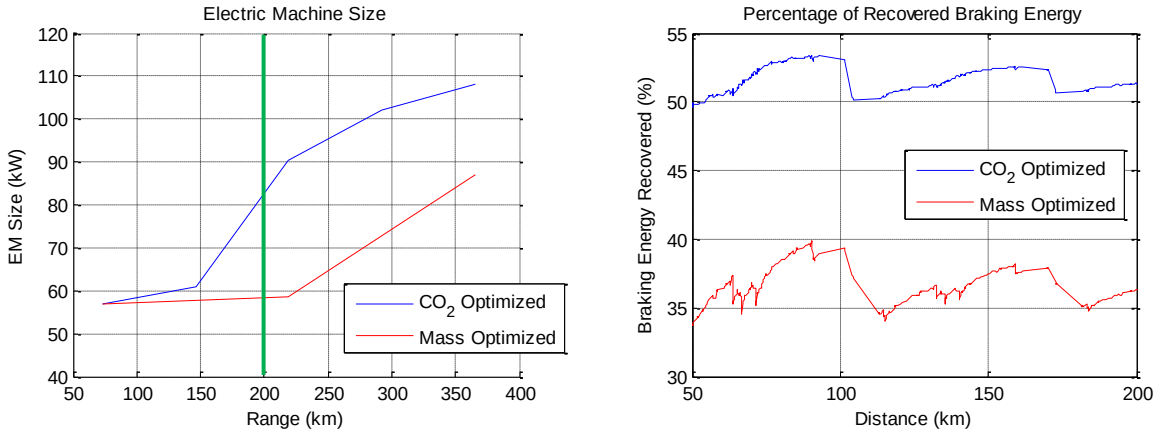


(**a**) (**b**)

**Figure 54: Comparison of EM characteristic over the ARTEMIS drivecycle: (a) EM size; and (b) Percentage of recovered braking energy.**

The white scatters in the negative torque region are braking points encountered during the drivecycle. To minimise well-to-wheel $CO_2$, the EM has to recover as much braking energy as possible. Given the regenerative braking strategy imposed, this necessitated a larger EM to accommodate as much of the regenerative energy as possible.

Conversely, when optimised for smaller mass, the EM was sized just large enough to be able to handle the positive torque demands of the drivecycle, at the expense of regenerative braking abilities. This can be observed in Figure 55b, where the white scatter plots in the positive torque region are closer to the power limits of the EM.

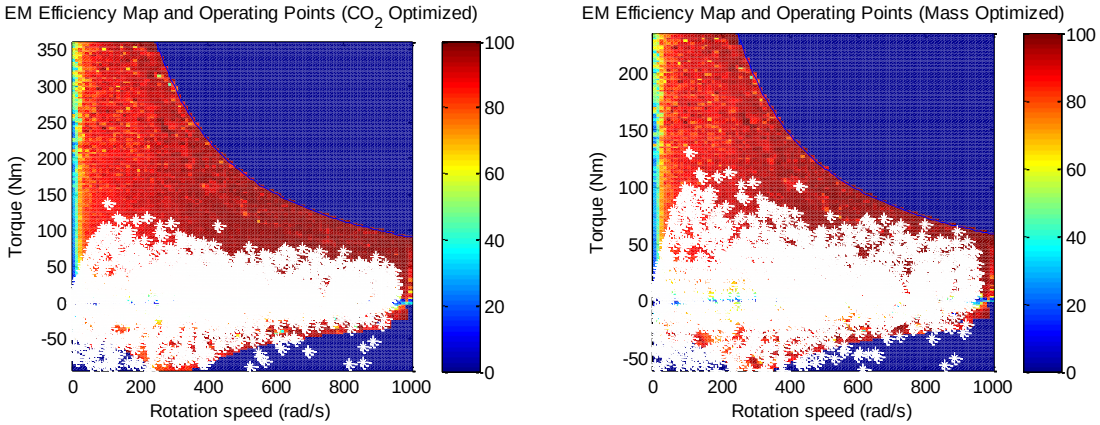


(**a**) (**b**)

**Figure 55: Comparison of EM efficiency and usage over the ARTEMIS drivecycle: (a) optimised for lowest well-to-wheel CO2; and (b) optimised for lowest mass.**

The second comparison aims to identify the differences observed in the optimised battery size for the two cost functions, using the NEDC as an example. For a travel range of 66 km (green line in Figure 56a), it is observed that the vehicle that was optimised for well-to-wheel $CO_2$ features a larger battery pack compared to the vehicle that was optimised for mass. This is further validated in Figure 56b for the same travel range, where the vehicle that was optimised for mass has a higher $CO_2$ output per kilometre, despite having the smaller battery (and therefore lighter) of the two vehicles.

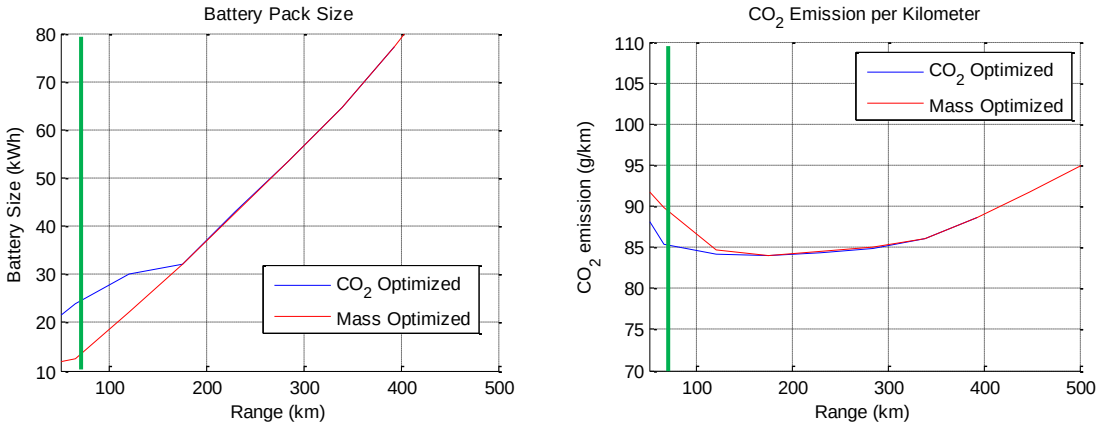


**(a)** **(b)**

**Figure 56: Comparison of battery pack size and $CO_2$ emission over the new European drivecycle (NEDC) drivecycle: (a) battery pack size; and (b) well-to-wheel $CO_2$ per kilometre.**

The reasoning to support this finding can be inferred from the histograms in Figure 57. In Figure 57a, a smaller battery pack encounters higher C-rate levels to provide the same amount of propulsion power. Therefore, although the battery pack is lighter, it is less efficient because of higher power losses, $P_{b(loss)}$, as given by,

$$P_{b(loss)} = I_b^2 \cdot R_b \tag{5-1}$$

where $I_b$ is the current flowing through the battery, and $R_b$ is the battery internal resistance. This difference in efficiency is reflected in Figure 57b, where the efficiency of the battery, $\eta_b$, is defined as .

$$\eta_b = \frac{P_b}{P_b + P_{b(loss)}} \tag{5-2}$$

where $P_b$ is the power demand from the battery.

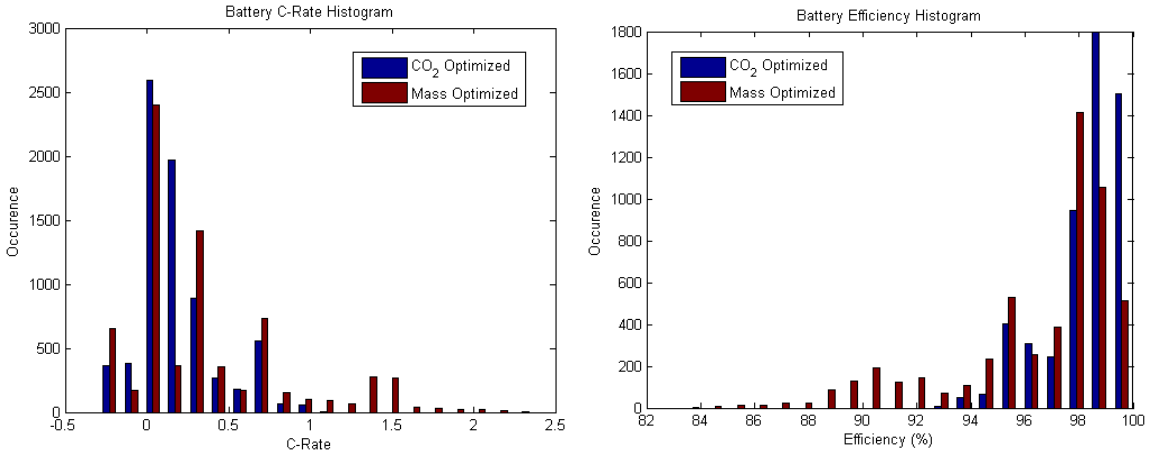


**(a)** **(b)**

**Figure 57: (a) Battery C-rate; and (b) efficiency histogram for EV sized for 66 km of NEDC.**

However, for travel range greater than 150 km, the influence of the battery pack's mass becomes more dominant. Therefore, the resultant battery pack sizes from both cost functions converge and yield almost identical $CO_2$ emissions, as observed in Figure 56b. Here, it is also noteworthy that the lowest point for $CO_2$ output per kilometre occurs at around 175 km. This finding is discussed in the next section.

The results so far has given some insight on EV powertrain sizing according to cost functions, drivecycles, and range. In the next chapter, this method of optimisation will be extended to other powertrain architectures, as well as giving the optimiser the ability to select the most appropriate powertrain topology to minimise a cost function, given the drivecycle and range.

## 5.5 Further Discussion on Behaviour of Normalised Well-to-Wheel $CO_2$ Emission per Kilometre

To aid this discussion, Figure 58a shows the well-to-wheel $CO_2$ emissions for the EV. The EV was optimised for lowest well-to-wheel $CO_2$ for different increments of the NEDC (the NEDC was repeated up to thirty-five times, to simulate varying autonomy ranges, as discussed in Section 3.7). In Figure 58a, the blue line represents the normalised well-to-wheel $CO_2$ output in grams per kilometre, whereas the green line represents the accumulated (total) well-to-wheel $CO_2$ output in kilograms The x-axis represents the incremental autonomy range that the EV was optimised for.

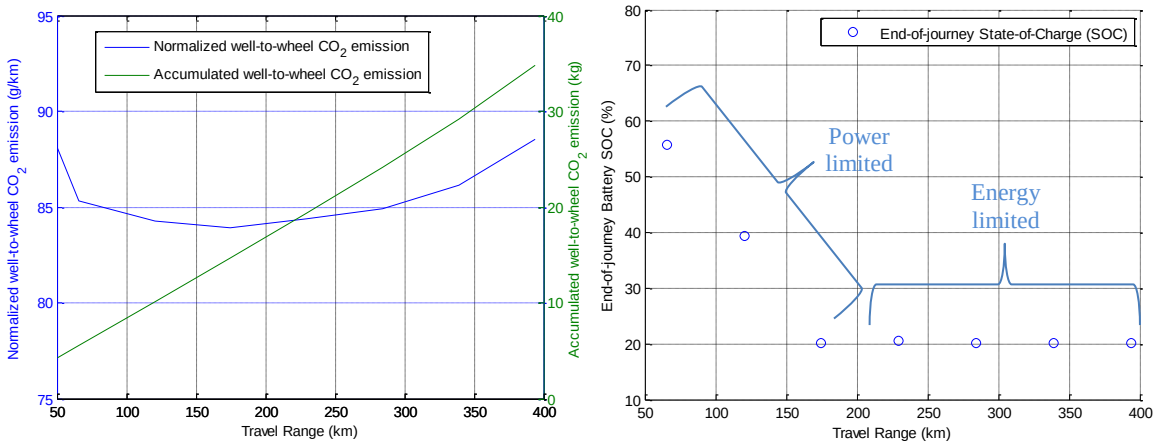


(**a**) (**b**)

**Figure 58: (a) Well-to-wheel $CO_2$; and (b) end-of-journey battery state of charge (SOC) as a function of travel range.**

Referring to Figure 58a, the lowest point for the normalised $CO_2$ output occurs when the EV is optimised for a travel range of approximately 175 km. When the EV is optimised for a larger travel range (more than 175 km), the normalised $CO_2$ emission rises accordingly. This is caused by the increase in vehicle mass, which is mainly driven by the increase in battery size to satisfy the larger travel range (therefore, the battery is energy limited in this instance). Consequently, the increase in vehicle mass creates a compounding effect where more energy is required to propel the EV over the drivecycle. Hence, the larger the travel range that the EV is optimised for, the greater the amount of $CO_2$ is emitted *per kilometre*.

However, it is also noticeable that the normalised $CO_2$ output rises again when the EV is optimised for travel ranges smaller than 175 km. In this scenario, the battery is considered to be "oversized" for travel ranges below 175 km (the battery has more energy capacity than needed to cover the travel range). This is validated in Figure 58b, where it is observed that the remaining battery SOC at the end of the trip increases for shorter travel ranges. If the battery were made smaller, its electrical current limit will be approached or exceeded, because the peak power demand from the drivecycle is almost constant, regardless of travel range (therefore, the battery is power limited in this instance).

Consequently, although the accumulated well-to-wheel $CO_2$ emission is lower for shorter travel ranges, the normalised $CO_2$ emissions is inevitably higher because the battery is underutilised and its extra capacity is considered as "dead weight". However, it is noteworthy that the characteristics shown in Figure 58 could vary depending on the battery C-rate capability and vehicle glider mass, along with other assumptions made in this investigation such as the regenerative braking strategy.

## 5.6 Chapter Conclusions

In this chapter, the optimisation framework, as discussed in the previous chapter, was used to demonstrate influence of different cost functions towards powertrain sizing. The following cost functions were used to optimise the EV powertrain:

- well-to-wheel $CO_2$
- total vehicle mass

Interestingly, results have revealed that the EV with the lightest powertrain may not necessarily emit the lowest well-to-wheel $CO_2$. The discrepancies between the sizing of the battery and EM were more evident at lower autonomy ranges, where the battery efficiency was a deciding factor for $CO_2$ emissions. However, at higher travel ranges, the effect of overall powertrain mass dominated the energy consumption, and therefore the results between the two cost functions converged.

For each of the cost functions, the EV powertrain optimised for an incremental autonomy range. This variation in autonomy range was achieved by multiplying the drivecycles, a trait that will be followed in the next chapters for optimising powertrain topologies based on different autonomy range requirements.

# 6 SIMULTANEOUS OPTIMISATION OF POWERTRAIN TOPOLOGY AND COMPONENT SIZING

This chapter demonstrates the main findings and the first novelty of this research; the ability to simultaneously optimise powertrain component sizing with powertrain topology selection [22]. In the interest of brevity, only a selection of the powertrain topologies that were shown in Table 12 will be used to evaluate the core functionality of this toolbox. These selected topologies are listed in Table 16. Similarly, the cost function $\phi(X)$ that will be evaluated is on minimising well-to-wheel $CO_2$ only. This cost function was selected to follow on from the understanding gained with the optimisations carried out in the previous chapter.

**Table 16: List of powertrain topologies investigated**

| Architecture | Single Power Source | | Series Hybrid |
|---|---|---|---|
| Topology | CV | EV | PHEV |
| Energy Converter #1 | ICE | EM | EM |
| Energy Storage #1 | Fuel Tank | Battery | Battery |
| Energy Converter #2 | - | - | APU |
| Energy Storage #2 | - | - | Fuel Tank |
| Powertrain Variant | 1 | 2 | 3 |

The interface to the proposed toolbox, where the various optimisation parameters are specified, is shown in Appendix A.1. Having discussed the results and workings of the toolbox from this chapter, the next chapter will then include all of the powertrain topologies seen in Table 12, along with additional cost functions.

For this chapter, the optimisation parameters are summarised in Table 17. The decision variable called "Powertrain Variant" relates to the selection of powertrain topology, and corresponds to the last row in Table 16. The normalisations of the components are then shown in Table 18. The framework's role is to simultaneously optimise the powertrain component sizing and topology selection, while meeting the power and energy demands of the respective drivecycle. In this case study, a total vehicle mass limit of 1600 kg is imposed, as the target vehicle class is an E-segment vehicle [160]. The rest of the vehicle parameters were based on the Jaguar XJ, as shown in Appendix C. Similar to the previous chapter, the optimisation is run in multiples of each drivecycle, up to a maximum range of about 450 km. In each run, the vehicle is required to complete the designated autonomy range using only the energy stored on-board (no

refuelling/recharging). The vehicle starts with a full tank of fuel and/or 90% battery SOC.

**Table 17: Decision variables (*X*) and constraints (*G*)**

| Term | Definition | Units |
|---|---|---|
| $\phi(X)$ | well-to-wheel $CO_2$ | kg |
| $X_1$ | 1 ≤ Energy Converter 1 ≤ 100 | - |
| $X_2$ | 1 ≤ Energy Storage 1 ≤ 100 | - |
| $X_3$ | 1≤ Energy Converter 2 ≤ 100 | - |
| $X_4$ | 1 ≤ Energy Storage 2 ≤ 100 | - |
| $X_5$ | 1 ≤ Powertrain Variant ≤ 3 | - |
| $G_1$ | 1000 ≤ total vehicle mass ≤ 1600 | kg |
| $G_2$ | Drivecycle speed constraints | m/s |

**Table 18: Normalisation of the scalable powertrain component sizes for the optimiser**

| Powertrain component | Dimension | Minimum size (scaled to 1) | Maximum size (scaled to 100) |
|---|---|---|---|
| ICE | displacement | 0.5L | 3L |
| EM | power | 10kW | 100kW |
| Battery | capacity | 8kWh | 80kWh |
| APU | power | 10kW | 100kW |
| Fuel Tank | volume | 10L | 100L |

## 6.1 Energy Supervisory Controller

In Chapter 5, the CV and EV powertrains were used as part of the case studies for comparing modelling techniques and investigating cost function sensitivities respectively. In this chapter, those two architectures will be investigated concurrently, with the addition of a third powertrain topology, the series PHEV, as shown in Table 16.

Whilst the CV and EV powertrain had a single power source each, the PHEV has two power sources; the EM and the APU. Therefore, a supervisory controller is required to arbitrate those two power sources. In this research, a thermostatic controller is used as the energy supervisory controller because of its simplicity and well documented use in PHEVs [161; 162]. The thermostat controller allows the battery to deplete from 90% to 20% SOC during charge-depleting mode, and then regulates the battery SOC between 20% and 30% during charge-sustaining mode. An example of these modes is shown in Figure 59. In this example, the vehicle runs for ten increments of the NEDC.

The following are the inputs and outputs of the controller:

- SOC of battery (input)
- Power demand (input)
- Power split (output).

However, this standardised interface allows more sophisticated controllers to be implemented, such as an Equivalent Consumption Minimisation Strategy (ECMS) controller [163; 164]. The implementation of the supervisory controller for the PHEV can be seen in Figure 42 (page 68).

Additionally, optimal power split trajectories from Dynamic Programming can be added as a subroutine within the optimisation algorithm [165; 166]. This subroutine can be encapsulated within the energy supervisory module.

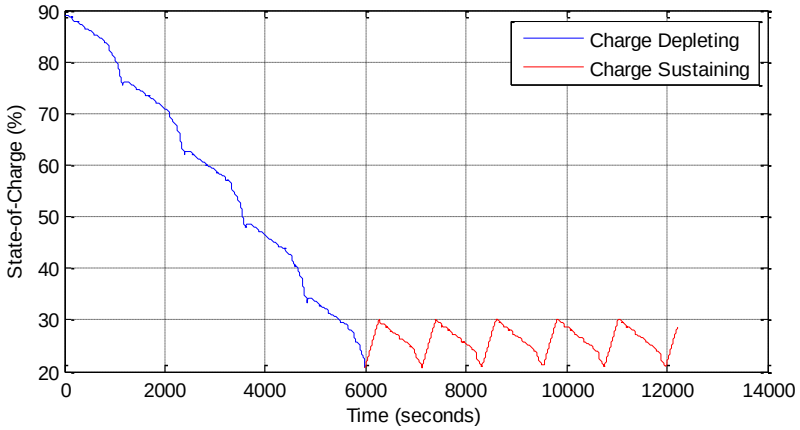


**Figure 59: Operation of the thermostatic controller for the PHEV powertrain**

## 6.2 Optimisation Results

Based on Figure 60, the EV powertrain was selected by the optimiser for travel range increments of up to 230 km on the NEDC. In the Cranfield and ARTEMIS drivecycle however, this reduces to about 210 km and 140 km, respectively.

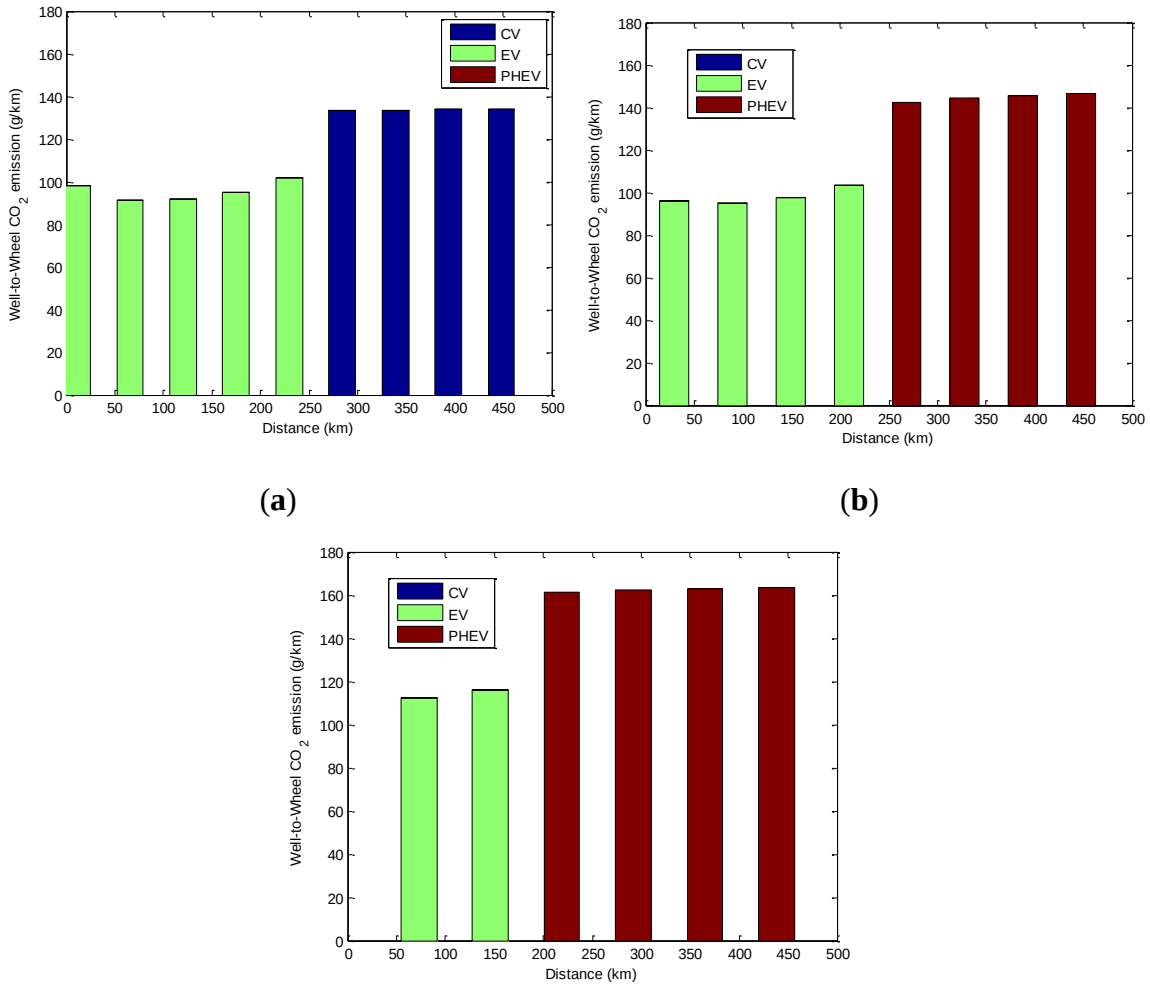


**Figure 60: Well-to-wheel $CO_2$/km emission: (a) NEDC; (b) Cranfield; and (c) ARTEMIS**

The EV powertrain offers the lowest well-to-wheel $CO_2$/km when compared to the CV and PHEV powertrains, for a given drivecycle and range. As a result, the optimiser has selected the EV powertrain for the initial increments of each drivecycle. The crossover from EV powertrain to a different type of powertrain occurred when the vehicle mass limit of 1600 kg was reached or exceeded. The EV powertrain could no longer support a battery large enough to cover the necessary range within the mass limit. This is observed in Figure 61, which shows the total vehicle mass of the respective powertrain and for the range that it was sized for.

To cater for a travel range of over 140 km in the ARTEMIS cycle, for example, a vehicle with an EV powertrain would exceed the mass limit of 1600 kg. Additionally, the increase in vehicle mass as a function of travel range is steeper for the EV when compared to the CV and PHEV. This is because the energy density per unit mass of batteries is smaller than that of fossil fuels by two orders of magnitude [167]. Similarly,

the mass of the battery as a percentage of the total vehicle mass is greater than that of the fuel tank. This is observed in Figure 62, which shows the breakdown of the vehicle masses from Figure 61. The definitions of the respective energy converters and energy storages for each type of powertrain architecture in Figure 61 were covered in Table 16.

In the previous chapter, where only the EV powertrain was optimised, the results indicated that the vehicle had a longer travel range on the NEDC than the ARTEMIS cycle for a given battery size, as observed from Figure 52b. This is because the overall power and energy requirements of the NEDC are lower than those of the ARTEMIS cycle. Referring back to Figure 61, it can be inferred that this is the reason for the transition to happen at a longer range in the NEDC than in the ARTEMIS and Cranfield cycles.

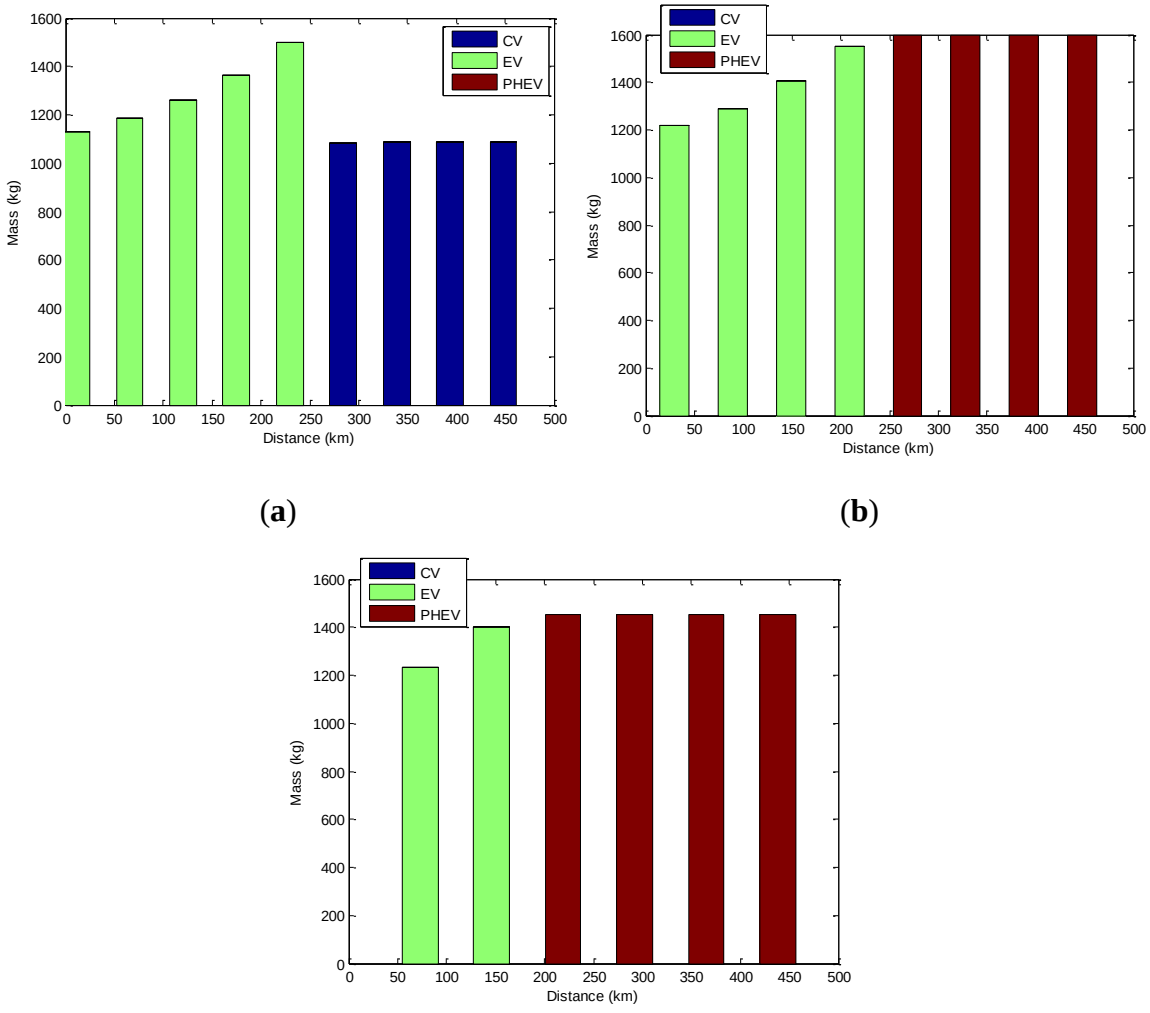


**Figure 61: Total vehicle mass for the respective architectures selected by the optimiser. (a) NEDC; (b) Cranfield; and (c) ARTEMIS.**

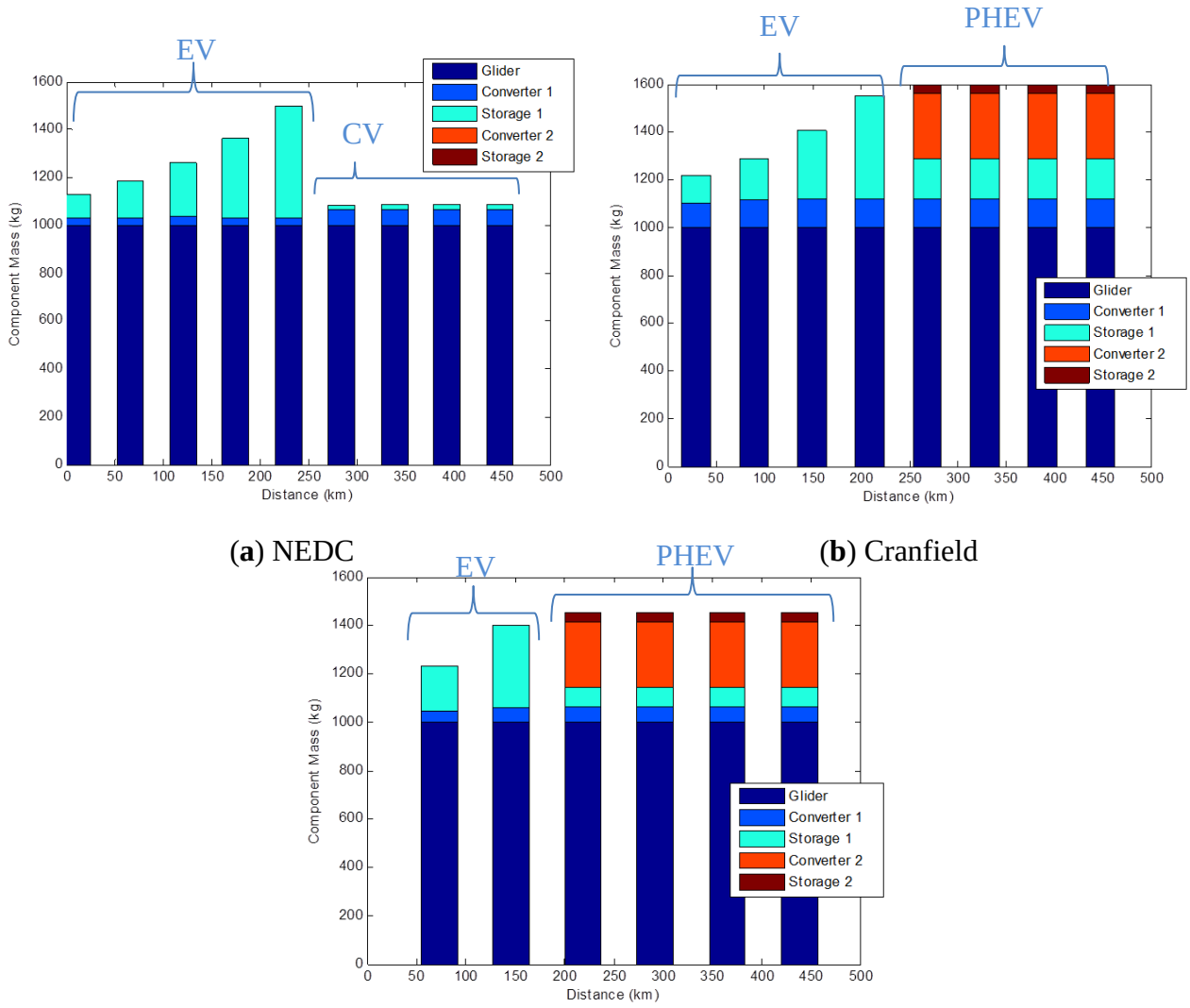


(**a**) NEDC (**b**) Cranfield

(**c**) ARTEMIS

**Figure 62: Breakdown of vehicle mass for each powertrain architecture**

## 6.3 Power and Energy Analysis

As mentioned in Section 3.1.1, the current regenerative braking strategy limits the maximum amount of regenerative power of the EM to 30% of its maximum propulsion power. The regenerative power is also phased out at low EM speeds (under 200 rad/s), as was seen in Figure 20. Additionally, the EM size is a decision variable for the optimiser, and it is scalable between 10 kW and 100 kW.

To minimise well-to-wheel $CO_2$, the EM has to recover as much braking energy as possible. Any deceleration event on the drivecycle that exceeds the maximum regenerative power of the EM will be blended with the friction brakes, which dissipate the energy to the environment as heat.

At minimum, the EM has to be sized just large enough to be able to handle the positive power demands of the drivecycle. This would result in an EM with the lowest possible mass, and subsequently allow the use of a smaller battery, due to the lower electrical current loads. However, as discussed in Section 5.4, the disadvantage of this approach is that a smaller EM would not be able to capture all of the deceleration events, thus sacrificing energy that could have been recovered via regenerative braking. Therefore, one of two outcomes can be expected from the optimiser:

- sizing the EM for lowest overall powertrain mass;
- sizing the EM for maximising energy recovery via regenerative braking.

In Figure 63, a combination of this decision can be seen. For the Cranfield cycle, the EM has been sized to maximise on the regenerative braking, which resulted in an EM with higher power rating than the maximum propulsion power encountered in the drivecycle. This is indicated by the blue dotted lines in Figure 63b.

Conversely, the EM was sized just enough to meet the propulsion power demands on the ARTEMIS cycle, thus sacrificing on recuperated braking energy (indicated by the blue dotted lines in Figure 63c). A consequence of this can be observed in Figure 64b,c, where the percentage of recovered braking energy in the Cranfield cycle is higher than that of the ARTEMIS cycle.

For the NEDC, the result was mixed; the EM was sized for maximum regenerative braking for travel range of up to 120 km, and then it was sized for maximum propulsion power thereafter, as seen in Figure 63a. After the EV powertrain transitioned to conventional powertrain, however, there was no more regenerative braking, and the ICE was sized to minimise its fuel consumption instead.

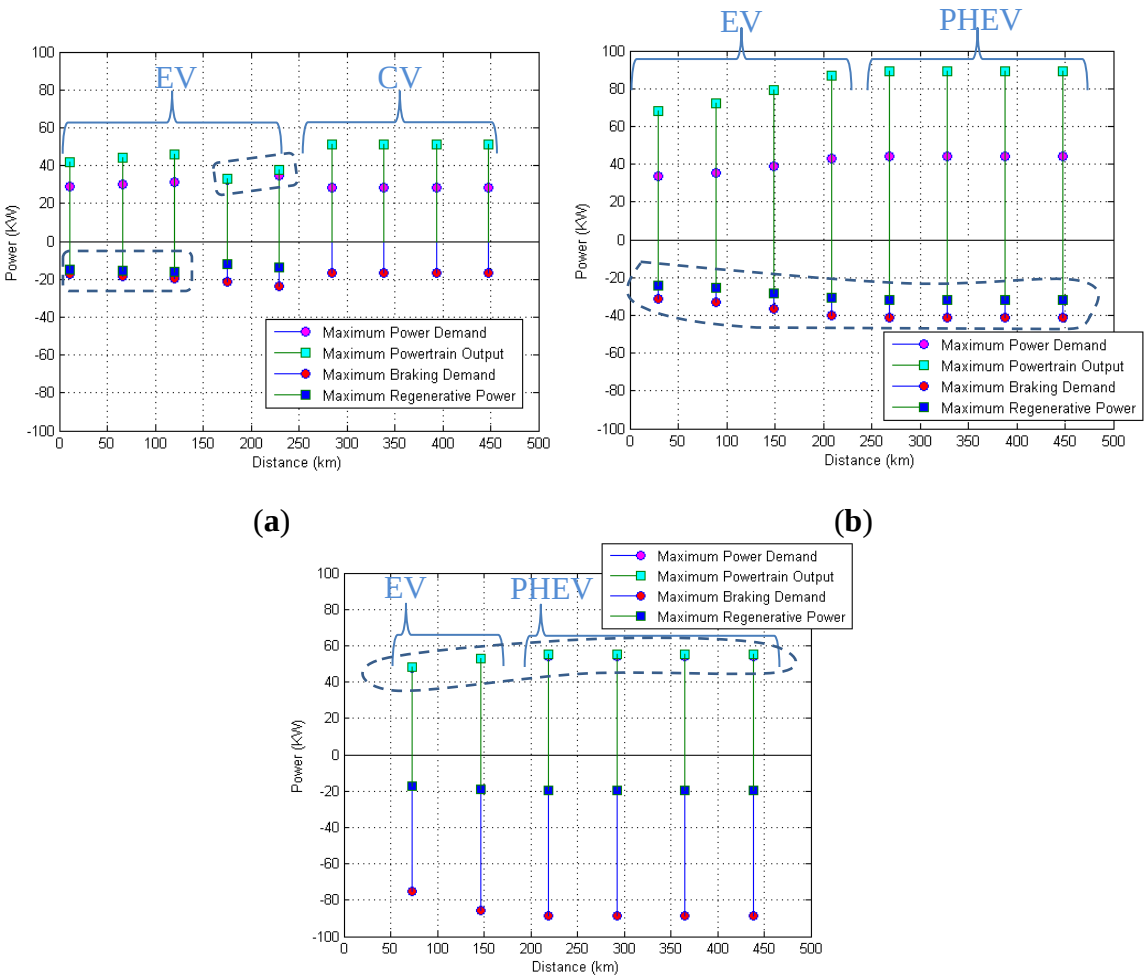


**Figure 63: Drivecycle and energy converter power: (a) NEDC; (b) Cranfield; and (c) ARTEMIS**

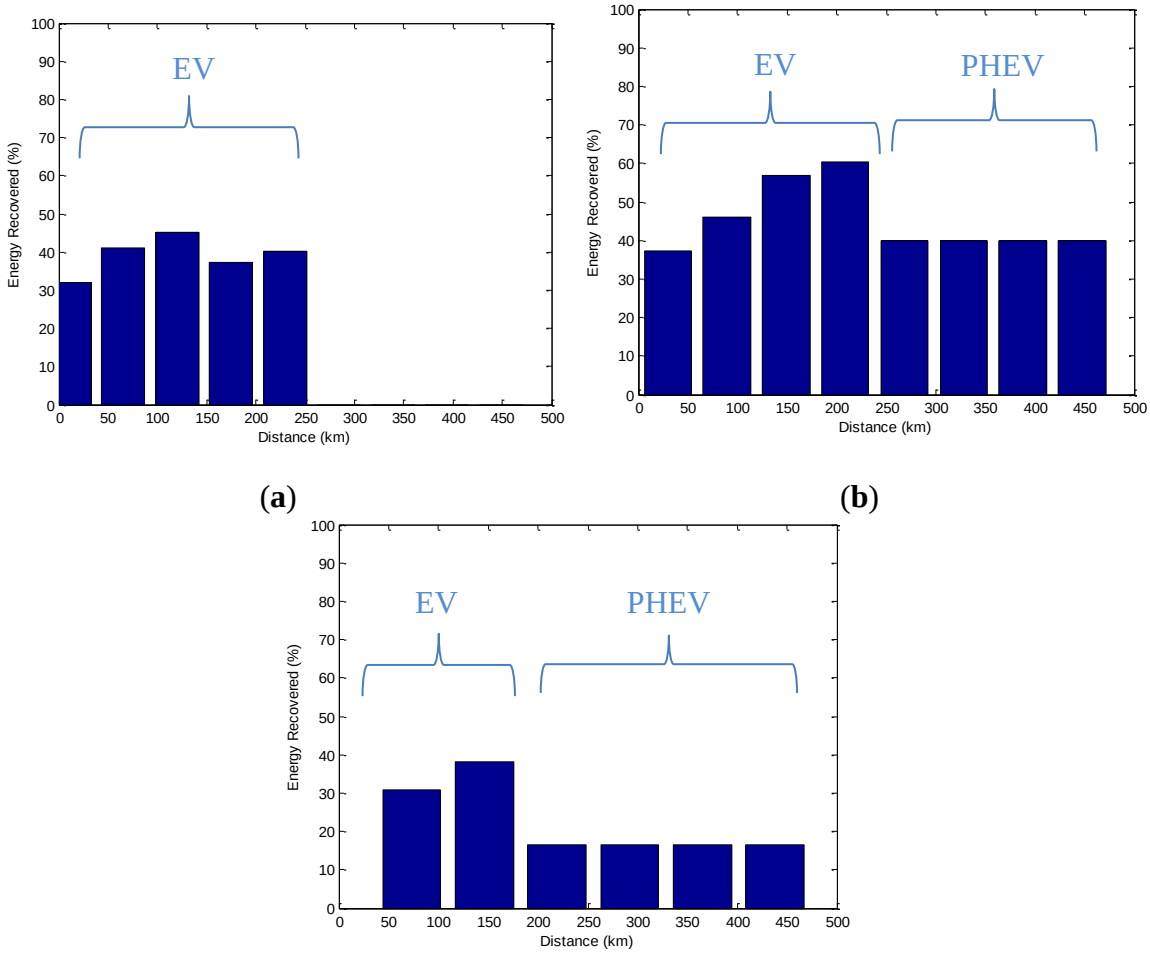


**Figure 64: Percentage of recovered braking energy: (a) NEDC; (b) Cranfield; and (c) ARTEMIS**

One reason to suggest the tendency of the optimiser to scale the EM for minimising mass or maximising regenerative braking can be inferred from Figure 65. The total energy (propulsion and regeneration) required by the ARTEMIS cycle (Figure 65c) is higher than the NEDC (Figure 65a) cycle for a given range. This correlates back to Figure 50b, where there is a larger spread of acceleration events (evident from the longer distance between 25th and 75th percentile lines on the box plot). Therefore, sizing the EM (and subsequently the battery) to maximise brake energy recuperation in the ARTEMIS cycle would have resulted in a powertrain that is heavier, and this would have caused the vehicle to emit more well-to-wheel $CO_2$ per km, despite the increase in regenerative braking capability.

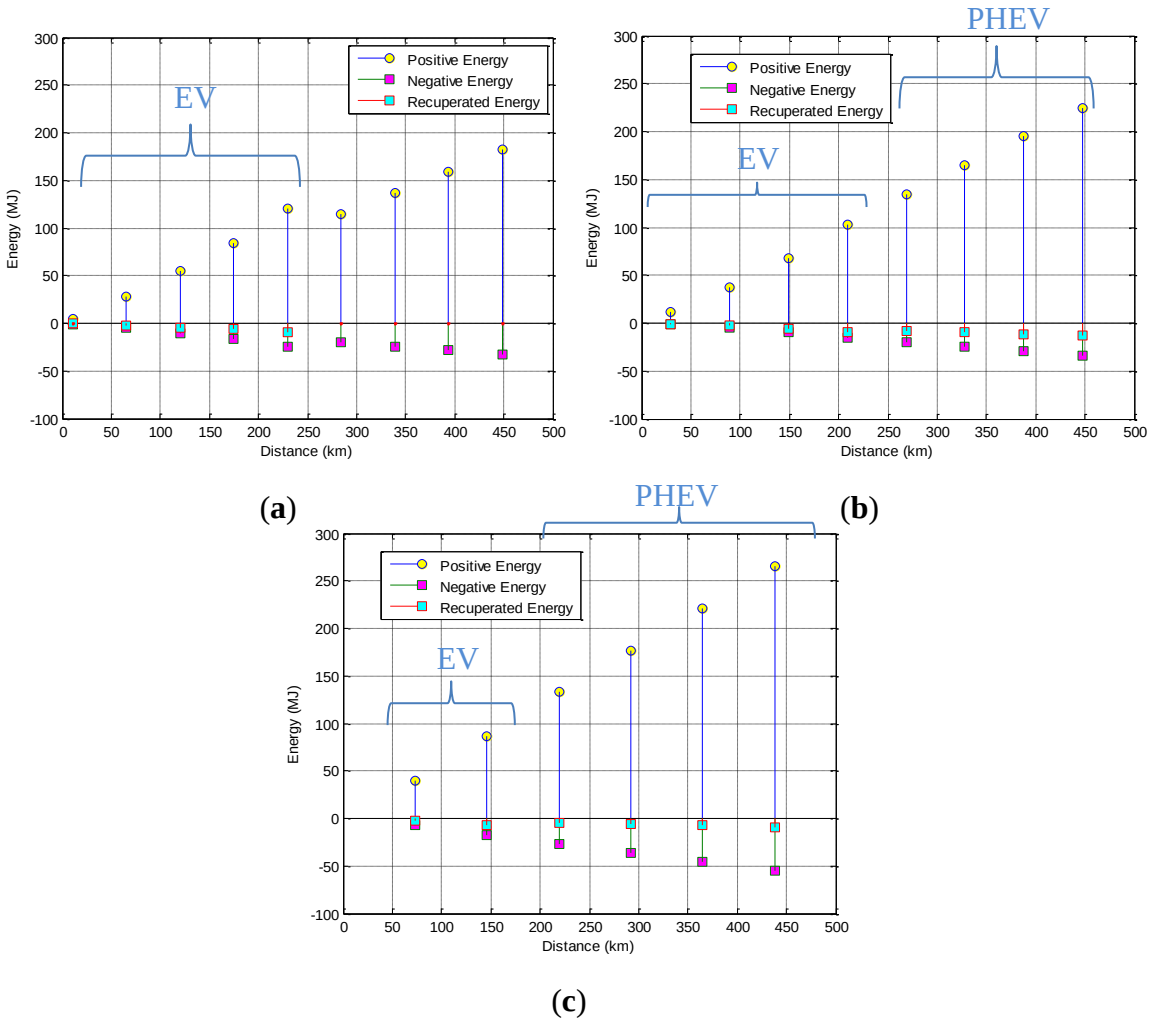


**Figure 65: Total energy from drivecycle and recovered braking energy: (a) NEDC; (b) Cranfield; and (c) ARTEMIS**

It ought to be mentioned that the results presented here are based on the assumptions made during the development of the powertrain components, as discussed in Chapter 3. These results may vary if further uncertainties are introduced into the model, such as component degradation and performance variation caused by changes in operating temperature. Whilst these effects were not considered in this research, the sensitivity of two parameters, the regenerative braking strategy and glider mass, will be investigated in the next section to ascertain their influence in the simulation results.

Additionally, the well-to-wheel $CO_2$ data used for the generation of electrical energy was based on data from the UK grid, and therefore the results will vary based on the grid mix in different countries.

## 6.4 Sensitivity Towards Variations in Parameters

Similar to the study carried out in Section 3.8 for parameter sensitivity at the powertrain-level, this investigation uses the same approach but applied at the topology optimisation-level. The following effects were investigated:

- Variation in regenerative braking strategy
- Change in vehicle glider mass
- Change in vehicle mass limits
- Effects of road inclination
- Variation in electricity grid $CO_2$ emissions.

### 6.4.1 Change in Mass limits

Referring back to Table 17, the constraint for total vehicle mass, $G_1$, was explored further with the limits of 1300kg and 1900kg respectively. The rest of the optimisation parameters, including the vehicle glider mass, were unchanged. The resultant powertrain selection and optimisation from these two different constraints are shown in Figure 66 (NEDC cycle).

For the mass constraint of 1300kg, it is observed that the transition from EV to CV occurs just after the autonomy distance of around 150km. This is because an EV with high autonomy range would require a larger battery, and therefore exceed the vehicle mass constraint of 1300kg. Similarly, for the mass constraint of 1900kg, the transition from EV to CV occurred at a higher autonomy range of about 300km.

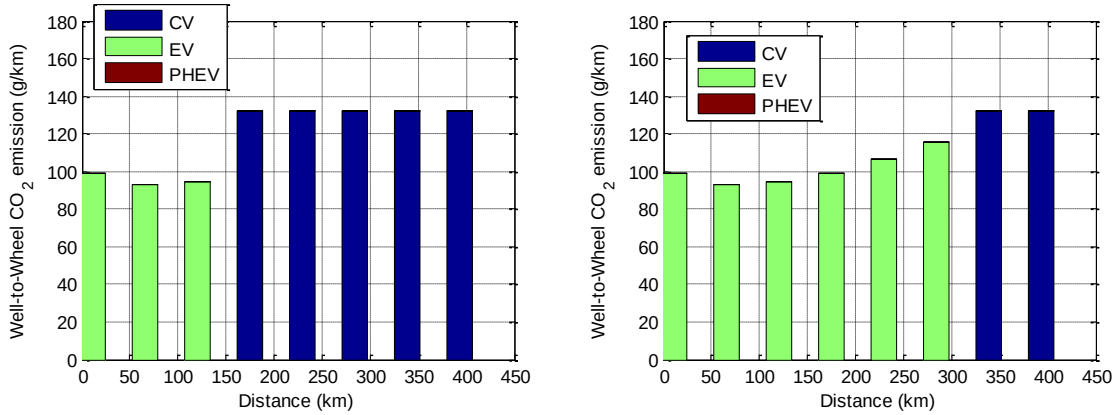


**Figure 66: Optimisation sensitivity towards chance in mass limits: (a) 1300kg; (b) 1900kg**

The reason for the transition can be seen in Figure 67, which shows the total vehicle mass. For the NEDC, the EV powertrain offered the lowest well-to-wheel $CO_2$/km when compared to the CV and PHEV powertrains. As a result, the optimiser selected the EV powertrain for the initial increments of the NEDC. The crossover from EV

powertrain to a different type of powertrain occurred when the vehicle mass constraint of 1300kg or 1900kg was exceeded, respectively.

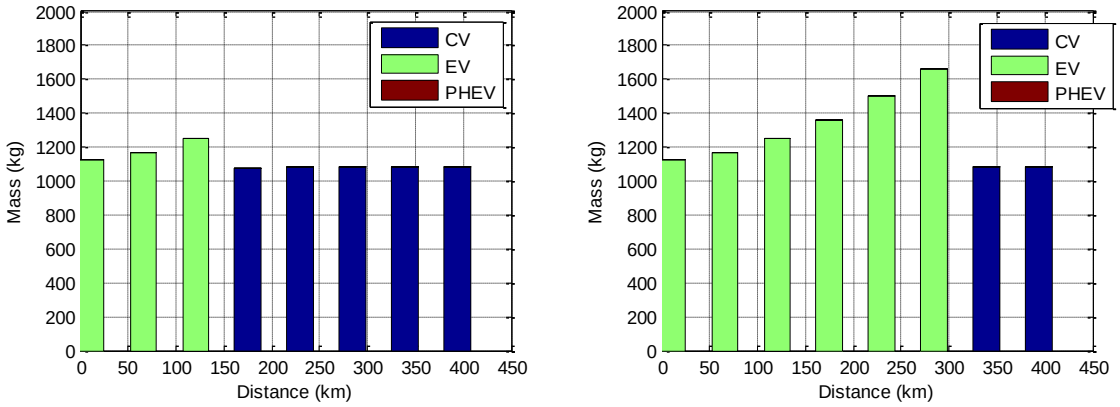


**Figure 67: Total vehicle mass for optimisation mass limits of (a) 1300kg, and (b) 1900kg**

## 6.4.2 Variation in Regenerative Strategy

Figure 68 shows the effects of varying the regenerative braking strategy towards powertrain topology selection and size optimisation. Given its close approximation to real-world usage, the ARTEMIS cycle was selected for this study. Additionally, the ARTEMIS cycle was shown to have the largest effects towards changes in the regenerative braking strategy, as was evident from both Figure 36 and Figure 37.

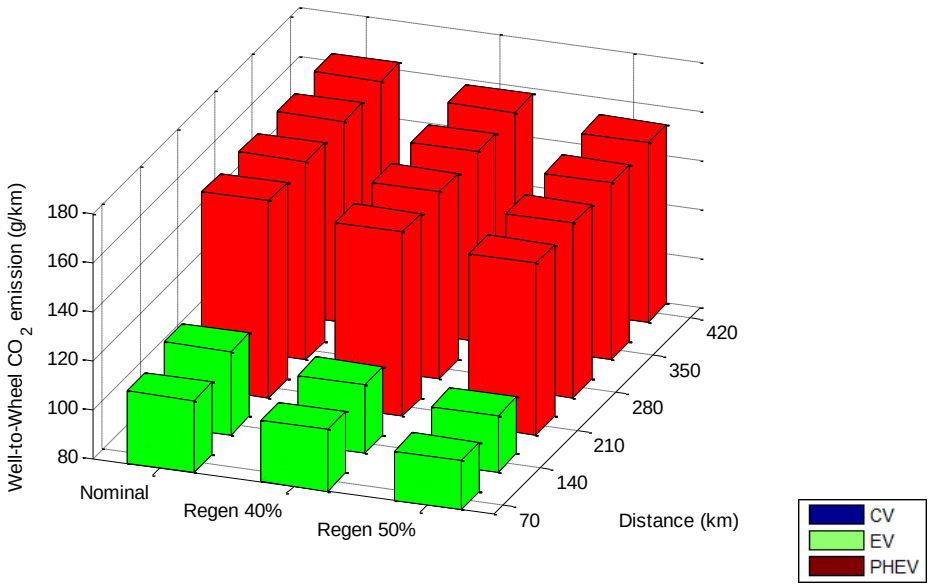


**Figure 68: Optimisation sensitivity towards regenerative braking strategy**

Based on the analysis carried out, the increase in the regenerative power of the EM (as a percentage of the maximum propulsion power) resulted in reduced emissions, which is to be expected. However, the increase in recuperated energy had no effect on the selection of the powertrain topologies in this instance. Other constraints, such as mass limits and energy density of the storage elements, were observed to be more dominant in the selection of the powertrain topology. The transition from the EV to the PHEV still occurred when the mass constraints of the vehicle (1600kg) was exceeded by the EV in order to satisfy the autonomy range for three increments of the ARTEMIS cycle (approximately 210 km). Therefore, the PHEV topology was selected instead as it was able to satisfy the range requirements but within the vehicle mass limits and with lower well-to-wheel emission when compared to the CV powertrain.

### 6.4.3 Change in Glider Mass

In line with the results seen in Section 3.8, the change in glider mass had a more pronounced effect when compared to the change in regenerative braking strategy. This was evident from Figure 69, where the glider mass was increased by 300kg (estimated by adding three more adults and luggage) from the nominal. For the purpose of the optimisation routine, the added mass of the occupants and luggage was incorporated into the glider mass. As a result, the glider mass is now assumed to be 1300kg, and the mass limit of the vehicle was also increased accordingly by 300 kg to a new value of 1900 kg.

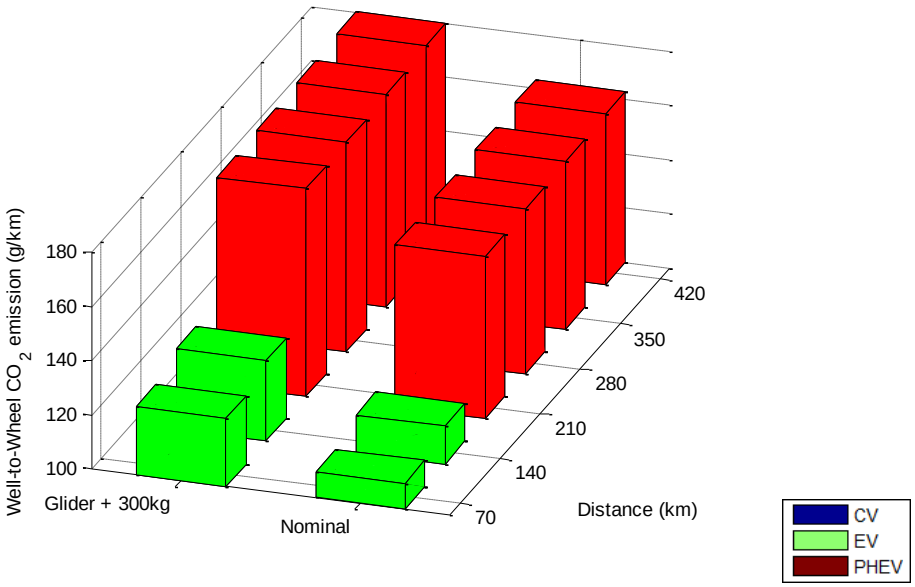


**Figure 69: Optimisation sensitivity towards change in glider mass**

With the increase in glider mass, the optimised sets of component sizes also increased consequently to cope with the bigger power demands from the drivecycle. However, the transition from EV to PHEV was maintained, similar to the sensitivity study of the regenerative strategy. Therefore, although the variations in the parameters affected the sizing of the powertrain at the components-level, the transition at the topology-level was insensitive to the change in glider mass for the ARTEMIS cycle.

### 6.4.4 Effects with Road Inclination

A small test case was carried out to investigate the effects of road inclination on the optimisation results. Since the drivecycles considered in this research lack any information on road inclinations, further customisation was carried out to the NEDC to incorporate such effects. This is seen in Figure 70, where the NEDC was modified to incorporate inclinations between two and five percent gradient. This included both ascending and descending slopes.

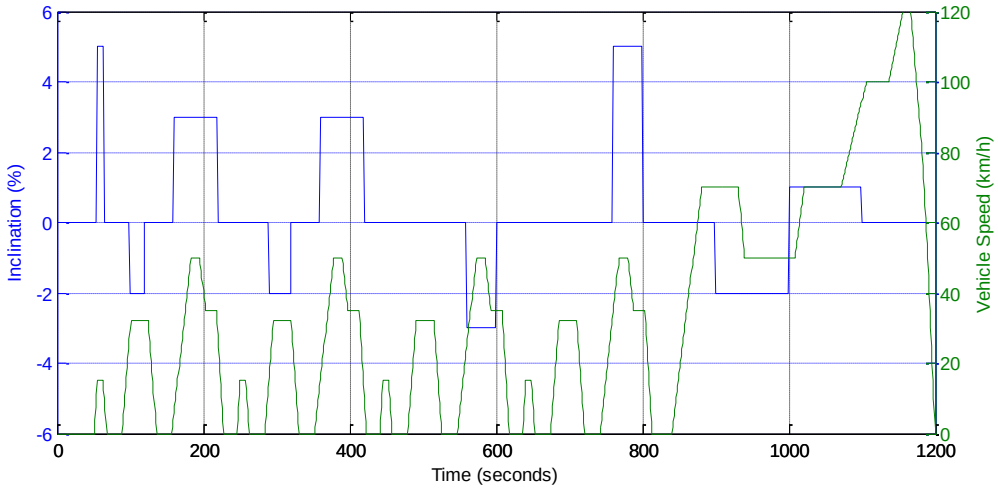


**Figure 70: Modified NEDC with road inclinations**

The gradients were selected based on the observation of the elevation changes around the area of Cranfield University. Figure 71 shows the results of the powertrain well-to-wheel $CO_2$ emissions with and without the effects of road inclination.

For the NEDC without any road inclinations (Figure 71a), the result of the optimisation is such that the EV powertrain is favoured for an autonomy range of up to about 250km, similar to that seen in Figure 60a. After this, the conventional powertrain is selected for the higher autonomy ranges. The results from a PHEV was also superimposed onto Figure 60a as a comparison; and it is observed that the CV has marginally better well-to-wheel $CO_2$ output than the PHEV. The reason for this, as discussed in Sections 5.1 and 6.3, is the combination of the low acceleration levels in the NEDC coupled with the lower overall mass of the CV in relation to the PHEV.

However, when road inclination is imposed onto the NEDC, the reverse is observed; the PHEV was selected by the optimiser over the CV for autonomy distances above 250km. The larger mass of the PHEV was outweighed by the ability of this powertrain to recuperate energy during hill descents. Therefore, it was able to emit lower well-to-wheel $CO_2$ when compared to the CV, causing it to be selected by the optimiser for autonomy distances over 250km.

It is interesting to note that the increase in $CO_2$ emissions is approximately 8% for the EV and the PHEV but 15% for the CV when road inclinations were included. The lower increments for the CV and PHEV can be attributed to the ability to recuperate energy during hill descend. Therefore, considering that the emissions of the CV was just below that of the PHEV on a flat road, it is noteworthy that the effects of inclination has tipped the balance towards the PHEV.

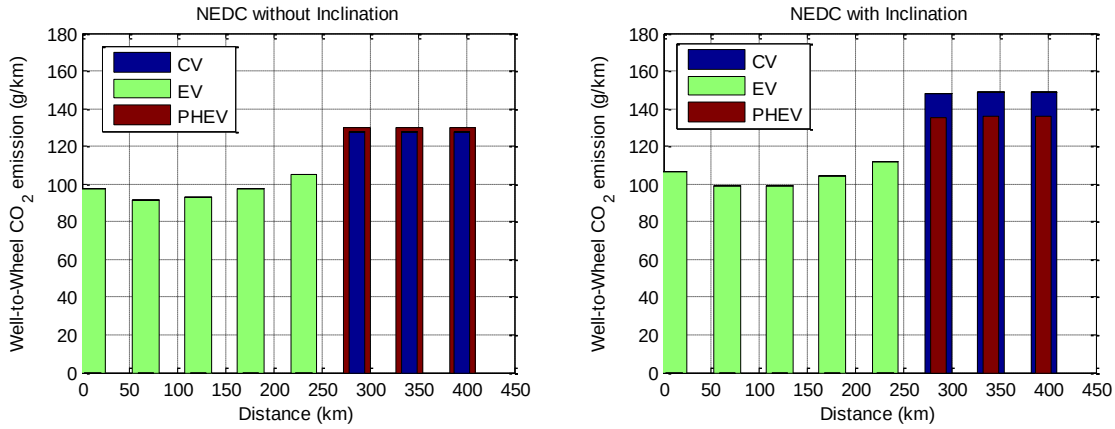


**Figure 71: Results of optimisation (a) without inclination (b) with inclination**

### 6.4.5 Variation in electricity grid $CO_2$ emissions

A test case was also carried out to study the effects of variation in $CO_2$ emissions from the electricity grid mix. In this test case, France was used an example because of its substantially lower $CO_2$ emission per kWh when compared to the UK, at approximately 90 g/kWh [168]. This is because France has significantly lower emission factors for electricity generation, being predominantly nuclear power. As a result, the well-to-wheel $CO_2$ outputs are also much lower, as seen in Figure 72a with the NEDC cycle. Whilst the overall $CO_2$ output is lower, a similar trend can be observed in terms of the transition from one powertrain to another. Beyond the autonomy range of 250km, the PHEV is selected over the EV. This is to satisfy the vehicle mass constraints of 1600kg, a breakdown which can be seen in Figure 72b. As mentioned previously, the vehicle

mass constraints of 1600kg will be exceeded if an EV was selected for autonomy ranges of over 250km on the NEDC.

Unlike the results seen in Figure 60a, however, it is observed that the PHEV is selected over the CV for autonomy range over 250km. This is because the contribution of $CO_2$ from the electricity grid is much lower, and therefore lowered the overall well-to-wheel $CO_2$ emissions of the PHEV, to the point where it is preferred over the CV in this instance.

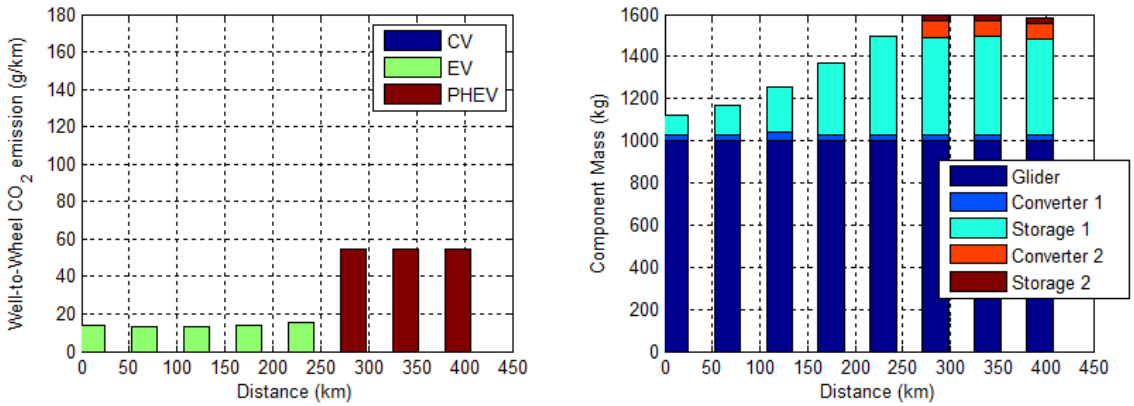


**(a)** **(b)**

**Figure 72: Results from using French electricity grid mix (a) well-to-wheel $CO_2$ (b) powertrain mass**

## 6.5 Chapter Conclusions

Using the methodology proposed in this research, investigations have identified the transition points between powertrain topologies based on the duty cycle and required travel range. This chapter highlighted the core novelty of this research, which is to simultaneously optimise both the powertrain topology and its component sizes for a given vehicle class, duty cycle, and cost function. Although this investigation was limited to three types of powertrain architectures, the flexibility of the MPS will enable additional types of energy converters and energy storages to be included, thus creating further permutations of powertrain architectures.

In this chapter, only one cost function was used to illustrate the workings of the optimisation framework. It was interesting to note that the CV powertrain was selected instead of the PHEV for autonomy ranges of above 250 km on the NEDC cycle. The NEDC is a less demanding cycle when compared to the Cranfield and ARTEMIS cycles, and does not offer as good an opportunity for regenerative braking. As a result, using a PHEV would have resulted in a heavier vehicle without the benefits of reduced emissions.

It ought to be mentioned that the results presented in this chapter are constrained to the power and energy demands of drivecycle. Vehicle manufacturers may also use other measures such as minimum standing start acceleration times to size the powertrain components. These attributes can also be included into the framework by supplementing the drive cycle to include such power demands. Additionally, the well-to-wheel $CO_2$ data used for the generation of electrical energy was based on data from the UK grid, and therefore the results will vary based on the grid mix in different countries, as seen in the case study using the electricity grid mix from France.

Therefore, the aim of this chapter, which is to understand the workings of the toolbox regarding powertrain topology optimisation, was achieved. The insights gained from the results of the optimisation presented in this chapter will be expanded further in the next chapter, with the inclusion of all powertrain topologies discussed in Table 12, as well as additional cost functions to conduct a more rigorous test on the toolbox.

# 7 MULTI-OBJECTIVE OPTIMISATION OF POWERTRAIN TOPOLOGY AND COMPONENT SIZING

In the previous chapter, the core ability of the proposed framework to simultaneously select and optimise powertrain topologies based on a given selection of powertrain components, vehicle parameters, and drivecycle, was investigated. The aim of this chapter is to extend this methodology to include multi-objective powertrain topology optimisation. This addresses the second novelty of this research [24].

Table 19 lists the combination of powertrain architectures that will be investigated, along with the associated energy converters and energy storages. The description for each powertrain component in this table was covered in Chapter 3.

**Table 19: List of powertrain topologies investigated**

| Architecture | Single Power Source | | Series Hybrid | Parallel Hybrid |
|---|---|---|---|---|
| Topology | CV | EV | PHEV | MHV |
| Energy Converter #1 | ICE | EM | EM | ICE |
| Energy Storage #1 | Fuel Tank | Battery | Battery | Fuel Tank |
| Energy Converter #2 | - | - | APU | - |
| Energy Storage #2 | - | - | Fuel Tank | Flywheel |
| Powertrain Variant | 1 | 2 | 3 | 4 |

The cause-and-effect relationship between the drivecycle and powertrain optimisation were investigated and discussed in Chapter 5 (for single powertrain topology) and Chapter 6 (for multiple powertrain topologies). The use of three drivecycles gave an opportunity to understand the variation in topology selection and components sizing because of differing power and energy demands from each drivecycle. For example, the NEDC, being a modal cycle, has lower power demands than the ARTEMIS cycle, and therefore resulted in comparatively smaller powertrain component sizes (for a given topology).

Having established the ability of the framework to simultaneously select and optimise powertrain topologies, the purpose of this chapter is to specifically investigate the area of multi-objective powertrain topology optimisation. Therefore, to keep the investigation concise and to maintain focus on the aims of this chapter, only the ARTEMIS cycle will be used as a case study. Given the vehicle parameters and drivecycle, the toolbox will evaluate the powertrain topologies and create Pareto fronts to show the trade-offs between two cost functions. This will provide insights to

manufacturers and practitioners on the influence of powertrain design targets, such as emissions and powertrain costs.

The normalisations of the powertrain components are shown in Table 20.

**Table 20: Normalisation of the scalable powertrain component sizes for the optimiser**

| Powertrain component | Dimension | Minimum size (scaled to 1) | Maximum size (scaled to 100) |
|---|---|---|---|
| ICE | displacement | 0.5L | 3L |
| EM | power | 10kW | 100kW |
| Battery | capacity | 8kWh | 80kWh |
| APU | power | 10kW | 100kW |
| Fuel Tank | volume | 10L | 100L |
| Flywheel | energy | 100kJ | 600kJ |

## 7.1 Case Study 1: Tank-to-Wheel vs Well-to-Wheel $CO_2$

The definitions of the cost functions that are evaluated in this case study are shown in Table 21. The powertrain optimisation was carried out for each increment of the ARTEMIS cycle, and the results were recorded at the end of each increment. As before, the toolbox's role is to simultaneously optimise the powertrain sizing and architecture selection, while meeting the power and energy demands of the drivecycle.

Three types of optimisation routines were carried out in this case study:

- Single-objective optimisation for well-to-wheel $CO_2$ emission
- Single-objective optimisation for tank-to-wheel $CO_2$ emission
- Multi-objective optimisation combining both the cost-functions above.

For the multi-objective optimisation, the cost function, $\phi_{multi}$, is formulated as a weighted sum of the two individual costs as follows,

$$\phi_{multi} = \beta\phi_1 + (1-\beta)\phi_2 \quad \textbf{(7-1)}$$

where parameter $\beta$ is used to weigh the two costs, and follows the relationship:

$$\beta \in [0,1] \quad \textbf{(7-2)}$$

**Table 21: Decision variables (*X*) and constraints (*G*)**

| Term | Definition | Units |
|---|---|---|
| $\phi_1(X)$ | tank-to-wheel $CO_2$ | kg |
| $\phi_2(X)$ | well-to-wheel $CO_2$ | kg |
| | | |
| $X_1$ | 1 ≤ Energy Converter 1 ≤ 100 | - |
| $X_2$ | 1 ≤ Energy Storage 1 ≤ 100 | - |
| $X_3$ | 1≤ Energy Converter 2 ≤ 100 | - |
| $X_4$ | 1 ≤ Energy Storage 2 ≤ 100 | - |
| $X_5$ | 1 ≤ Powertrain Variant ≤ 4 | - |
| | | |
| $G_1$ | 1000 ≤ total vehicle mass ≤ 1600 | kg |
| $G_2$ | Drivecycle speed constraints | m/s |

### 7.1.1 Lowest well-to-wheel $CO_2$ emission

Figure 73 shows the results for optimising the powertrains for lowest well-to-wheel $CO_2$ emission. The optimisation was carried out for each increment of the ARTEMIS drivecycle. Based on Figure 73, the EV powertrain was selected by the optimiser for the first two increments of the drivecycle (autonomy range of up to 150km).

This was because the EV powertrain achieved the lowest well-to-wheel $CO_2$/km when compared to the CV, PHEV, and MHV powertrains. The transition from EV to PHEV then occurred when the vehicle mass limit of 1600kg was reached or exceeded. The EV powertrain could no longer support a battery large enough to cover the necessary range within this mass limit. This is observed in Figure 74, which shows the total vehicle mass of the respective powertrain and for the range that it was sized for.

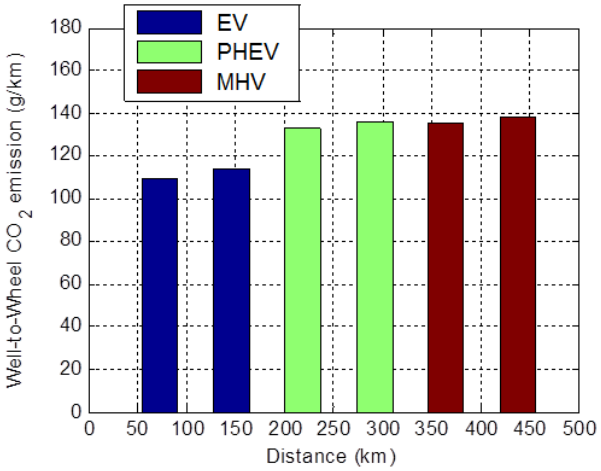


**Figure 73: Well-to-wheel emission**

To cater for an autonomy range of over 150km on the ARTEMIS cycle, a vehicle with an EV powertrain would exceed the mass limit of 1600kg. Additionally, the rate of increase in vehicle mass as a function of autonomy range is steeper for the EV when compared to the other powertrains. This is because the energy density per unit mass of batteries, as discussed previously, is smaller than that of fossil fuels by two orders of magnitude [167].

Another transition occurred between the fourth and fifth increments of the drivecycle, where the MHV is selected instead of the PHEV. In this scenario, it was more efficient to use the lighter mechanical hybrid for the longer travel range instead of the heavier plug-in hybrid. Since the well-to-wheel $CO_2$ encapsulates the total energy used by the vehicle to cover the drivecycle, the heavier PHEV would have emitted higher well-to-wheel $CO_2$ than the comparatively lighter MHV.

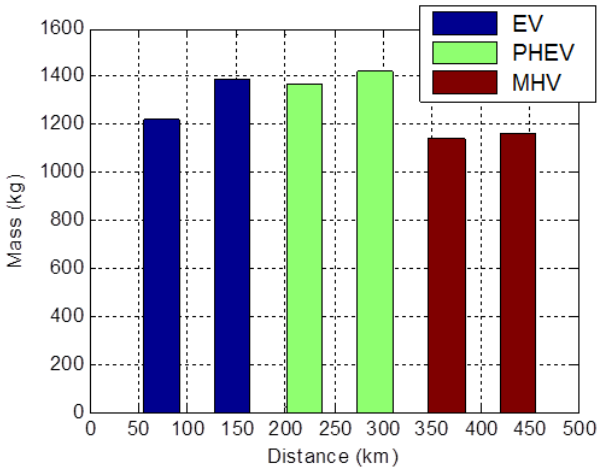


**Figure 74: Total vehicle mass for the respective architecture selected by the optimiser**

### 7.1.2 Lowest tank-to-wheel $CO_2$ emission

Figure 75 shows the results for optimising the powertrains for lowest tank-to-wheel $CO_2$ emissions instead.

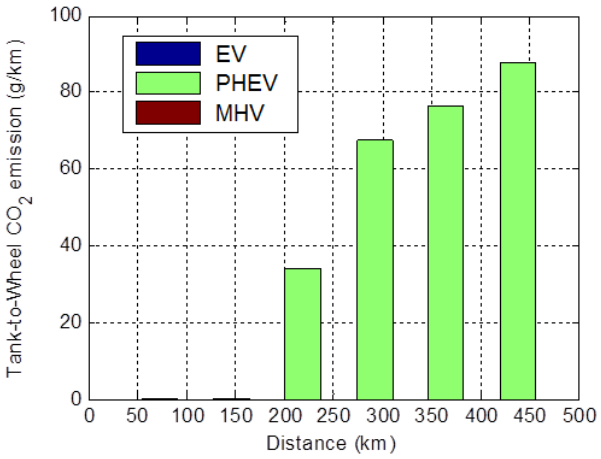


**Figure 75: Tank-to-wheel emission**

When comparing Figure 75 with Figure 73, there are a couple of similarities and differences that can be observed with regards to the selection of powertrain architecture between the two cost-functions. Although not visible in Figure 75, the optimiser has once again selected the EV powertrain for the first two increments of the ARTEMIS cycle. This was not reflected in Figure 75 because the EV powertrain emits no tank-to-wheel $CO_2$ (zero tail-pipe emissions).

In contrast, the PHEV was selected instead of the MHV for the fifth and sixth increments of the ARTEMIS drivecycle. In this scenario, a portion of the energy used to propel the PHEV was sourced "externally" from the electrical grid, as compared to the MHV, which only has a single source of energy from the fossil fuel in its tank. Therefore, the PHEV emitted lower tank-to-wheel $CO_2$ when compared to the MHV in this scenario.

### 7.1.3 Multi-objective optimisation

Unlike the single-objective optimisations carried out previously, there is no single optimal solution for a multi-objective optimisation. For a sweep of the value of $\beta$, as shown in Equations (7-1) and (7-2), there will be a set of points that fit the definition of an "optimum" solution called the Pareto front. Further discussions on multi-objective optimisation and the Pareto front can be found in the work by Marler and Arora [169].

In this investigation, the multi-objective optimisation produced Pareto fronts for well-to-wheel $CO_2$ versus tank-to-wheel $CO_2$. To illustrate the workings of the optimiser, the Pareto fronts from a single increment and from quadruple increments of the ARTEMIS drivecycle are shown in Figure 76 and Figure 77 respectively. In each of these figures, five particular Pareto-optimal points were shown for clarity. These five points correspond to:

$$\beta = [0, 0.25, 0.5, 0.75, 1] \quad \textbf{(7-3)}$$

As a test, based on Figure 76, there was no Pareto front formed after carrying out a multi-objective optimisation on a single increment of the ARTEMIS cycle. This was because the resultant tank-to-wheel $CO_2$ of the selected powertrain (EV) was always zero, regardless of the ratio between the two cost functions. This was also reflected in Figure 75, where the EV powertrain was emitting zero tailpipe emissions.

As a result, the simulation has basically "reverted" to a single-objective optimisation because the tank-to-wheel emission was always equal to zero, and therefore the optimiser only optimised the powertrain for well-to-wheel $CO_2$, thus producing the same results over the entire sweep of $\beta$. Therefore, the optimised EV powertrain produced the same well-to-wheel $CO_2$ output regardless of the value of $\beta$.

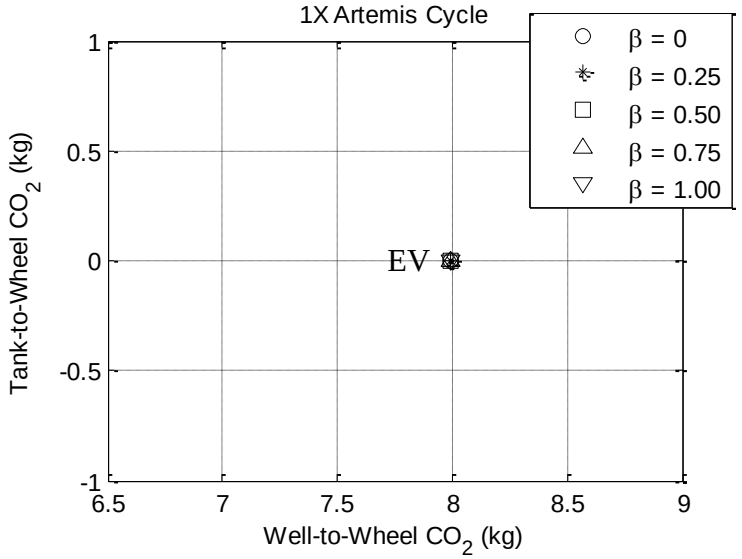


**Figure 76: Pareto front for single increment of the ARTEMIS drivecycle**

In contrast, Figure 77 shows the Pareto front for four increments of the ARTEMIS cycle (around 400km of autonomy range). As discussed previously, the EV powertrain was not selected for higher increments of the ARTEMIS cycle because the vehicle would exceed the mass limit of 1600kg. The remaining powertrain options (CV, PHEV, and

MHV) produce both tank-to-wheel and well-to-wheel $CO_2$ emissions, and therefore generated a Pareto front across different values of $\beta$, as observed in Figure 77.

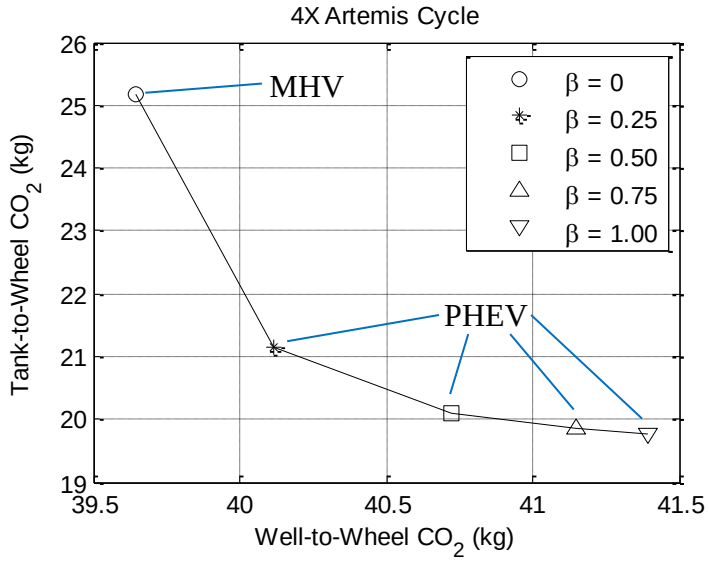


**Figure 77: Pareto front for quadruple increments of the ARTEMIS drivecycle**

Figure 78 combines the Pareto fronts from all six increments of the ARTEMIS cycle. The numbers in circles denote the Pareto front for each specific drivecycle increment. As observed from the single-objective optimisations previously, the EV powertrain was selected for the first two increments of the ARTEMIS cycle regardless of the cost function, because it produced the lowest tank-to-wheel and well-to-wheel emissions. This is also reflected in Figure 78.

For increments 3 – 6 of the ARTEMIS cycle, the powertrain selection is dominated by the PHEV. However, as the ratio of the optimisation favours well-to-wheel $CO_2$ (i.e. as $\beta$ approaches zero), it can be seen that the MHV is selected instead of the PHEV. This relates back to transition seen in Figure 73. It is also noteworthy that the ratio between the selection of the MHV over the PHEV rises as the autonomy range in which the vehicle is optimised for (i.e. drivecycle increments) increases. The shaded regions in between each drivecycle increment are the interpolation of the powertrain topology selected in each Pareto front.

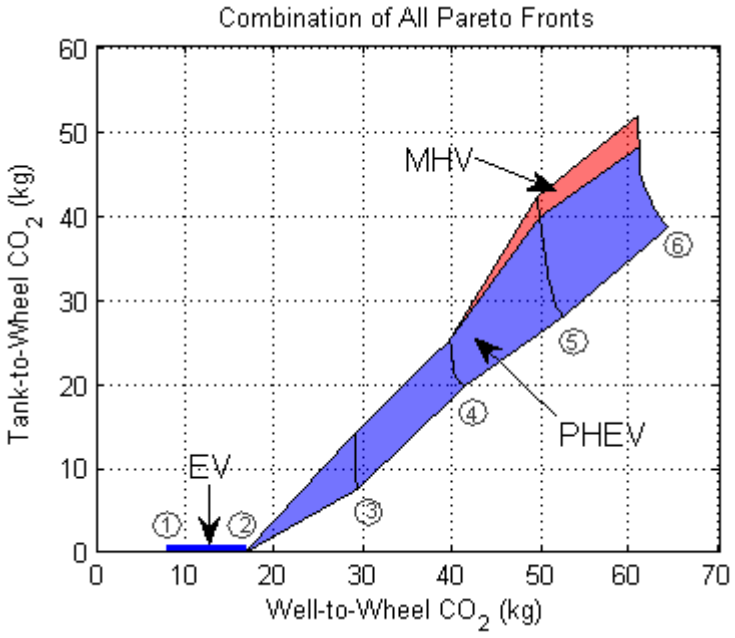


**Figure 78: Sweep of Pareto fronts and powertrain selection for multiple increments of the ARTEMIS cycle (the numbers in circles denote the cycle increment)**

The results shown in Figure 78 highlight the second novelty of the framework by showing the trends of powertrain architecture selection given the travel range and trade-offs from two cost functions. The use of this toolbox lends itself naturally to identifying the transitions between powertrain topologies. Practitioners intending to use this toolbox will be able to generate such comparisons by defining their own cost function(s), along with the relevant vehicle parameters, powertrain components, and drivecycle.

## 7.2 Case Study 2: Powertrain Cost vs Well-to-Wheel $CO_2$

In this case study, the trade-offs between powertrain cost and well-to-wheel $CO_2$ are investigated, using the same powertrain topologies shown in Table 19. The definition and justifications of these two cost functions were carried out in Section 2.3.

The optimisation parameters for this case study are shown in Table 22. Based on these parameters, the multi-objective optimisation produced Pareto fronts as shown in Figure 79. The results shown in Figure 79 are for a single increment of the ARTEMIS cycle.

**Table 22: Decision variables (*X*) and constraints (*G*)**

| Term | Definition | Units |
|---|---|---|
| $\phi_1(X)$ | Estimated powertrain cost | USD $ |
| $\phi_2(X)$ | well-to-wheel $CO_2$ | kg |
| $X_1$ | 1 ≤ Energy Converter 1 ≤ 100 | - |
| $X_2$ | 1 ≤ Energy Storage 1 ≤ 100 | - |
| $X_3$ | 1≤ Energy Converter 2 ≤ 100 | - |
| $X_4$ | 1 ≤ Energy Storage 2 ≤ 100 | - |
| $X_5$ | 1 ≤ Powertrain Variant ≤ 4 | - |
| $G_1$ | 1000 ≤ total vehicle mass ≤ 1600 | kg |
| $G_2$ | Drivecycle speed constraints | m/s |

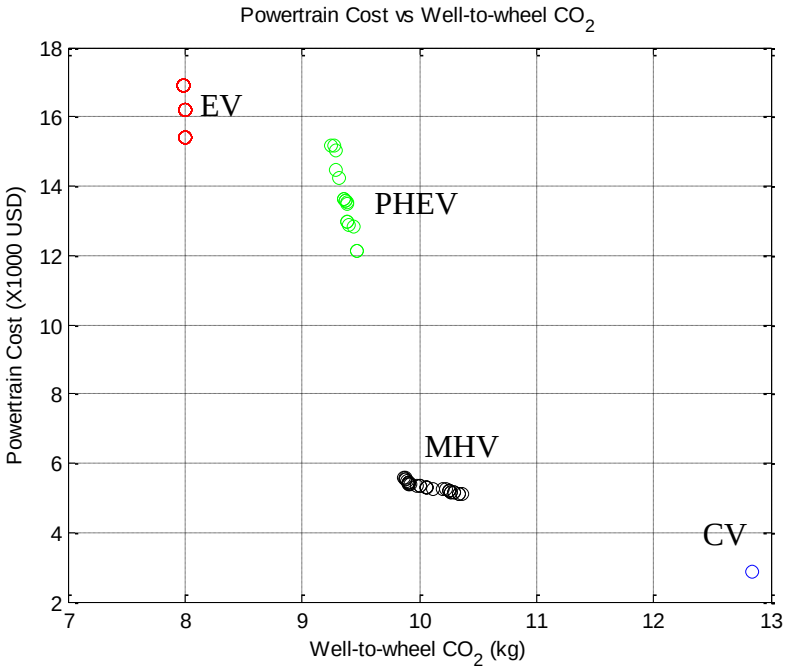


**Figure 79: Pareto front for single increment of the ARTEMIS drivecycle**

Between the powertrain topologies considered in this case study, the EV arguably has the highest powertrain cost relative to its autonomy range. Therefore, although it obtained the lowest well-to-wheel $CO_2$ emissions, it was at the expense of higher powertrain costs. Conversely, the CV produced the highest emissions but has the lowest powertrain costs. It is also observed that the CV does not have a Pareto front. Based on the Willans ICE model used in this research, a more expensive ICE will result in a larger displacement, and hence produce more emissions. Therefore, there is no trade-off as such when optimising the CV for those two cost functions, resulting in only one solution point instead of a Pareto front.

The Pareto fronts for each powertrain in Figure 79 is shown in Figure 80.

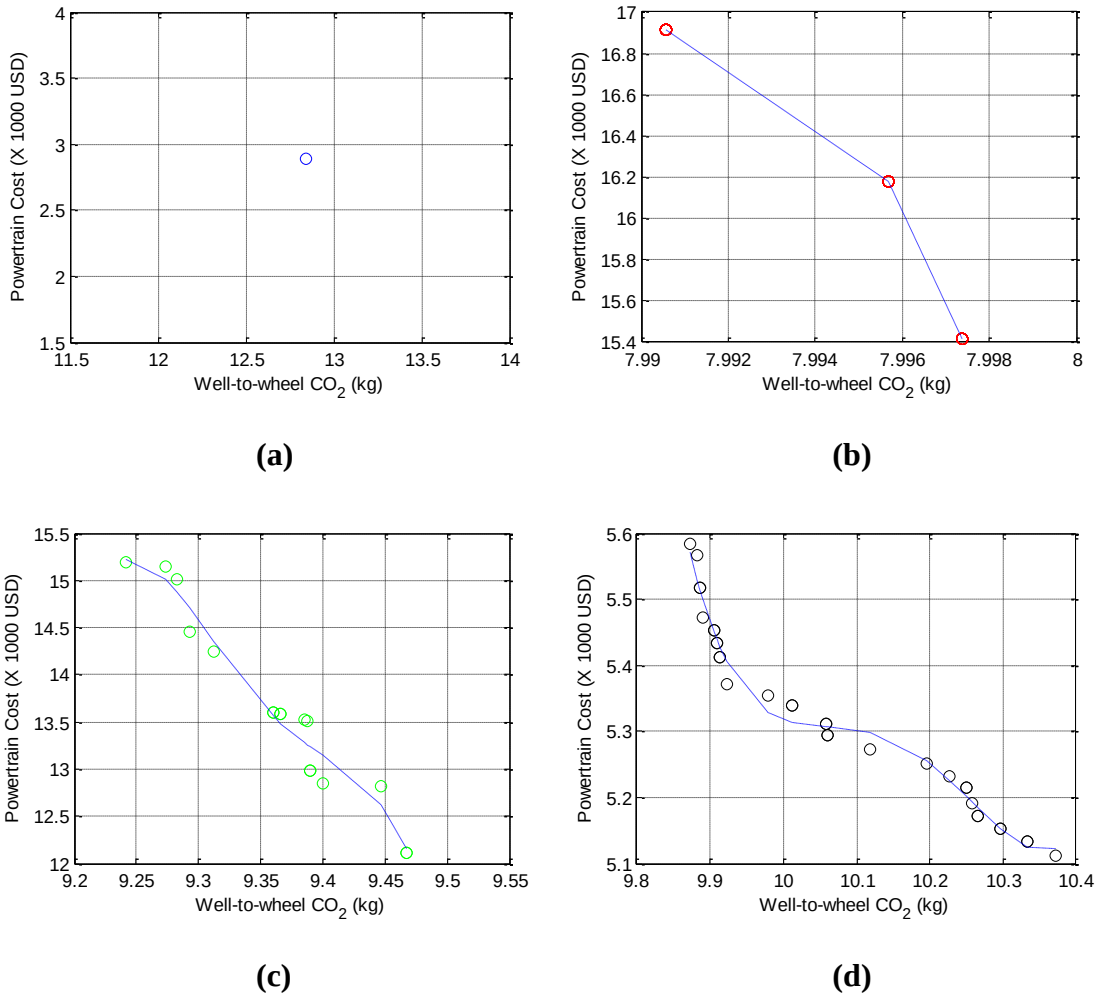


**Figure 80: Pareto fronts for individual powertrain topologies: (a) CV; (b) EV; (c) PHEV; and (d) MHV**

In particular, the result from Figure 80(b) relates back to the trends seen in Section 5.4 for sensitivity of the optimised battery size towards different cost functions. An EV

powertrain with a smaller battery (and thus lower powertrain cost) will produce more well-to-wheel $CO_2$ for a single increment of the ARTEMIS because the higher power losses within the battery (from higher current rates) than compared to a larger battery. In contrast, an EV with a larger battery (and thus more expensive), will produce lower well-to-wheel $CO_2$ emissions for a single increment of the ARTEMIS cycle, which supports the Pareto front seen in Figure 80(b).

Additionally, it is observed that there is a bigger spread of solution points on the Pareto fronts for the hybrid powertrains (both the PHEV and MHV). This is inherent from the larger solution space offered by the hybrid powertrains, due to the greater permutation of component size combinations gained from having more energy converters and storages when compared to the single-source powertrains (CV and EV).

By combining several increments of the ARTEMIS cycle, a 3-dimentional Pareto plot is created, as shown in Figure 81. It is observed that in the first two increments of the cycle, all four powertrain topologies are present on the Pareto front. However, the PHEV powertrain was eliminated from the third increment of the cycle onwards. The reason for this is that to achieve a higher autonomy range, the PHEV has to either have a larger battery, where it approaches the cost of the EV powertrain, or a larger fuel tank, where it approaches the emissions of the MHV (because of its comparatively higher mass coupled with lower efficiency when running in charge-sustaining mode).

Therefore, the region on the Pareto front that was once populated by the PHEV is now overlapped by the EV and the MHV, thus eliminating the need for a PHEV altogether. Although this may seem counter-intuitive, it should be stressed that the emission metric used in this case study is well-to-wheel $CO_2$; it is envisaged that the results would favour a PHEV over an MHV if it were tank-to-wheel $CO_2$, such as indicated in Figure 75.

After four increments of the cycle, the EV powertrain then gets eliminated as well because all of its possible solutions points would exceed the vehicle mass constraints of 1600kg in order to achieve the autonomy range on a single charge. This leaves the MHV and CV powertrains on the Pareto front for the fifth and sixth increments of the cycle.

The creation of a 3-dimentional Pareto plot such as Figure 81 is a natural output of the proposed toolbox. If the same results were to be replicated using the existing optimisation methods seen in the literature, it is envisaged that it would take significantly longer because each powertrain topology would have to be optimised separately to create the individual Pareto fronts. Additionally, some of the optimisation routines would be computationally wasteful because the particular powertrain topology may no longer be cost-effective for the levels of $CO_2$ produced, such as the PHEV in this case study, which was eliminated from the third increment of the ARTEMIS cycle.

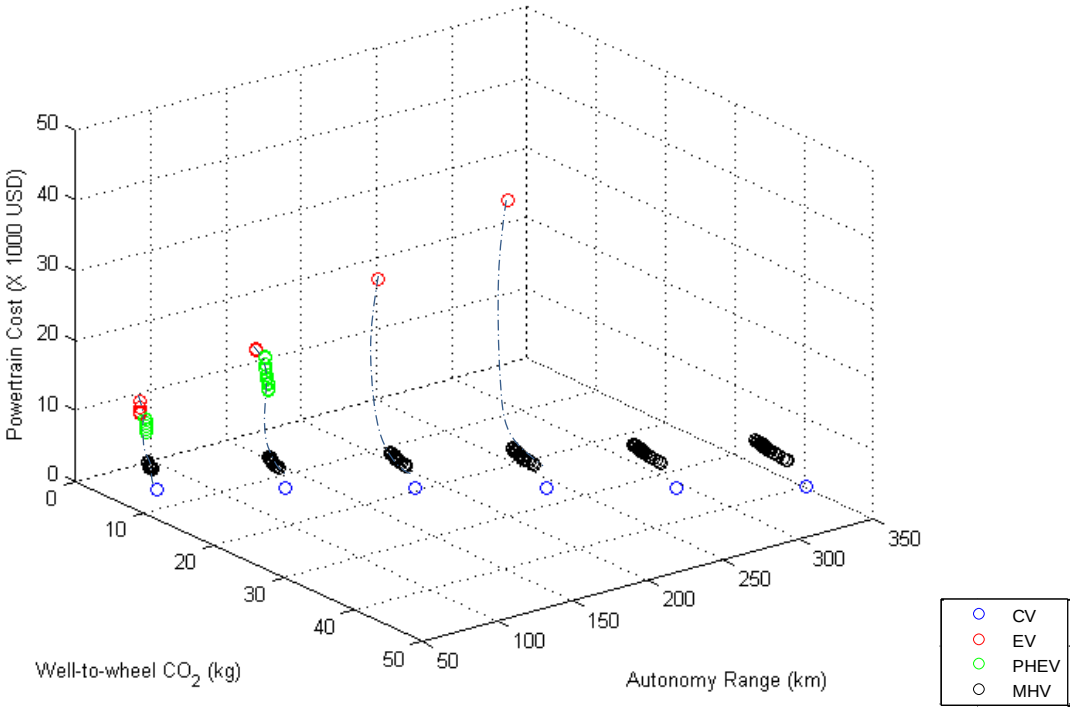


**Figure 81: Combination of Pareto fronts for all increments of the ARTEMIS cycle**

Additionally, with the increase in autonomy range, there is a divergence observed between the powertrain architectures, particularly between EV and MHV. The cost of the EV is highly sensitive to its range, with an increment of approximately $171 per kilometre of autonomy. However, the cost increment of the MHV and CV remain relatively constant, as the cost of extra fossil fuel to cover additional autonomy is insignificant. The reason for the EV's high sensitivity is due to the battery costs, and this relates back Equation (3-44) on page 54. For the PHEV, a mixture of this effect can be seen when comparing its spread of powertrain cost between the first and second increment of the ARTEMIS cycle.

## 7.3 Implementation in the FUTURE Vehicle Project

The FUTURE Vehicle project is an ongoing collaboration between six universities from the UK with the aim of improving the fundamental understandings of key powertrain components that are used in low carbon vehicles. This project began in 2011, and is being funded by the Engineering and Physical Sciences Research Council (EPSRC) [170]. The project contains six work packages that are running in parallel, with one work package allocated to each university. The following powertrain components are being investigated by this project:

- Lithium-ion batteries (Imperial College London)
- Ultracapacitors (Imperial College London)

- EMs (University of Oxford)
- Power electronics (University of Sheffield)
- Fuel cells (Loughborough University)

The role of Cranfield University is on integrating the reduced-order models of these powertrain components, and developing control strategies that aim to minimise their degradation. To that end, the proposed toolbox is being utilised to accommodate these powertrains components. The powertrain topologies that result from the inclusion of these components are shown in Appendix B.

An area that is currently being investigated in this project is the multi-objective optimisation of the battery-ultracapacitor EV powertrain. In this investigation, the battery model includes a degradation mechanism, where battery gradually loses its capacity when the following happens:

- Change in electric current direction (from charge to discharge and vice-versa)
- Magnitude of the current draw imposed on the battery.

The role of the ultracapacitor is to minimise these effects on the battery. To achieve this, the high transients in charge and discharge power demands is taken up by the ultracapacitors, thus "smoothening" the current load on the battery. Compared to the battery, the ultracapacitor is assumed to have negligible degradation.

Nevertheless, ultracapacitors are also an added cost to implement into an EV powertrain. However, supplementing the battery pack with ultracapacitors will also allow for downsizing the pack, and thus achieve a net weight reduction. This potentially leads to lower electricity consumption and hence lower well-to-wheel $CO_2$ emissions.

Therefore, a multi-objective optimisation study is being carried out to find the trade-offs between the size of the battery and the ultracapacitor with respect to powertrain costs and emissions.

## 7.4 Chapter Conclusions

This chapter highlighted the second novelty of this research, which is on multi-objective optimisation of powertrain topologies with component sizing. The case studies put forth in this chapter was made possible using the proposed toolbox in this research.

Three cost functions were then evaluated over two case studies to identify their trade-offs with respect to the powertrain topologies and mass constraints. The cost functions were well-to-wheel $CO_2$, tank-to-wheel $CO_2$ and estimated powertrain costs. These cost functions were chosen based on their recurring use in the literature for powertrain analysis.

It is noteworthy that the PHEV powertrain was eliminated from the third increment of the cycle onwards. The reason for this is that to achieve a higher autonomy range, the PHEV has to either have a larger battery, where it approaches the cost of the EV powertrain, or a larger fuel tank, where it approaches the emissions of the MHV (because of its comparatively higher mass coupled with lower efficiency when running in charge-sustaining mode). Additionally, a divergence was observed between the powertrain as the autonomy range increased. This was driven by the cost of the powertrain, with the EV exhibiting the highest cost sensitivity per kilometre of additional autonomy range.

The proposed methodology, supported by these findings, opens a way for practitioners to quantify the benefits and trade-offs from each type of powertrain architecture in a multi-objective optimisation environment.

# 8 CONCLUSIONS

Through the literature review, it was identified that different powertrain topologies have a variety of trade-offs in their performances with regards to emissions, autonomy range, and costs. However, collating data from literature for analysing such trade-offs produced findings that were discontinuous, thus making it difficult for drawing conclusions when comparing multiple types of powertrain topologies. This led to the research hypothesis; is it possible to determine the most appropriate powertrain architecture for a given vehicle type and usage profile, based on a unified optimisation routine?

To prove this hypothesis, it was determined that a methodology that combines an optimisation algorithm with a multi-architecture powertrain simulation environment was required. This then led to the two novel areas of research: creating a methodology to simultaneously select a powertrain topology and optimise its component sizes for a given cost function, and utilising multi-objective optimisation for identifying trade-offs between cost functions by way of powertrain topology selection.

To support this research, powertrain topologies for the following types of vehicles were created: Conventional Vehicle (CV), Electric Vehicle (EV), Series Plug-in Hybrid Electric Vehicle (PHEV), and Flywheel-based Mechanical Hybrid Vehicle (MHV). This list was narrowed down based on the availability and quality of data gathered from literature and from work carried out by Cranfield University with partners and funded projects. Whilst the powertrain component performances were verified against data from real vehicles, several assumptions were made with regards to their scalability for peak power. Additionally, the scaling of financial costs and component mass was based on linear functions. Nevertheless, this level of fidelity was deemed sufficient for the purpose of demonstrating the functionality of the proposed methodology.

The drivecycles that were used to simulate the powertrains were the NEDC, ARTEMIS cycle, and Cranfield cycle. The first two cycles were selected based on their recurring use in literature, whereas the last cycle was developed at Cranfield University though a series of real-world tests using a Smart ED electric vehicle.

Lastly, a sensitivity analysis was carried out to identify the severity of the uncertainties of several parameters in the model. Based on the EV powertrain that was analysed, it was found that changes in glider mass had the most pronounced effect towards changes in energy consumption. The trends from the sensitivity analysis were noted and were subsequently investigated in the optimisation study. However, based on the investigations carried out, it was revealed that whilst the change in parameters affected the sizing of the powertrain components, it did not affect the selection of the powertrain topology.

It was identified that there are two methods for carrying out vehicle powertrain modelling: forward-facing and backward-facing models. Each method has its advantages and disadvantages. For the purpose of iterative optimisation routines, coupled with the knowledge of the vehicle speed profile apriori, it was deemed that the backward-facing model was the most suitable option for the purposes of this research, with its comparatively faster simulation times. However, given the relatively larger time step of the backward-facing approach, the proposed toolbox is more suited to obtain a first-hand approximation for the type of powertrain topology that is most appropriate for a given vehicle type and duty cycle. Hence, the toolbox is suitable for powertrain analysis, rather than specific powertrain design, and it can be used to predict measures such as fuel consumption and emissions; however, it cannot be used to study details that require smaller time-steps, such as vibrations and harshness. Additionally, backward-facing models do not adhere to physical causality which is important when developing control system algorithms; however this is not part of the aims of this research.

The switching between powertrain topologies within the Modular Powertrain Structure (MPS) was made possible because of the modular approach to encapsulating the various powertrain components. The powertrain components within a given topology were classified as energy converter, energy storage, and power transformers. This classification provided modularity in the implementation of powertrain topologies in the toolbox. Modularity is important because this toolbox will need to offer the flexibility for completely defining the layout of the powertrain configuration.

A methodology was created to facilitate the ability to simultaneously optimise both the powertrain topology and components sizes within the toolbox. The MPS encapsulates this methodology, and when combined with a Genetic Algorithm, forms the optimisation framework within the proposed toolbox. This framework underscores the first novelty of this research. The NSGA-II algorithm was also included into the framework to support multi-objective optimisations, and supports the second novelty of this research.

Using the proposed toolbox, investigations have identified the transition points between powertrain topologies based on the optimisation cost functions and a given set of constraints. In Chapter 6, the results showed the trends in the selection of powertrain topologies when optimising purely for well-to-wheel $CO_2$. For the initial increments of the drivecycles, the EV powertrain was chosen because it emitted the lowest well-to-wheel $CO_2$ when compared to the other topologies. However, when the EV exceeded the mass constraints for increased autonomy range, the transition into a different powertrain was dependant on the power and energy requirements of the individual drivecycles. For higher autonomy ranges, the PHEV was selected for transient cycles such as the ARTEMIS and Cranfield cycles, whereas the CV was selected for the NEDC instead.

For a given powertrain architecture, it was interesting to note that that the lightest configuration may not necessarily yield the lowest well-to-wheel $CO_2$ emissions. In the case of the EV, a smaller EM, though lighter, would not be able to capture all of the deceleration events, thus sacrificing energy that could have been recovered via regenerative braking. Therefore, one of two outcomes were observed from the optimiser when sizing powertrain components: sizing the component for lowest overall powertrain mass, or sizing the component for maximising energy recovery via regenerative braking. This decision was observed to vary according to the drivecycle; for the Cranfield cycle, the EM was sized to maximise on regenerative braking capability (resulting in a heavier EM with higher power rating), whereas for the ARTEMIS cycle, the EM was sized just enough to meet the propulsion power demands (lighter but sacrificing on recuperated braking energy). This was attributed to the acceleration levels seen in the drivecycles, with the higher acceleration levels in the ARTEMIS favouring a lighter vehicle than one which is heavier but with greater regenerative braking capabilities.

To probe the optimisation results from the toolbox further, several sensitivity analyses were carried out, including varying the amount of regenerative braking, glider mass, vehicle mass constraints, and electricity grid $CO_2$ emissions. For the ARTEMIS cycle, whilst the increase in the regenerative power of the EM resulted in reduced emissions, it was interesting to note that it had no effect on the selection of the powertrain topologies. Other constraints, such as mass limits and energy density of the storage elements, were observed to be more dominant in the selection of the powertrain topology. The transition from the EV to the PHEV powertrain still occurred when the mass constraints of the vehicle was exceeded. Varying the vehicle mass constraints, however, did have an effect on the switching point between powertrain depending on the autonomy range.

For the effects in road inclination, the main difference observed was the selection of PHEV instead of the CV for higher autonomy ranges on the NEDC. This was attributed to the ability of the PHEV to utilise regenerative braking during hill descents. A test case was also carried out to study the effects of variation in $CO_2$ emissions from the electricity grid mix. In this test case, France was used an example because of its substantially lower $CO_2$ emission per kWh when compared to the UK. As a result, the well-to-wheel $CO_2$ outputs were also observed to be much lower.

In Chapter 7, the use of multi-objective optimisation was included as part of the powertrain topology selection and components sizing routine. Whilst the optimisations were limited to the ARTEMIS cycle, several cost functions were evaluated and the trade-offs in these cost functions were evident from the Pareto fronts of the various powertrain topologies. The creation of a 3-dimentional Pareto plot that showed the various solution points from different powertrain topologies is inherent from the ability of the toolbox to concurrently evaluate different topologies during the optimisation. Therefore, is it envisaged that practitioners using this toolbox would be able to perform

multi-objective powertrain topology optimisations more directly and quickly than using conventional methods.

These aims of this research were addressed by creating a toolbox that provided the ability to simultaneously optimise both the powertrain topologies and components sizes, given a set of constraints and cost function(s). The ability to compare multiple types of powertrain is useful because of the significant number of advanced powertrain topologies that are available.

Using the novel methodology proposed in this research, investigations have identified the transition points between powertrain topologies, given the drivecycle, desired autonomy range, and associated cost function(s). If the results from these simulations were to be replicated using conventional methods, it is envisaged to take significantly longer to produce, because each powertrain would have to be individually optimised. Additionally, some of the optimisation would be computationally wasteful because the particular powertrain topology may no longer be suitable for the design targets, although this may not be realised until the optimisation routine is completed.

It is important to reiterate that this methodology is used to obtain a first-hand approximation for the type of powertrain that is most likely suitable or a given vehicle type and duty cycle. Thus, this research aims to produce a tool suitable for powertrain analysis, rather than specific powertrain design. It can be used to predict measures such as fuel consumption and emissions; however, it cannot be used to study details that require smaller time-steps, such as vibrations and harshness.

Although this research covered four types of powertrain topologies, the flexibility of the MPS will enable additional types of energy converters and energy storages to be included, thus creating further permutations of powertrain topologies. In conclusion, the hypothesis of this research has been addressed; it is indeed possible, by way of a unified optimiser and a modular powertrain framework, to determine the most appropriate powertrain architecture for a given vehicle type and usage profile. Practitioners would benefit from a flexible toolbox that facilitates simultaneous optimisation of both powertrain topology and component sizing, and the proposed toolbox could ultimately be used to establish standards within the automotive modelling community.

## 8.1 Future Work

There were several assumptions made with regards to the creation of the powertrain components, especially in the implementation of scalability. Future work may wish to investigate the use of discreet component selection for different peak power requirements. For example, instead of using just one EM model to scale across a large range, there can be several discrete EM models to choose from during the optimisation, such that each EM now caters for a smaller window of peak power scaling.

The results of the optimised powertrain component sizes are based on drivability measures that are defined by the drivecycle. During the optimisation, the powertrain selection and sizing are constrained to the power and energy demands of that particular drivecycle. However, vehicle manufacturers also use other measures such as minimum 0 – 100 km/h times and overtaking manoeuvre times to optimise the size of their powertrain components. These attributes could also be included into the toolbox as part of future work by supplementing the drivecycle to include such power demands.

The battery model was parameterised such that its internal resistance value was optimised to minimise the RMS of the cumulative SOC error between the simulated model and the measure data. Unfortunately, variations in the resistance under charge and discharge conditions, as well as in different thermal operating conditions, were inherently averaged using this approach. Future work could investigate this area by parameterising the model from data obtained using a battery test rig in a controlled test environment.

For the hybrid powertrains, a rule-based supervisory controller was used. However, an optimal trajectory for the split in power between the two power sources could be created as part of future work and included into the optimisation. This can potentially be achieved using two optimisation loops. The larger “outer” optimisation loop performs the powertrain topology selection and sizing. For each topology selected, an “inner” loop then calculates the ideal power split amongst the hybrid power systems.

Finally, this research is an early part of a long term vision for developing a toolbox that utilises artificial intelligence to create the optimal powertrain topology from a mix of powertrain components. At present, powertrain topologies have been pre-defined as variants, as seen in Chapter 4. The ability to automatically define the powertrain topology based on a selection of powertrain components will be very valuable to manufacturers as part of their design process.

# APPENDICES

## Appendix A M-file Codes for Optimiser

The following subsections in this Appendix lists key MATLAB m-files used in the proposed toolbox to carry out simultaneous optimisation of the powertrain topology and component sizing. Section A.1 is the shows the interface script of this toolbox, where all the key parameters of the optimisation, such as drivecycle type, cost function, and mass and cost limits of the vehicle are specified. Section A.2 then lists the codes for the Initial Population Generator, which was discussed in page 71, followed by sub-section A.2.1 which shows a sample of the output from this code. Sections A.3 and A.4 then follow by showing the codes for the Custom Rounding function and Custom Mutation function, which were discussed in pages 78 and 79 respectively.

### A.1 Initialising the Optimisation Run

```
%% Drivecycle to Use
% 0 - Blank
% 1 - NEDC
% 2 - Cranfield
% 3 - Artemis
% 4 - Constant Speed where type is speed value

dcType = 3;
dcIncrement = 1;
dcLowerLimit = 1;
dcUpperLimit = 6;

%% Minimisation Function
% 1 - Well-to-Wheel CO2
% 2 - Tank-to-Wheel CO2
% 3 - Mass
% 4 - WtW CO2 and Mass (Multi-objective)
% 5 - WtW CO2 and Cost (Multi-objective)
% 6 - Mass of Battery vs Mass of UCap (Multi-objective)

costFunction = 6;

%% Simulation Limits

massLimit = 1600;
costLimit = 1e8;

%% Powertrain Selection
% 1 - Conventional Powertrain
% 2 - EV
% 3 - Series PHEV
% 4 - Fuel Cell + Ultracap
% 5 - Parallel Flywheel + CVT
% 6 - Battery + Ultracap
% 7 - EV (with SOH)
% 8 - Battery (with SOH) + Ultracap
```

```
powertrainSelection = [8];  %Please ensure selection array is in
ascending order!
powertrainSelection = sort(powertrainSelection);

%% Launch Simulation

[resultArray] =
runDCRange(dcType,dcIncrement,dcLowerLimit,dcUpperLimit,massLimit,cost
Limit,costFunction,powertrainSelection);

save('Result_Final');
```

## A.2 MATLAB code for Initial Population Generator

The following m-file codes support the discussion in Section 4.2.1.

```
function IP = getIniPop(LB,UB,popDist,type)

% Type
% 1 - Random
% 2 - Uniform

nP = length(UB);

if type == 1
    popSize = popDist;
    IP = repmat(LB,popSize,1) + rand(popSize,nP).*repmat((UB-
LB),popSize,1);
end

if type == 2
    popSize = 1;
    for i = 1:nP;
        popSize=popSize*popDist(i);
    end

    axesValues = zeros(max(popDist),nP);

    for i = 1:nP
        axesValues(1:popDist(i),i) =
linspace(LB(i),UB(i),popDist(i))';
    end

    IP = zeros(popSize,nP);

    for i = 0:popSize-1
        idx = i;

        for j = 1:nP
            idxAxes = mod(idx,popDist(j))+1;
            idx = floor(idx/popDist(j));
            IP(i+1,j) = axesValues(idxAxes,j);
        end
```

```
    end
end
% keyboard;
IP = roundMe(IP,[1 1 1 1 1]); % Force individual to be integer only
IP = conditionIndividual(IP); % Condition individual based on
powertrain type
end
```

### A.2.1 Results for Initial Population Generator

The following list is the output from the Initial Population Generator, as discussed in Section 4.2.2.

**Table A1: The list of individuals created by the Initial Population Generator**

| Individual No. | EM Power (kW) | Battery Size (kWh) | | Individual No. | EM Power (kW) | Battery Size (kWh) |
|---|---|---|---|---|---|---|
| 1 | 40 | 10 | | 26 | 40 | 88 |
| 2 | 55 | 10 | | 27 | 55 | 88 |
| 3 | 70 | 10 | | 28 | 70 | 88 |
| 4 | 85 | 10 | | 29 | 85 | 88 |
| 5 | 100 | 10 | | 30 | 100 | 88 |
| 6 | 40 | 26 | | 31 | 40 | 103 |
| 7 | 55 | 26 | | 32 | 55 | 103 |
| 8 | 70 | 26 | | 33 | 70 | 103 |
| 9 | 85 | 26 | | 34 | 85 | 103 |
| 10 | 100 | 26 | | 35 | 100 | 103 |
| 11 | 40 | 41 | | 36 | 40 | 119 |
| 12 | 55 | 41 | | 37 | 55 | 119 |
| 13 | 70 | 41 | | 38 | 70 | 119 |
| 14 | 85 | 41 | | 39 | 85 | 119 |
| 15 | 100 | 41 | | 40 | 100 | 119 |
| 16 | 40 | 57 | | 41 | 40 | 134 |
| 17 | 55 | 57 | | 42 | 55 | 134 |
| 18 | 70 | 57 | | 43 | 70 | 134 |
| 19 | 85 | 57 | | 44 | 85 | 134 |
| 20 | 100 | 57 | | 45 | 100 | 134 |
| 21 | 40 | 72 | | 46 | 40 | 150 |
| 22 | 55 | 72 | | 47 | 55 | 150 |
| 23 | 70 | 72 | | 48 | 70 | 150 |
| 24 | 85 | 72 | | 49 | 85 | 150 |
| 25 | 100 | 72 | | 50 | 100 | 150 |

## A.3 MATLAB code for Custom Rounding Functions

The following m-file codes support the discussion in Section 4.5.1

```
function rounded = roundMe(IP,roundReq)

try
    if isempty(IP)
        rounded = IP;
    else
        if length(IP(1,:)) == length(roundReq)
            rounded = zeros(size(IP));
            for i = 1:length(IP(:,1))
                for j = 1:length(roundReq)
                    rounded(i,j) =
roundReq(j)*(round(IP(i,j)*(1/roundReq(j))));
                end
            end
        else
            disp('Population rounding error - individual size and
rounding requirements mismatch')
            rounded = IP;
        end
    end
catch RoundError
    disp('Population rounding error - function aborted')
    rounded = IP;
end
end
```

## A.4 MATLAB code for Custom Mutation Function

The following m-file codes support the discussion in Section 4.5.2

```
function newIndividual =
findNearIndividual(individual,y,UB,LB,funHdl,multiObj,toPlot)
scaleVal = (UB-LB).*y;
LowB = individual-scaleVal;
UpB = individual+scaleVal;
LowB = max(LB,LowB);
UpB = min(UB,UpB);
res = inf;
count = 0;

while isinf(res)
    count = count + 1;
    newIndividual = getIniPop(LowB,UpB,1,1);
    if count == 10
        newIndividual = individual;
    end

    if multiObj == 0
        res = feval(funHdl,newIndividual);
    else
        resTemp = feval(funHdl,newIndividual);
        if isinf(resTemp(1)) %== 1e12
            res = inf;
        else
            if isinf(resTemp(2)) %== 1e12
                res = inf;
            else
                res = 1;
            end
        end
    end
end

if toPlot
    figure(20)
    plot(individual(1),individual(2),'.k')
    hold on;
    rectangle('Position',[LowB(1),LowB(2),UpB(1)-LowB(1),UpB(2)-
LowB(2)])
    scatter(newIndividual(1),newIndividual(2),res,'.r')
    xlim([LB(1) UB(1)]);
    ylim([LB(2) UB(2)]);
end

end
```

# Appendix B Other Possible Powertrains Topologies for Inclusion into the MPS

The following are examples of other powertrain topologies that can be included into the MPS. The topologies shown in Figure A1 and Figure A2 are being investigated as part of the FUTURE Vehicle project [170]. This appendix supports the discussions carried out in Section 4.1.1 and Section 7.3.

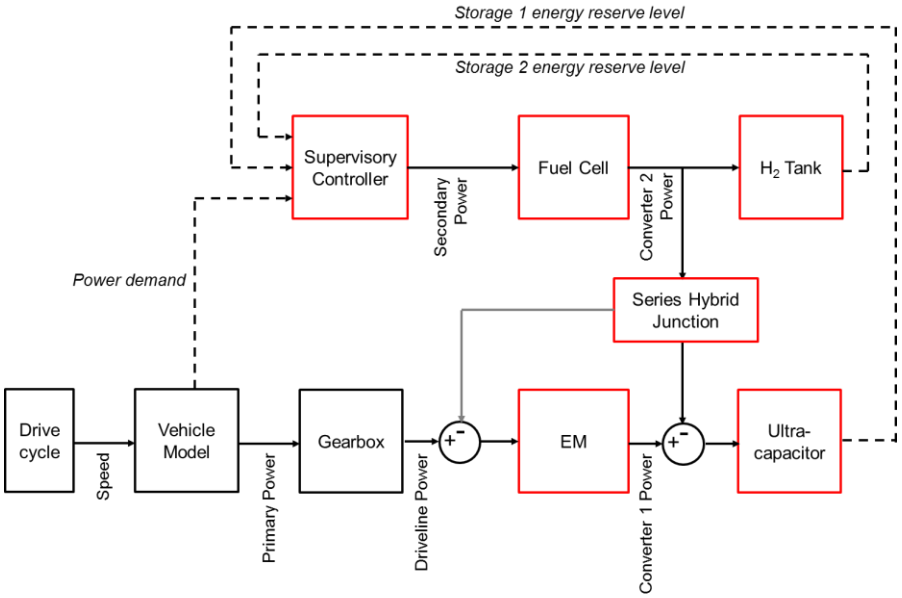


**Figure A1: Fuel Cell – Ultracapacitor Hybrid**

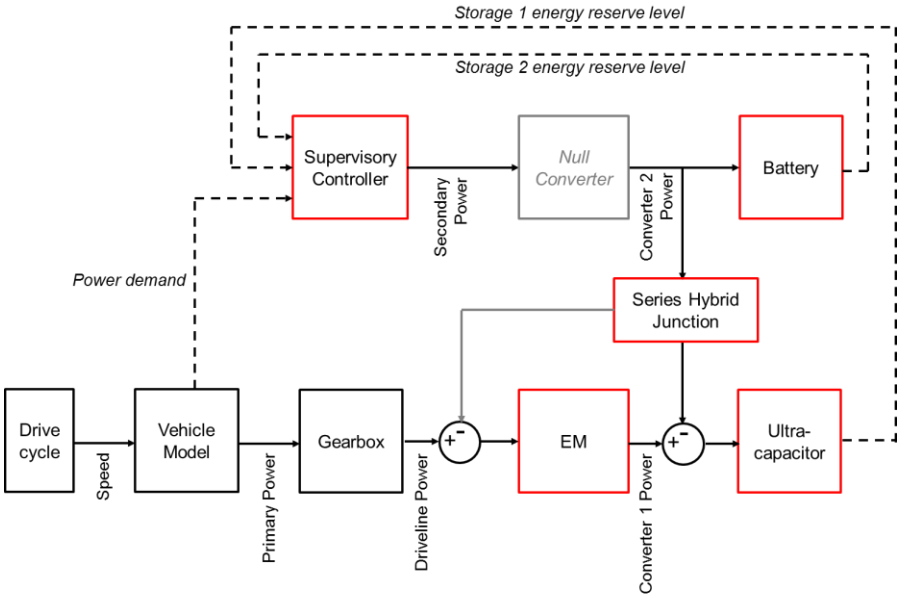


**Figure A2: Battery - Ultracapacitor Hybrid**

Figure A3 shows the Ford C-Max power-split hybrid powertrain incorporated into the MPS. This was made possible by encapsulating the powertrain components into the respective energy converters and energy converters. The high-level schematic of this powertrain is shown in Figure A4. This powertrain topology was created to support a technical presentation that was delivered at the Ford Technical Centre in Dearborn, USA by the author.

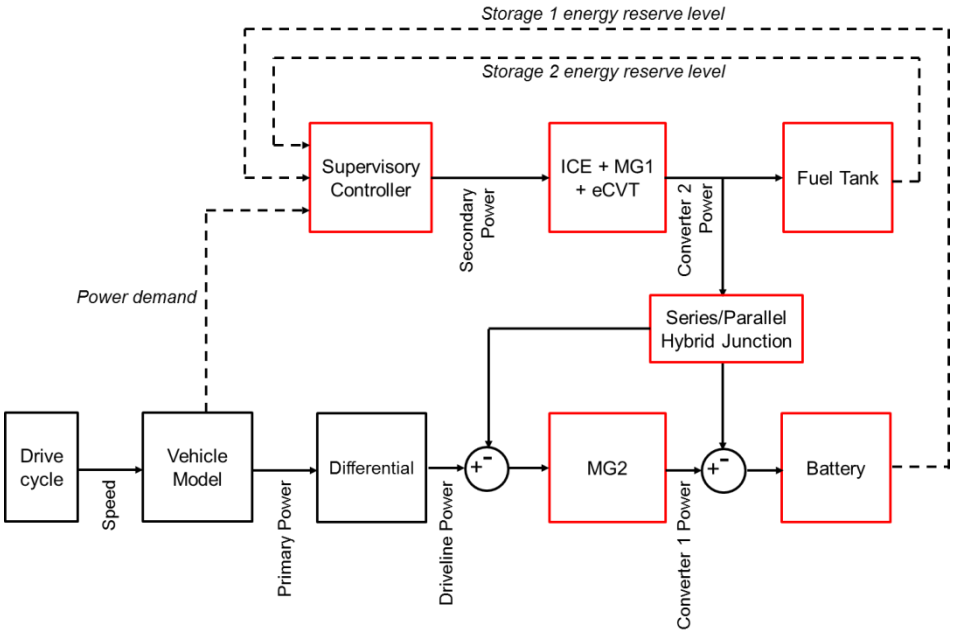


**Figure A3: The Ford C-Max power-split hybrid powertrain**

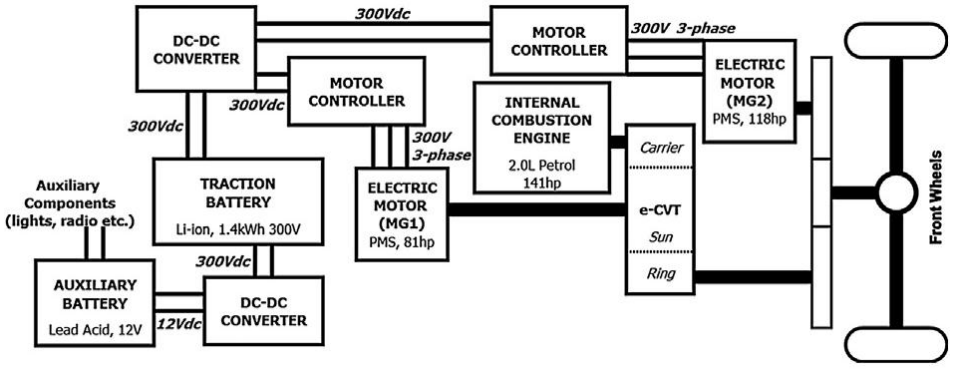


**Figure A4: High-level schematic of the Ford C-Max power-split powertrain** [171]

# Appendix C Vehicle Data

Table A2 contains data for the vehicle models referenced throughout this thesis. A majority of the data was sourced internally from work carried out for the following funded projects:

- Low Carbon Vehicle Technology Project (LCVTP) [40]
- Smart Move Electric Vehicle Trial conducted by Cenex [79]
- FUTURE Vehicle consortium (EPSRC grant number EP/I038586/1).

However, where possible, published references are provided for verification of these data. These are indicated in square brackets inside each applicable cell.

**Table A2: List of vehicle data**

| **Vehicle** | **Smart ED** | **Smart Fortwo (Petrol)** | **Jaguar Limo Green** | **Jaguar XJ (Petrol)** | **Nissan Leaf** |
|---|---|---|---|---|---|
| **Dry Mass (kg)** | 965 | 750 [172] | 2036 | 1755 [172] | 1525 [172] |
| **Frontal Area ($m^2$)** | 2.06 [173] | 2.06 [173] | 2.4 | 2.4 | 2.27 [172] |
| **Coeff of Aero Drag** | 0.35 [173] | 0.35 [173] | 0.29 [172] | 0.29 [172] | 0.29 [172] |
| **Battery Capacity (kWh)** | 16.5 [79] | - | 17.6 | - | 24 [172] |
| **Battery Power (kW)** | 30 [79] | - | 247 | - | 90 |
| **Driven Axle** | Rear | Rear | Rear | Rear | Front |
| **Tyre Rolling Radius** | 0.25 | 0.25 | 0.35 | 0.35 | 0.32 |
| **Coeff of Rolling Resistance (total)** | 0.006 | 0.006 | 0.008 | 0.008 | 0.007 |
| **EM Peak Power (kW)** | 55 (limited to 30) | - | 145 | - | 80 |
| **ICE Type** | - | 1.0L 3-cylinders [172] | 1.3L 3-cylinder [100] | 5.0L V8 [172] | - |
| **ICE Peak Power (kW)** | - | | 35 [100] | 283 [172] | - |

The tyre rolling radii were measured directly from the vehicles during the project. The coefficients of aerodynamic drag and rolling resistance for the Smart was derived from the coastdown curve provided by Millbrook, who also participated in the Smart Move Trial [79]. Similarly, the coefficients of aerodynamic drag and rolling resistance for the Jaguar Limo Green was derived from the coastdown curve provided by Ricardo, and the same values were assumed for the Jaguar XJ (petrol).

## C.1 Transmission Ratios

Table A3 shows the list of ratios used in the mechanical transmission for the CV and MHV topologies, based on the ZF 8-speed transmission from the Jaguar XJ saloon. Transmission data is soured from [174] and from work carried out for the LCVTP project. The reverse gear is not considered in this research, and is therefore excluded from this list. The gear ratio for the Smart Fortwo (petrol 1.0L model) is also shown in Table Table A4 [85].

For the EV and PHEV powertrain, where the EM is the primary mover, the gear ratio is fixed at 8.67, which is the same as that on the Smart ED vehicle.

**Table A3: Gear ratio for ZF 8-speed transmission**

| Gear No. | Ratio |
|---|---|
| 1 | 4.70 |
| 2 | 3.13 |
| 3 | 2.10 |
| 4 | 1.67 |
| 5 | 1.29 |
| 6 | 1.00 |
| 7 | 0.84 |
| 8 | 0.67 |

**Table A4: Gear ratio for Smart Fortwo (petrol) transmission**

| Gear No. | Ratio |
|---|---|
| 1 | 13.912 |
| 2 | 8.664 |
| 3 | 5.697 |
| 4 | 4.271 |
| 5 | 3.456 |

# Appendix D Full Implementation of MPS in Simulink

## D.1 Conventional Vehicle

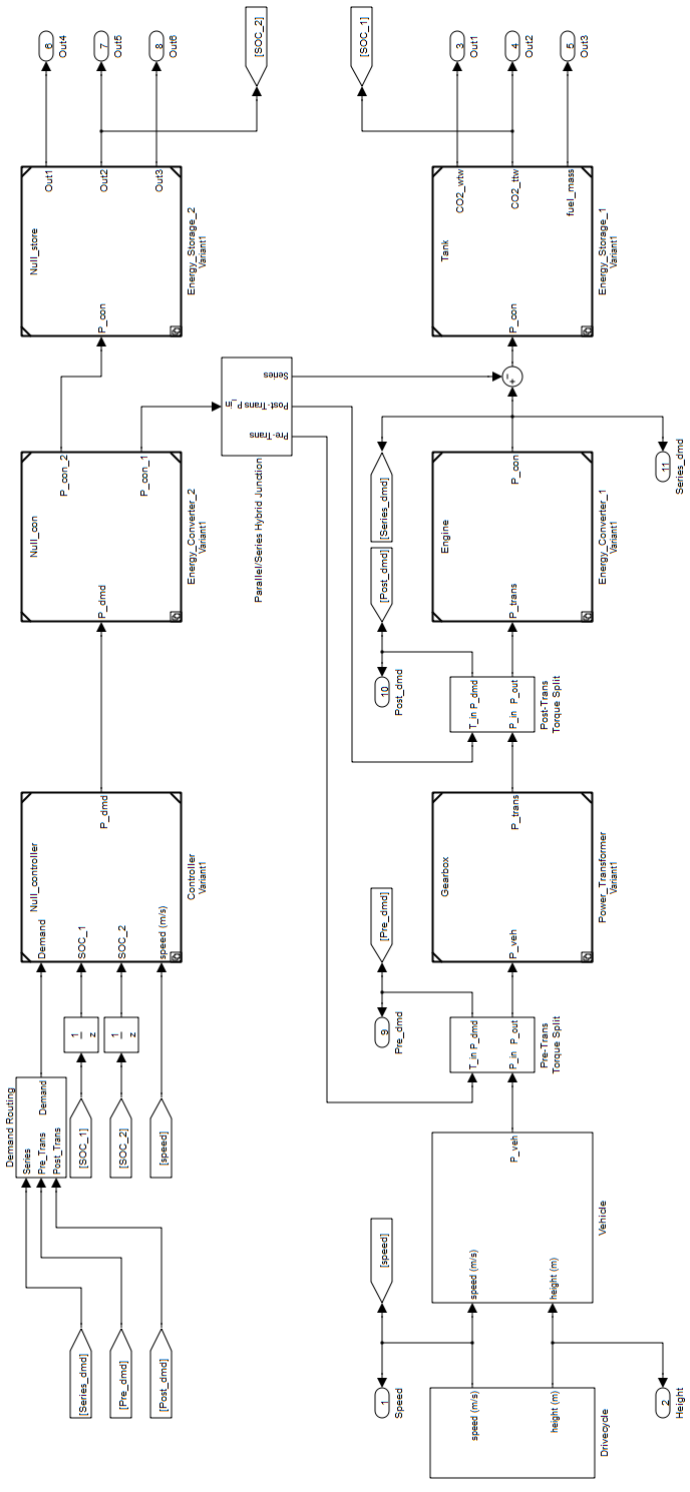

## D.2 Plugin Series Hybrid Electric Vehicle

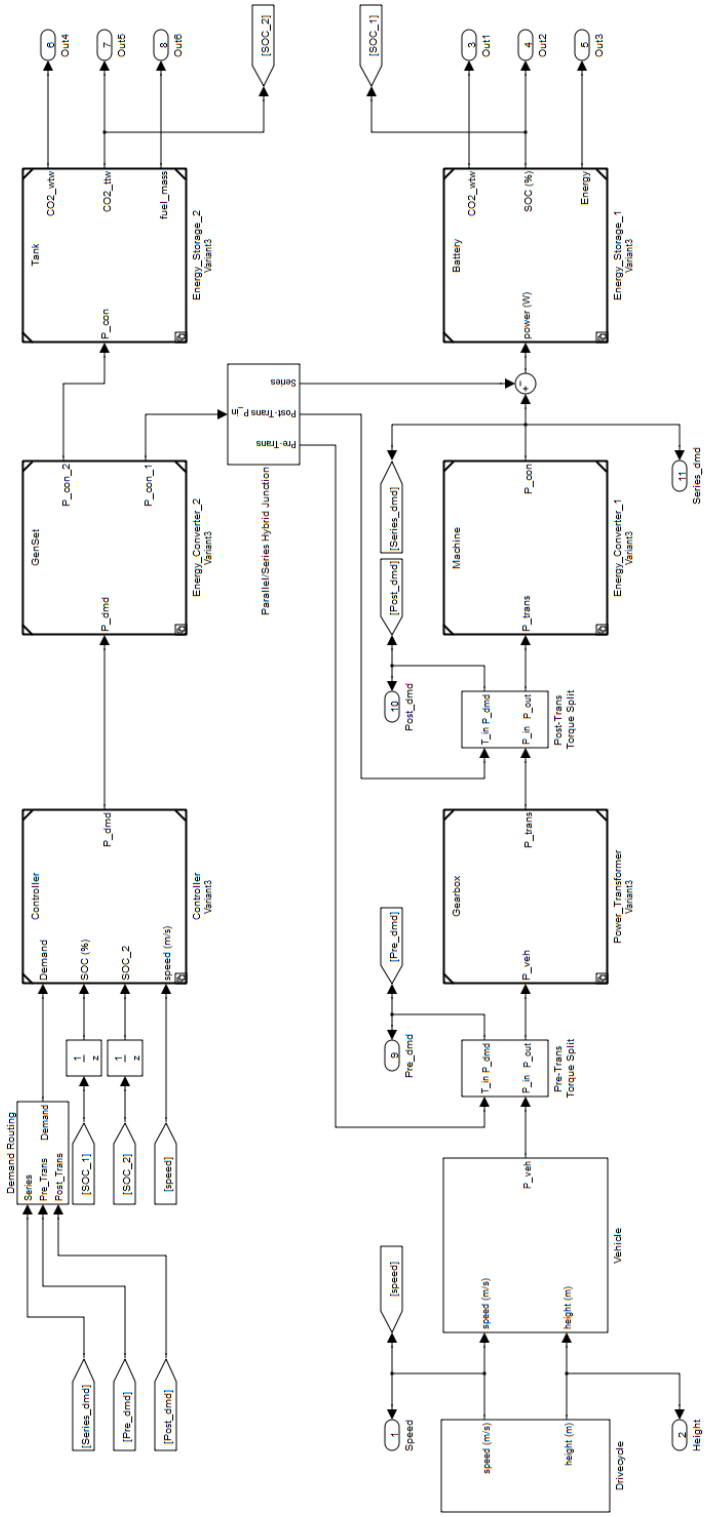

# Appendix E List Of Inputs and Outputs for Powertrain Topologies

This Appendix lists the Simulink models for the energy converters and energy storages considered in this thesis.

## E.1 Vehicle Model

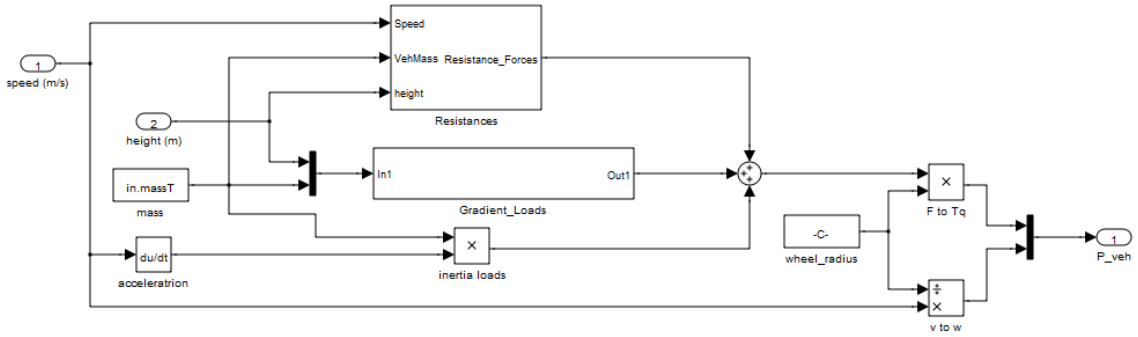


## E.2 Internal Combustion Engine

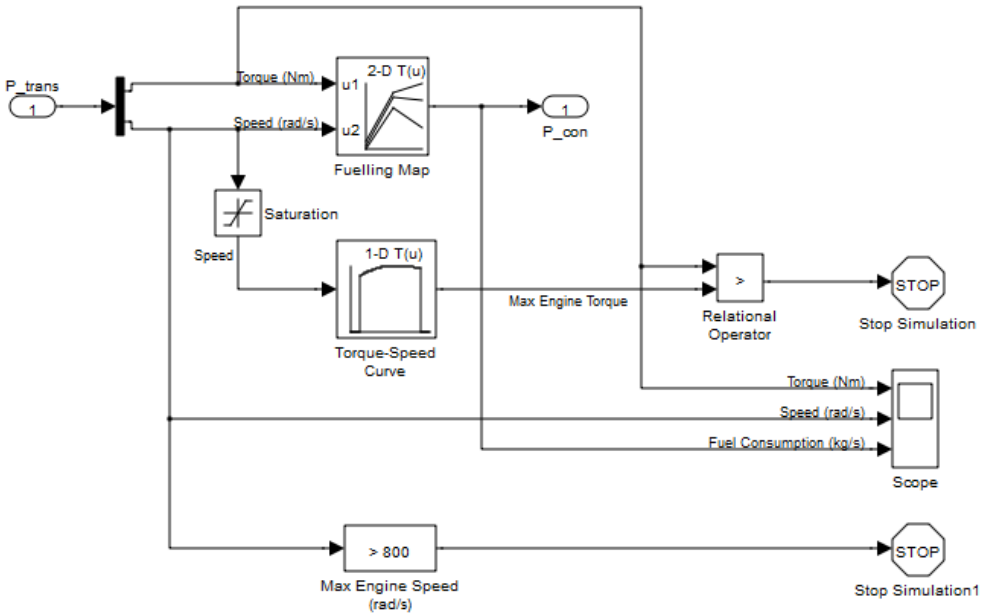

## E.3 Electrical Machine

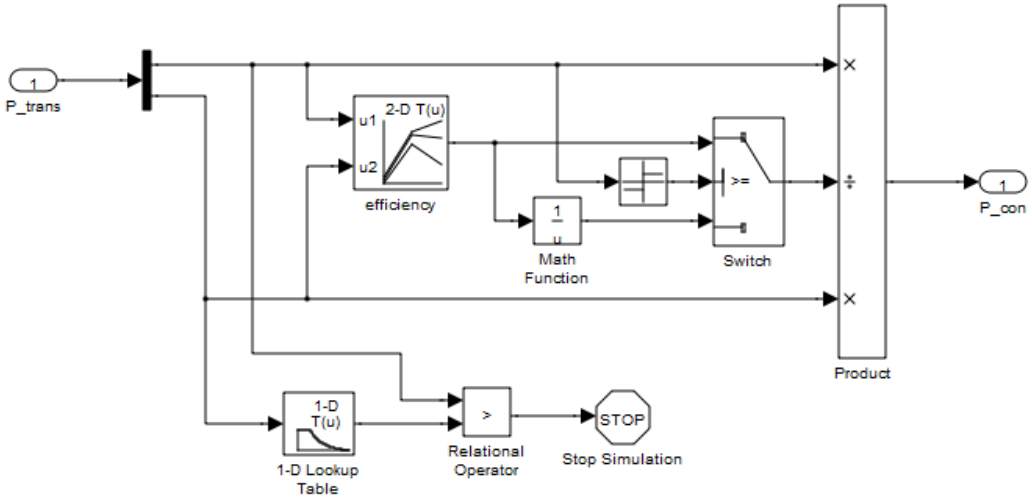


## E.4 Battery Model

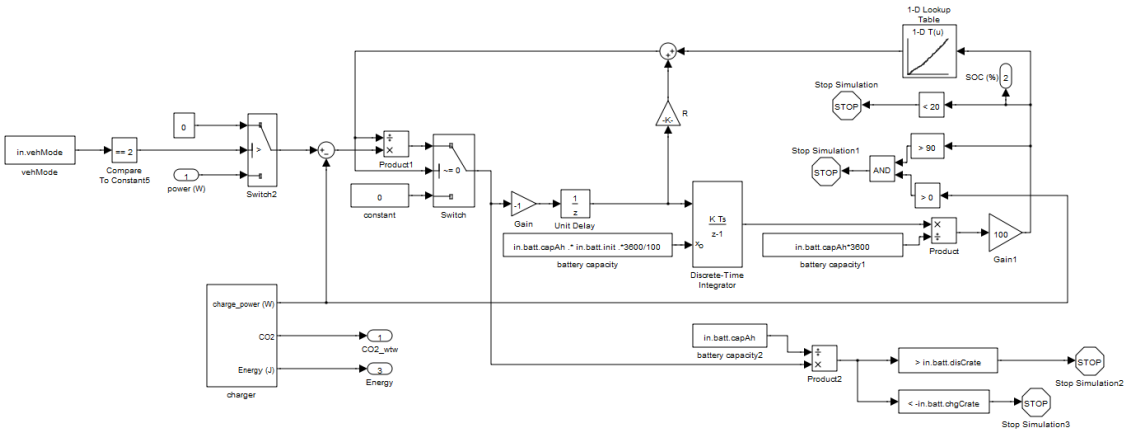


## E.5 Mechanical Transmission

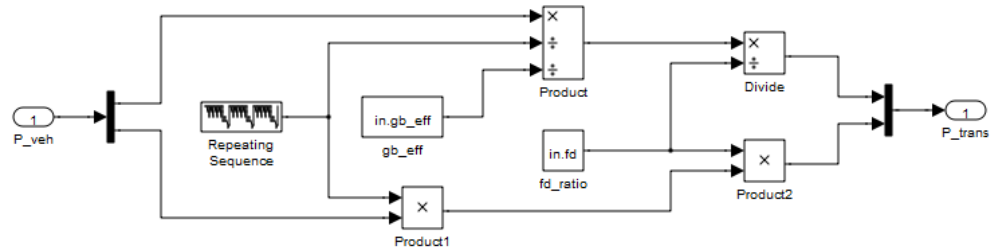

## E.6 Thermostatic Controller

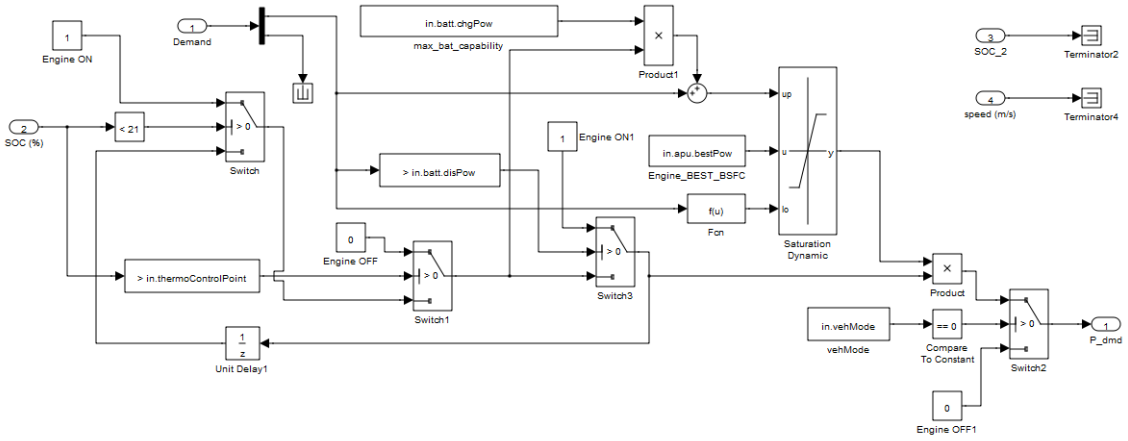


## E.7 Flywheel

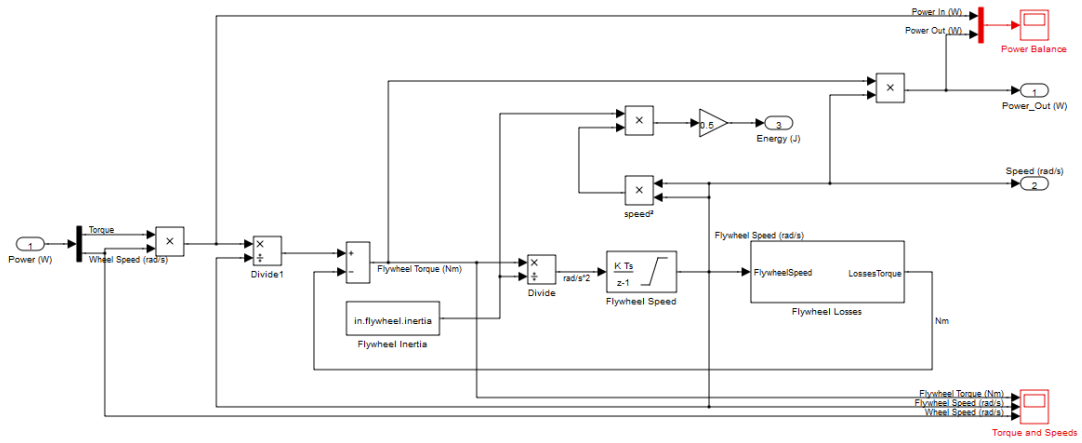

# Appendix F Scripts for Powertrain Topology Switching

The following script shows the interface between powertrain topology parameterisation and initialisation in MATLAB with the MPS in Simulink. It supports the discussion that was carried out in Section 4.1.1. Each topology initialises its respective components in MATLAB, and this information is then passed on to the "Variant subsystem" block in Simulink to create the desired topology for inclusion into the optimisation routine.

```
function [in simu] =
runModel(vehMass,massLimit,drivecycleType,drivecycleRepeat,fdRatio,con
Scale,stoScale,conScale2,stoScale2,costLimit,powertrainVariant,powertr
ainSelection)

if ~nargin
    vehMass = [];   % Vehicle mass
    massLimit = [];
    drivecycleType = [];
    drivecycleRepeat = [];
    fdRatio = [];
    conScale = [];  % Scale of primary energy converter from 0 - 100
    stoScale = [];  % Scale of primary energy storage from 0 - 100
    conScale2 = []; % Scale of secondary energy converter from 0 - 100
    stoScale2 = []; % Scale of secondary energy storage from 0 - 100
    costLimit = [];
    powertrainVariant = [];
    powertrainSelection = [];
end


%% *** INITIALISE SIGNATURE ***

if isempty(vehMass)
    vehMass = 1000;
end

if isempty(massLimit)
    massLimit = 10000;
end

% Drivecycle to Use
% 0 - Blank
% 1 - NEDC
% 2 - Cranfield
% 3 - Artemis

if isempty(drivecycleType)
    drivecycleType = 1;
end

if isempty(fdRatio)
    fdRatio = 5;
end
```

```
if isempty(conScale)
    conScale = 50;
end

if isempty(stoScale)
    stoScale = 50;
end

if isempty(conScale2)
    conScale2 = 50;
end

if isempty(stoScale2)
    stoScale2 = 50;
end

if isempty(costLimit)
    costLimit = 1e9;
end

if isempty(powertrainSelection)
    powertrainSelection = 1:8; % Adjust maximum powertrain variants
here
end

if isempty(powertrainVariant)
    powertrainVariant = 1;
end

if checkRoundNumbers([conScale stoScale conScale2 stoScale2
powertrainVariant]) == 0
    keyboard;
end


%% *** MAP POWERTRAIN SELECTION TO POWERTRAIN VARIANTS ***

initVariant; % Remember to adjust maximum powertrain variants here
Powertrain = powertrainSelection(powertrainVariant);


%% *** INITIALISE VARIABLES ***

in = getDrivecycle(drivecycleType,[],drivecycleRepeat);
in.vehMass = vehMass;

in.sim_stoptime = max(in.dc_time);

in.batIniSOC = 89;  % Initial battery SOC (%)
in.batIniSOH = 100; % Initial battery SOH (%)
in.fd = fdRatio;
in.mu_aero = 0.3;
in.veh_wheelr = 0.3704;
in.sim_ts = 1;
in.busVoltage = 400;
```

```
in.thermoControlPoint = 30;
in.vehMode = 0; % Used for EV to switch between charge/running a
drivecycle


%% *** INITIALISE COMPONENTS ***

% Powertrain Selection
% 1 - Conventional Powertrain
% 2 - EV
% 3 - Series PHEV
% 4 - Fuel Cell + Ultracap
% 5 - Parallel Flywheel + CVT
% 6 - Battery + Ultracap
% 7 - EV (with SOH)
% 8 - Battery (with SOH) + Ultracap

switch Powertrain
    case 1
        inA = initEngine(conScale,1);
        inB = initTank(stoScale,1);
        inC = initGearbox(in.dc_speed.*3.6,1);

    case 2
        inA = initMachine(conScale,1,[]);
        inB = initBattery(stoScale,in.batIniSOC,1,0,[]);
        inC = initGearbox(in.dc_speed.*3.6,2);

    case 3
        inA = initMachine(conScale,1,[]);
        inB = initBattery(stoScale,in.batIniSOC,1,0,[]);
        inC = initGearbox(in.dc_speed.*3.6,2);
        inD = initGenSet(conScale2);
        inE = initTank(stoScale2,2);

    case 4
        inA = initMachine(conScale,1,[]);
        inB = initUltraCap(stoScale);
        inC = initGearbox(in.dc_speed.*3.6,2);
        inD = initFuelCell(conScale2);
        inE = initTankFC(stoScale2);

    case 5
        inA = initEngine(conScale,1);
        inB = initTank(stoScale,1);
        inC = initGearbox(in.dc_speed.*3.6,1);
        inD = initCVT(conScale2);
        inE = initFlywheel(stoScale2);

    case 6
        inA = initMachine(conScale,1,50);
        inB = initUltraCap(stoScale);
        inC = initGearbox(in.dc_speed.*3.6,2);
        inD = initNull_con(conScale2);
        inE = initBattery(stoScale2,in.batIniSOC,2,0,[]);
```

```
    case 7
        inA = initMachine(conScale,1,[]);
        inB = initBattery(stoScale,in.batIniSOC,1,1,in.batIniSOH);
        inC = initGearbox(in.dc_speed.*3.6,2);

    case 8
        inA = initMachine(conScale,1,50);
        inB = initUltraCap(stoScale);
        inC = initGearbox(in.dc_speed.*3.6,2);
        inD = initNull_con(conScale2);
        inE = initBattery(stoScale2,in.batIniSOC,2,1,in.batIniSOH);

    otherwise
        disp('Invalid powertrain selection');
end

inTemp = in;
switch Powertrain
    case {1,2,7}
        in = mergeStruct(inTemp,inA,inB,inC);
        in.costT = in.costA + in.costB + in.costC;
        in.massT = in.vehMass + in.massA + in.massB + in.massC;
        in.hybridType = 0;
    case 5
        in = mergeStruct(inTemp,inA,inB,inC,inD,inE);
        in.costT = in.costA + in.costB + in.costC + in.costD +
in.costE;
        in.massT = in.vehMass + in.massA + in.massB + in.massC +
in.massD + in.massE;
        in.hybridType = 1;
    otherwise
        in = mergeStruct(inTemp,inA,inB,inC,inD,inE);
        in.costT = in.costA + in.costB + in.costC + in.costD +
in.costE;
        in.massT = in.vehMass + in.massA + in.massB + in.massC +
in.massD + in.massE;
        in.hybridType = 0;
end


%% *** RUN SIMULATION ***

if in.costT < costLimit
    if in.massT < massLimit
        simu = runSimu(in,Powertrain);
    end
end


%% *** POST-PROCESSING ***
% keyboard;

if in.costT < costLimit
    if in.massT < massLimit
        simu.distance = trapz(simu.t,simu.speed);

        switch Powertrain
```

```
            case 1
                simuA = simuEngine(in,simu);

            case {2,6}
                simuA = simuMachine(in,simu,Powertrain);

            case 3
                simuA = simuGenSet(in,simu,Powertrain);

            case 4
                simuA = simuFuelCell(in,simu,Powertrain);

            case 5
                simuA = simuFlywheel(in,simu);

            case {7,8}
                simuA = simuSOH(in,simu,Powertrain);

            otherwise
                disp('Invalid powertrain post-processing');
        end

        simuTemp = simu;
        simu = mergeStruct(simuTemp,simuA);
    else
        simu.wtw_CO2 = inf;
        simu.ttw_CO2 = inf;
    end
else
    simu.wtw_CO2 = inf;
    simu.ttw_CO2 = inf;
end

% keyboard;
end


function confirmRound = checkRoundNumbers(inputArray)
% Redundant check to ensure that inputs are round numbers
confirmRound = 1;

for i = 1:length(inputArray)
    if inputArray(i) ~= round(inputArray(i))
        disp('Error: inputs are not integer values!');
        confirmRound = 0;
    end
end
end
```

# REFERENCES


[1] Proost, S. and van Dender, K., (2010), *What Sustainable Road Transport Future?*, Organisation for Economic Co-operation and Development.

[2] Chan, C. C. (2007), "The State of the Art of Electric, Hybrid, and Fuel Cell Vehicles", *Proceedings of the IEEE,* vol. 95, no. 4, pp. 704-718.

[3] Rieveley, R. J. and Minaker, B. P. *Variable Torque Distribution For Advanced Hybrid Electric Powertrains,* Department of Mechanical, Automotive, & Materials Engineering, University of Windsor, Windsor, Ontario, Canada.

[4] Cross, D. and Hilton, J. (2008), "High Speed Flywheel Based Hybrid Systems for Low Carbon Vehicles", *Hybrid and Eco-Friendly Vehicle Conference, 2008. IET HEVC 2008,* pp. 1.

[5] Diamond, D. (2009), "The impact of government incentives for hybrid-electric vehicles: Evidence from US states", *Energy Policy,* vol. 37, no. 3, pp. 972-983.

[6] Li, X. and Williamson, S. S. (2007), "Comparative investigation of series and parallel hybrid electric vehicle (HEV) efficiencies based on comprehensive parametric analysis", *Vehicle Power and Propulsion Conference, 2007. VPPC 2007. IEEE,* IEEE, pp. 499.

[7] Van Mierlo, J., Maggetto, G. and Lataire, P. (2006), "Which energy source for road transport in the future? A comparison of battery, hybrid and fuel cell vehicles", *Energy Conversion and Management,* vol. 47, no. 17, pp. 2748-2760.

[8] Offer, G., Howey, D., Contestabile, M., Clague, R. and Brandon, N. (2010), "Comparative analysis of battery electric, hydrogen fuel cell and hybrid vehicles in a future sustainable road transport system", *Energy Policy,* vol. 38, no. 1, pp. 24-29.

[9] Bento, N. (2010), "Dynamic competition between plug-in hybrid and hydrogen fuel cell vehicles for personal transportation", *International Journal of Hydrogen Energy,* vol. 35, no. 20, pp. 11271-11283.

[10] Offer, G. J., Contestabile, M., Howey, D. A., Clague, R. and Brandon, N. P. (2011), "Techno-economic and behavioural analysis of battery electric, hydrogen fuel cell and hybrid vehicles in a future sustainable road transport system in the UK", *Energy Policy,* vol. 39, pp. 1939.

[11] Salisa, A. R., Zhang, N. and Zhu, J. G. (2011), "A Comparative Analysis of Fuel Economy and Emissions Between a Conventional HEV and the UTS PHEV", *Vehicular Technology, IEEE Transactions on,* vol. 60, no. 1, pp. 44-54.

[12] Nzisabira, J., Louvigny, Y. and Duysinx, P. (2009), "Comparison of ultra capacitors, hydraulic accumulators and batteries technologies to optimize hybrid vehicle ecoefficiency", *Power Engineering, Energy and Electrical Drives, 2009. POWERENG '09. International Conference on,* pp. 353.

[13] Ribau, J., Silva, C., Brito, F. P. and Martins, J. (2012), "Analysis of four-stroke, Wankel, and microturbine based range extenders for electric vehicles", *Energy Conversion and Management,* vol. 58, pp. 120-133.

[14] Boretti, A. (2010), "Comparison of fuel economies of high efficiency diesel and hydrogen engines powering a compact car with a flywheel based kinetic energy recovery systems", *International Journal of Hydrogen Energy,* vol. 35, no. 16, pp. 8417-8424.

[15] Williamson, S. S. and Emadi, A. (2005), "Comparative assessment of hybrid electric and fuel cell vehicles based on comprehensive well-to-wheels efficiency analysis", *Vehicular Technology, IEEE Transactions on,* vol. 54, no. 3, pp. 856-862.

[16] An, F., & Santini, D. (2003). *Assessing tank-to-wheel efficiencies of advanced technology vehicles* (No. 2003-01-0412). SAE Technical Paper.

[17] Weiss, M. A., Heywood, J. B., Drake, E. M., Schafer, A. and AuYeung, F. F. (2000), "On the Road in 2020", *Energy Laboratory Report# MIT EL 00-003, Massachusetts Institute of Technology*.

[18] Wang, M., *Well-to-wheel energy use and greenhouse gas emissions of advanced fuel/vehicle systems North American analysis*. No. ANL/ES/RP-104528. Argonne National Lab., IL (US), 2001.

[19] Walker, A., McGordon, A., Hannis, G., Picarelli, A., Breddy, J., Carter, S., Vinsome, A., Jennings, P., Dempsey, M. and Willows, M. (2006), "A novel structure for comprehensive HEV powertrain modelling", *Vehicle Power and Propulsion Conference, 2006. VPPC'06. IEEE,* IEEE, pp. 1.

[20] Fontaras, G., Pistikopoulos, P. and Samaras, Z. (2008), "Experimental evaluation of hybrid vehicle fuel economy and pollutant emissions over real-world simulation driving cycles", *Atmospheric Environment,* vol. 42, no. 18, pp. 4023-4035.

[21] Milliken, W. F., Milliken, D. L. and Metz, L. D. (1995), *Race car vehicle dynamics,* SAE International Warrendale, PA.

[22] Mohan, G., Assadian, F. and Longo, S. (2013), "An Optimization Framework for Comparative Analysis of Multiple Vehicle Powertrains", *Energies*.

[23] Mohan, G., Assadian, F. and Marco, J. (2012), "Influence of Cost Function on EV Powertrain Sizing", *Powertrain Modelling and Control,* September 4, Bradford.

[24] Mohan, G. "Comparative Analysis of Multiple Powertrain Architectures based on a Novel Optimization Framework", *Training*, vol. 2014, pp. 06-09.

[25] Markel, T., Brooker, A., Hendricks, T., Johnson, V., Kelly, K., Kramer, B., O'Keefe, M., Sprik, S. and Wipke, K. (2002), "ADVISOR: a systems analysis tool for advanced vehicle modeling", *Journal of Power Sources*, vol. 110, no. 2, pp. 255-266.

[26] Gao, D. W., Mi, C. and Emadi, A. (2007), "Modeling and Simulation of Electric and Hybrid Vehicles", *Proceedings of the IEEE*, vol. 95, no. 4, pp. 729-745.

[27] Guzzella, L. and Amstutz, A. (1999), "CAE tools for quasi-static modeling and optimization of hybrid powertrains", *Vehicular Technology, IEEE Transactions on*, vol. 48, no. 6, pp. 1762-1769.

[28] Contestabile, M., Offer, G. J., Slade, R., Jaeger, F. and Thoennes, M. (2011), "Battery electric vehicles, hydrogen fuel cells and biofuels. Which will be the winner?", *Energy & Environmental Science*, vol. 4, no. 10, pp. 3754-3772.

[29] Van Mierlo, J., Van den Bossche, P. and Maggetto, G. (2004), "Models of energy sources for EV and HEV: Fuel cells, batteries, ultracapacitors, flywheels, and engine-generators", *Journal of Power Sources*, vol. 128, pp. 76.

[30] Assanis, D., Delagrammatikas, G., Fellini, R., Filipi, Z., Liedtke, J., Michelena, N., Papalambros, P., Reyes, D., Rosenbaum, D., Sales, A. and Sasena, M. (1999), "An Optimization Approach to Hybrid Electric Propulsion System Design", *Mechanics of Structures and Machines*, vol. 27, no. 4, pp. 365.

[31] Rizzoni, G., Guzzella, L. and Baumann, B. M. (1999), "Unified modeling of hybrid electric vehicle drivetrains", *Mechatronics, IEEE/ASME Transactions on*, vol. 4, no. 3, pp. 246-257.

[32] Wipke, K. B., Cuddy, M. R. and Burch, S. D. (1999), "ADVISOR 2.1: a user-friendly advanced powertrain simulation using a combined backward/forward approach", *Vehicular Technology, IEEE Transactions on*, vol. 48, no. 6, pp. 1751-1761.

[33] Hofman, T., Steinbuch, M., van Druten, R. and Serrarens, A. (2009), "Design of CVT-based hybrid passenger cars", *Vehicular Technology, IEEE Transactions on*, vol. 58, no. 2, pp. 572-587.

[34] Oh, S. C. (2005), "Evaluation of motor characteristics for hybrid electric vehicles using the hardware-in-the-loop concept", *Vehicular Technology, IEEE Transactions on*, vol. 54, no. 3, pp. 817-824.

[35] Katrašnik, T. (2007), "Hybridization of powertrain and downsizing of IC engine–A way to reduce fuel consumption and pollutant emissions–Part 1", *Energy Conversion and Management*, vol. 48, no. 5, pp. 1411-1423.

[36] Xiong, W., Zhang, Y. and Yin, C. (2009), "Optimal energy management for a series–parallel hybrid electric bus", *Energy conversion and management,* vol. 50, no. 7, pp. 1730-1738.

[37] Hauer, K. and Moore, R. (2003), "Fuel Cell Vehicle Simulation–Part 1: Benchmarking Available Fuel Cell Vehicle Simulation Tools", *Fuel cells,* vol. 3, no. 3, pp. 84-94.

[38] Same, A., Stipe, A., Grossman, D. and Park, J. W. (2010), "A study on optimization of hybrid drive train using Advanced Vehicle Simulator (ADVISOR)", *Journal of Power Sources,* vol. 195, no. 19, pp. 6954-6963.

[39] Harrington. (Cranfield University), (2012), *Low Carbon Vehicle Technology Project Workstream 6 Final Report: Vehicle Supervisory Control Task 6.1 Reusable Reference Architecture,* Warwick Manufacturing Group.

[40] Harrington, C. M., Marco, J. and Vaughan, N. D. (2012), "The Design of a Reference Control Architecture to Support Vehicle Hybridisation", *International Journal of Vehicle Design (IJVD),* no. Special Issue on: "Automotive Mechatronics: Innovations in Design, Analysis and Implementation".

[41] Orie, C. J. and Nwatu, Q. I. (2011), "Challenges of Energy Saving Crisis as a Panacea to Hybrid Electric Vehicle (HEV)", *Mediterranean Journal of Social Sciences,* pp. 67.

[42] Vahabzadeh, H. and Linzell, S. M. (1992), "Modeling, Simulation and Control Implementation for a Split-Torque, Geared-Neutral, Infinitely Variable Transmission", *SAE transactions,* vol. 100, pp. 546-546.

[43] Jinming Liu and Huei Peng (2008), "Modeling and Control of a Power-Split Hybrid Vehicle", *Control Systems Technology, IEEE Transactions on,* vol. 16, no. 6, pp. 1242-1251.

[44] Voelcker, J. (2011), "Chevy Volt sparks a series of plug-in hybrids", *Spectrum, IEEE,* vol. 48, no. 2, pp. 16-18.

[45] Jonasson, K. (2002), *Analysing Hybrid Drive System Topologies* (Licentiate thesis), Lund University, Sweden.

[46] Miller, J. M. and Nicastri, P. R. (1998), "The next generation automotive electrical power system architecture: issues and challenges", *Digital Avionics Systems Conference, 1998. Proceedings., 17th DASC. The AIAA/IEEE/SAE,* Vol. 2, pp. I15/1.

[47] Lianghong Wu, Yaonan Wang, Xiaofang Yuan and Zhenlong Chen (2011), "Multiobjective Optimization of HEV Fuel Economy and Emissions Using the Self-Adaptive Differential Evolution Algorithm", *Vehicular Technology, IEEE Transactions on,* vol. 60, no. 6, pp. 2458-2470.

[48] Wu, J., Zhang, C. and Cui, N. (2008), "PSO algorithm-based parameter optimization for HEV powertrain and its control strategy", *International Journal of Automotive Technology,* vol. 9, no. 1, pp. 53-59.

[49] Wenzhong Gao and Porandla, S. K. (2005), "Design optimization of a parallel hybrid electric powertrain", *Vehicle Power and Propulsion, 2005 IEEE Conference,* pp. 6.

[50] Bauman, J. and Kazerani, M. (2008), "A Comparative Study of Fuel-Cell–Battery, Fuel-Cell–Ultracapacitor, and Fuel-Cell–Battery–Ultracapacitor Vehicles", *Vehicular Technology, IEEE Transactions on,* vol. 57, no. 2, pp. 760-769.

[51] Bauman, J. and Kazerani, M. (2009), "An Analytical Optimization Method for Improved Fuel Cell–Battery–Ultracapacitor Powertrain", *Vehicular Technology, IEEE Transactions on,* vol. 58, no. 7, pp. 3186-3197.

[52] de Sisternes, F. J. (2010), *Plug-In Electric Vehicle Introduction in the EU* (MSc thesis), Massachusetts Institute of Technology, USA.

[53] Douglas, C. and Stewart, A. (2011), "Influences on the Low Carbon Car Market from 2020–2030, Final Report".

[54] Regulation, E. "443/2009 of the European Parliament and of the Council of 23 April 2009 setting emission performance standards for new passenger cars as part of the Community's integrated approach to reduce CO2 emissions from light-duty vehicles. Official Register of the European Union", *eur-lex.europa.eu/Notice.do*.

[55] DEFRA (2013), "Government GHG Conversion Factors for Company Reporting", *London: Department for Environment, Food and Rural Affairs and Department for Energy and Climate Change*.

[56] Anderson, T., Christophersen, O., Pickering, K., Southwood, H. and Tipping, S. (2009), "National Travel Survey 2008 Technical Report", *Department for Transport, National Centre for Social Research*.

[57] Lucas, A., Neto, R. C. and Silva, C. A. (2013), "Energy supply infrastructure LCA model for electric and hydrogen transportation systems", *Energy,* vol. 56, no. 0, pp. 70-80.

[58] Mira, A. A. and Wanib, M. M. (2015), "Computational Analysis of Performance and Emissions of a Compression Ignition Engine under various Air Induction Methods", *Int.J.of Thermal & Environmental Engineering,* vol. 9, no. 1, pp. 47-52.

[59] Özkan, M. (2015), "A Comparative Study on Energy and Exergy Analyses of a CI Engine Performed with Different Multiple Injection Strategies at Part Load: Effect of Injection Pressure", *Entropy,* vol. 17, no. 1, pp. 244-263.

[60] Vítek, O., Macek, J., & Polášek, M. (2003). *Simulation of pre-chambers in an engine combustion chamber using available software* (No. 2003-01-0373). SAE Technical Paper.

[61] Rousseau, A. and Pasquier, M. (2001), "Validation of a hybrid modeling software (PSAT) using its extension for prototyping (PSAT-PRO)", *Proceedings of the 2001 Global Powertrain Congress, Detroit, MI, USA,* pp. 1.

[62] Guzzella, L. and Sciarretta, A. (2005), *Vehicle propulsion systems: introduction to modeling and optimization,* Springer.

[63] Karnopp, D. C., Margolis, D. L. and Rosenberg, R. C. (2012), *System Dynamics: Modeling, Simulation, and Control of Mechatronic Systems,* Wiley.

[64] Rousseau, A., Sharer, P. and Besnier, F. (2004), "Feasibility of reusable vehicle modeling: application to hybrid vehicle", *SAE SP*, pp. 293-302.

[65] Wilkins, S. and Lampérth, M. (2002), "An Object-Oriented modelling tool of Hybrid Powertrains for vehicle performance simulation", *Proc.of EVS19*.

[66] Ribau, J. P., Sousa, J. M. C. and Silva, C. M. (2013), "Plug-In Hybrid Vehicle Powertrain Design Optimization: Energy Consumption and Cost", vol. 191, pp. 595-613.

[67] Burke, A. F. and Miller, M. (2009), *Simulated Performance of Alternative Hybrid-Electric Powertrains in Vehicles on Various Driving Cycles,* Institute of Transportation Studies, University of California, Davis.

[68] Karbowski, D., Rousseau, A., Pagerit, S. and Sharer, P. (2006), "Plug-in vehicle control strategy: from global optimization to real time application", *22nd Electric Vehicle Symposium, EVS22, Yokohama, Japan.*

[69] Wu, X., Cao, B., Li, X., Xu, J. and Ren, X. (2011), "Component sizing optimization of plug-in hybrid electric vehicles", *Applied Energy,* vol. 88, no. 3, pp. 799-804.

[70] Delagrammatikas, G. and Assanis, D. (2004), "Development of a neural network model of an advanced, turbocharged diesel engine for use in vehicle-level optimization studies", *Proceedings of the Institution of Mechanical Engineers, Part D: Journal of Automobile Engineering,* vol. 218, no. 5, pp. 521-533.

[71] Rousseau, A., Pagerit, S. and Gao, D. (2007), "Plug-in hybrid electric vehicle control strategy parameter optimization", *Argonne National Laboratory*.

[72] Hofman, T., Steinbuch, M., van Druten, R. and Serrarens, A. (2007), "Parametric modeling of components for selection and specification of hybrid vehicle drivetrains", *WEVA J*, vol. 1, no. 1, pp. 215-224.

[73] Senger, R. D., Merkle, M. A. and Nelson, D. J. (1998), "Validation of ADVISOR as a simulation tool for a series hybrid electric vehicle", *Polymer,* vol. 2013, pp. 02-11.

[74] Matheson, P. and Stecki, J. (2003), "Development and simulation of a hydraulic-hybrid powertrain for use in commercial heavy vehicles", *SAE transactions,* vol. 112, no. 2, pp. 114-123.

[75] Ogburn, Michael James. *Systems integration, modeling, and validation of a fuel cell hybrid electric vehicle*. Dissertation. Virginia Polytechnic Institute and State University, 2000.

[76] Borutzky, W. (1999), "Bond graph modeling from an object oriented modeling point of view", *Simulation Practice and Theory,* vol. 7, no. 5–6, pp. 439-461.

[77] Mason, B. A., Ebrahimi, M. and Farid, M. (2009), "Reconfigurable modelling for drivetrain real-time simulation", *Proceedings of the Institution of Mechanical Engineers, Part K: Journal of Multi-body Dynamics,* vol. 223, no. 4, pp. 309-323.

[78] Silva, C., Ross, M. and Farias, T. (2009), "Evaluation of energy consumption, emissions and cost of plug-in hybrid vehicles", *Energy Conversion and Management,* vol. 50, no. 7, pp. 1635-1643.

[79] Walsh, C., Carroll, S., Eastlake, A. and Blythe, P. (2010), "Electric vehicle driving style and duty variation performance study", *University of Sheffield2010.*

[80] "Proposal for a regulation of the European Parliament and of the European Council setting emission performance standards for new passenger cars as part of the Community's integrated approach to reduce CO2 emissions from light duty vehicles", (2007), *EC,* vol. COM(2007) 856 final.

[81] Naigt (2009), *An Independent Report on the Future of the Automotive Industry in the UK,* BERR2009.

[82] Bandivadekar, A. (2008), *On the road in 2035: Reducing transportation's petroleum consumption and GHG emissions,* Massachusetts Institute of Technology.

[83] Bohac, S. V., Baker, D. M. and Assanis, D. N. (1996), "A global model for steady state and transient SI engine heat transfer studies", *SAE transactions,* vol. 105, pp. 196-214.

[84] Economic Commission for Europe (2004), "Proposal for Draft Amendment to the 05 Series of Amendments to Regulation No. 83 (Emissions of M1 and N1 Categories of Vehicles)", *Inland Transport Committee, World Forum for Harmonization of Vehicle Regulation (WP. 29), Working Party on Pollution and Energy (49th GRPE),* Vol. 4.

[85] Daimler AG (2011), *Technical data - Smart Fortwo*, available at: http://media.daimler.com/dcmedia/smart/en (accessed December 2011).

[86] Vehicle Certification Agency (VCA) (2014), *Car fuel data, $CO_2$ and vehicle tax tools*, available at: http://carfueldata.direct.gov.uk/ (accessed January 2015).

[87] Woolmer, T. J. and McCulloch, M. D. (2007), "Analysis of the Yokeless And Segmented Armature Machine", *Electric Machines & Drives Conference, 2007. IEMDC '07. IEEE International*, Vol. 1, pp. 704.

[88] Bumby, J. R., Spooner, E. and Jagiela, M. (2006), "Solid Rotor Induction Machines for use in Electrically-Assisted Turbochargers", *Power Electronics, Machines and Drives, 2006. The 3rd IET International Conference on*, pp. 341.

[89] Chuang Yu, Xiaodong Zhang, Shuang Gao and Diyun Wu (2010), "Comparison of permanent magnet brushless motors for electric vehicles", *Vehicle Power and Propulsion Conference (VPPC), 2010 IEEE*, pp. 1.

[90] Ehsani, M., Yimin Gao and Gay, S. (2003), "Characterization of electric motor drives for traction applications", *Industrial Electronics Society, 2003. IECON '03. The 29th Annual Conference of the IEEE*, Vol. 1, pp. 891.

[91] *Zytek Automotive. Zytek IDT 120-55 integrated 55kw electric engine*, available at: http://www.zytekautomotive.co.uk/ (accessed February 2011).

[92] Smart USA (2012), *Smart Electric Drive*, available at: http://www.smartusa.com/models/electric-drive/overview.aspx (accessed February 2012).

[93] André, M. (2004), "The ARTEMIS European driving cycles for measuring car pollutant emissions", *Science of The Total Environment*, vol. 334–335, no. 0, pp. 73-84.

[94] Cenex UK (2011), *Smart Move 2 Electric Vehicle Trial*, available at: http://www.cenex.co.uk/projects/electric-vehicle-trials/smart-move-2 (accessed May).

[95] Amrhein, M. and Krein, P. T. (2005), "Dynamic simulation for analysis of hybrid electric vehicle system and subsystem interactions, including power electronics", *Vehicular Technology, IEEE Transactions on*, vol. 54, no. 3, pp. 825-836.

[96] Lukic, S. M. and Emadi, A. (2004), "Effects of drivetrain hybridization on fuel economy and dynamic performance of parallel hybrid electric vehicles", *Vehicular Technology, IEEE Transactions on*, vol. 53, no. 2, pp. 385-389.

[97] GKN Driveline (2015), *GKN - EVO Electric Product Datasheet*, available at: www.gkn.com/driveline/our-solutions/edrive-systems/eMachines/Pages/default.aspx (accessed January 2015).

[98] YASA Motors (2014), *YASA Motors Product Datasheet*, available at: http://www.yasamotors.com/products/ (accessed January 2015).

[99] Powell, B. K. and Pilutti, T. E. (1994), "A Range Extender Hybrid Electric Vehicle dynamic model", *Decision and Control, 1994., Proceedings of the 33rd IEEE Conference on*, Vol. 3, pp. 2736.

[100] Turner, J. W. G., Blake, D., Moore, J., Burke, P., Pearson, R. J., Patel, R., Blundell, D. W., Chandrashekar, R. B., Matteucci, L. and Barker, P. C. C. A. (2010), *The Lotus Range Extender Engine*, 2010-01-2208, SAE International, USA.

[101] *Bosch Automotive Handbook*, (2007), 7th Edition ed, Robert Bosch GmbH, Germany.

[102] Harrington, C. M., Marco, J., Vaughan, N. D., Kellaway, M., Cooper, A. and Eastlake, A. (2008), "Affordable Hybrid Electric System for Urban Commercial Vehicle Applications, Using Advanced VRLA Battery", *Hybrid and Eco-Friendly Vehicle Conference, 2008. IET HEVC 2008*, pp. 1.

[103] Van den Bossche, P., Vergels, F., Van Mierlo, J., Matheys, J. and Van Autenboer, W. (2006), "SUBAT: An assessment of sustainable battery technology", *Journal of Power Sources*, vol. 162, no. 2, pp. 913-919.

[104] Kalhammer, F., Kopf, B., Swan, D., Roan, V. and Walsh, M. (2007), *Status and Prospects for Zero Emissions Vehicle Technology Report of the ARB Independent Expert Panel 2007*, California Air Resources Board, Sacramento, CA. USA.

[105] Burke, A. F. (2007), "Batteries and Ultracapacitors for Electric, Hybrid, and Fuel Cell Vehicles", *Proceedings of the IEEE*, vol. 95, no. 4, pp. 806-820.

[106] Gao, W. (2005), "Performance Comparison of a Fuel Cell-Battery Hybrid Powertrain and a Fuel Cell-Ultracapacitor Hybrid Powertrain", *IEEE Transactions On Vehicular Technology*, vol. 54, no. 3, pp. 846.

[107] Antaloae and Marco, J. (Low Carbon Vehicle Technology Project), (2010), *Literature review on Li-ion battery modelling* Cranfield University.

[108] Tremblay, O., Dessaint, L. A. and Dekkiche, A. I. (2007), "A generic battery model for the dynamic simulation of hybrid electric vehicles", *Vehicle Power and Propulsion Conference*, IEEE, pp. 284.

[109] He, H., Xiong, R. and Fan, J. (2011), "Evaluation of lithium-ion battery equivalent circuit models for state of charge estimation by an experimental approach", *Energies,* vol. 4, no. 4, pp. 582-598.

[110] Panasonic Corporation (2010), *Panasonic NCR18650 NNP series*, available at: http://industrial.panasonic.com/www-data/pdf2/ACA4000/ACA4000CE240.pdf (accessed May 27).

[111] Plett, G. L. (2004), "Extended Kalman filtering for battery management systems of LiPB-based HEV battery packs: Part 1. Background", *Journal of Power Sources,* vol. 134, no. 2, pp. 252-261.

[112] Rodrigues, S., Munichandraiah, N. and Shukla, A. (1999), "AC impedance and state-of-charge analysis of a sealed lithium-ion rechargeable battery", *Journal of Solid State Electrochemistry,* vol. 3, no. 7-8, pp. 397-405.

[113] Hensher, D. A. and Puckett, S. M. (2005), "Road user charging: The global relevance of recent developments in the United Kingdom", *Road User Charging: Theory and Practices,* vol. 12, pp. 377.

[114] MacKay, D., ( 2008), *Sustainable Energy, without the hot air,* Cambridge: UIT Cambridge.

[115] Kim, S. and Dale, B. E. (2005), "Environmental aspects of ethanol derived from no-tilled corn grain: nonrenewable energy consumption and greenhouse gas emissions", *Biomass and Bioenergy,* vol. 28, pp. 475.

[116] Karl Georg, H. (2008), "The history of alternative fuels in transportation: The case of electric and hybrid cars", *Utilities Policy,* vol. 16, no. 2, pp. 63-71.

[117] Liberman, M. A. (2008), *Introduction to Physics and Chemistry of Combustion: Explosion, Flame, Detonation,* Springer.

[118] EPA, (2011), *Inventory of US greenhouse gas emissions and sinks: 1990-2009.*

[119] Liu, H. and Jiang, J. (2007), "Flywheel energy storage—An upswing technology for energy sustainability", *Energy and Buildings,* vol. 39, no. 5, pp. 599-604.

[120] Cross, D. and Brockbank, C. (2009), "Mechanical hybrid system comprising a flywheel and CVT for motorsport and mainstream automotive applications", *SAE Technical Paper,* pp. 01-1312.

[121] Doucette, R. T. and McCulloch, M. D. (2011), "A comparison of high-speed flywheels, batteries, and ultracapacitors on the bases of cost and fuel economy as the energy storage system in a fuel cell based hybrid electric vehicle", *Journal of Power Sources,* vol. 196, no. 3, pp. 1163-1170.

[122] Birch, S. and RSC, R. S. C. (2011), "Volvo spins up flywheel technology research", *Fuel,* vol. 2014, pp. 11-11.

[123] Nuo Xu, Huiyan CHen, Yuhui Hu and Haiou Liu (2007), "The Integrated Control System in Automatic Transmission", *Mechatronics and Automation, 2007. ICMA 2007. International Conference on,* pp. 1655.

[124] Irimescu, A., Mihon, L. and Pãdure, G. (2011), "Automotive transmission efficiency measurement using a chassis dynamometer", *International Journal of Automotive Technology,* vol. 12, no. 4, pp. 555-559.

[125] Gong, S. (2013), "A generalized IC engine propulsion method and corresponding transmission design for improving vehicle fuel efficiency", *European Transport Research Review,* pp. 1-15.

[126] Viet, N. D. (2012). *Gear Shift Strategies for Automotive Transmissions* (Doctoral dissertation, PhD thesis, Eindhoven Technical University).

[127] Xuefang Lin-Shi, Morel, F., Llor, A. M., Allard, B. and Retif, J. -. (2007), "Implementation of Hybrid Control for Motor Drives", *Industrial Electronics, IEEE Transactions on,* vol. 54, no. 4, pp. 1946-1952.

[128] O'Keefe, M., Brooker, A., Johnson, C., Mendelsohn, M., Neubauer, J. and Pesaran, A. (2010), *Battery ownership model: a tool for evaluating the economics of electrified vehicles and related infrastructure,* National Renewable Energy Laboratory.

[129] Simpson, A. (2006), *Cost-benefit analysis of plug-in hybrid electric vehicle technology,* National Renewable Energy Laboratory, Golden.

[130] Markel, T. and Simpson, A. (2006), "Cost-benefit analysis of plug-in hybrid electric vehicle technology", *22nd International Electric Vehicle Symposium.*

[131] Committee on Transitions to Alternative Vehicles and Fuels (2013), "Transitions to Alternative Vehicles and Fuels".

[132] Alkidas, A. C. (2007), "Combustion advancements in gasoline engines", *Energy Conversion and Management,* vol. 48, no. 11, pp. 2751-2761.

[133] Moura, S. J., Callaway, D. S., Fathy, H. K. and Stein, J. L. (2008), "Impact of battery sizing on stochastic optimal power management in plug-in hybrid electric vehicles", *Vehicular Electronics and Safety, 2008. ICVES 2008. IEEE International Conference on,* IEEE, pp. 96.

[134] Barlow, T., Latham, S., McCrae, I. and Boulter, P. (2009), *A reference book of driving cycles for use in the measurement of road vehicle emissions.*

[135] André, M., Joumard, R., Vidon, R., Tassel, P. and Perret, P. (2006), "Real-world European driving cycles, for measuring pollutant emissions from high-and low-powered cars", *Atmospheric Environment,* vol. 40, no. 31, pp. 5944-5953.

[136] Shankar, R., Marco, J. and Carroll, S. (2011), "Performance of an EV during real-world usage", *Cenex Hybrid Electric Vehicle Conference, UK.*

[137] Tzirakis, E., Pitsas, K., Zannikos, F. and Stournas, S. (2006), "Vehicle emissions and driving cycles: comparison of the Athens driving cycle (ADC) with ECE-15 and European driving cycle (EDC)", *Global NEST Journal,* vol. 8, no. 3, pp. 282-290.

[138] Kuhler, M., & Karstens, D. (1978). *Improved driving cycle for testing automotive exhaust emissions* (No. 780650). SAE Technical Paper.

[139] Ericsson, E. (2001), "Independent driving pattern factors and their influence on fuel-use and exhaust emission factors", *Transportation Research Part D: Transport and Environment,* vol. 6, no. 5, pp. 325-345.

[140] De Vlieger, I., De Keukeleere, D. and Kretzschmar, J. (2000), "Environmental effects of driving behaviour and congestion related to passenger cars", *Atmospheric Environment,* vol. 34, no. 27, pp. 4649-4655.

[141] Hayes, J. G., de Oliveira, R Pedro R, Vaughan, S. and Egan, M. G. (2011), "Simplified electric vehicle power train models and range estimation", *Vehicle Power and Propulsion Conference (VPPC), 2011 IEEE,* IEEE, pp. 1.

[142] The MathWorks, I. (2014), *Variant Subsystem*, available at: http://www.mathworks.com/help/simulink/slref/variantsubsystem.html (accessed February 2014).

[143] Man, K., Tang, K. and Kwong, S. (1996), "Genetic algorithms: concepts and applications", *IEEE Transactions on Industrial Electronics,* vol. 43, no. 5, pp. 519-534.

[144] Kennedy, J. and Eberhart, R. (1995), "Particle swarm optimization", *Proceedings of IEEE international conference on neural networks,* Vol. 4, Perth, Australia, pp. 1942.

[145] Goldberg, D. E. (1989), *Genetic Algorithms in Search, Optimization and Machine Learning,* Addison-Wesley Longman Publishing Co., Inc.

[146] Houck, C. R., Joines, J. and Kay, M. G. (1995), "A genetic algorithm for function optimization: a Matlab implementation", *NCSU-IE TR,* vol. 95, no. 09.

[147] Fukuyama, Y. and Yoshida, H. (2001), "A particle swarm optimization for reactive power and voltage control in electric power systems", *Evolutionary Computation, 2001. Proceedings of the 2001 Congress on,* Vol. 1, IEEE, pp. 87.

[148] Kuo, Y. and Li, T. (1999), "GA-based fuzzy PI/PD controller for automotive active suspension system", *Industrial Electronics, IEEE Transactions on,* vol. 46, no. 6, pp. 1051-1056.

[149] Marko, K. A. and Hampo, R. J. (1992), "Application of genetic programming to control of vehicle systems", *Intelligent Vehicles' 92 Symposium., Proceedings of the,* IEEE, pp. 191.

[150] Huang, S. and Ren, W. (1999), "Use of neural fuzzy networks with mixed genetic/gradient algorithm in automated vehicle control", *Industrial Electronics, IEEE Transactions on,* vol. 46, no. 6, pp. 1090-1102.

[151] Lampinen, J. (2003), "Cam shape optimisation by genetic algorithm", *Computer-Aided Design,* vol. 35, no. 8, pp. 727-737.

[152] Fang, L., Qin, S., Xu, G., Li, T. and Zhu, K. (2011), "Simultaneous optimization for hybrid electric vehicle parameters based on multi-objective genetic algorithms", *Energies,* vol. 4, no. 3, pp. 532-544.

[153] Ribau, J., Silva, C. and Sousa, J. (2013), "Multi-Objective Optimization of Fuel Cell Hybrid Vehicle Powertrain Design - Cost and Energy", Vol. SAE Technical Paper 2013-24-0082.

[154] Galdi, V., Ippolito, L., Piccolo, A. and Vaccaro, A. (2001), "A genetic-based methodology for hybrid electric vehicles sizing", *Soft Computing,* vol. 5, no. 6, pp. 451-457.

[155] Balling, R. J., & Sobieszczanski-Sobieski, J. (1996). Optimization of coupled systems-a critical overview of approaches. *AIAA journal*, *34*(1), 6-17.

[156] Kodiyalam, S. and Sobieszczanski-Sobieski, J. (2001), "Multidisciplinary design optimisation-some formal methods, framework requirements, and application to vehicle design", *International Journal of Vehicle Design,* vol. 25, no. 1, pp. 3-22.

[157] Holland, J. H. (1975). *Adaptation in natural and artificial systems: an introductory analysis with applications to biology, control, and artificial intelligence*. U Michigan Press.

[158] Deb, K., Pratap, A., Agarwal, S. and Meyarivan, T. (2002), "A fast and elitist multiobjective genetic algorithm: NSGA-II", *Evolutionary Computation, IEEE Transactions on,* vol. 6, no. 2, pp. 182-197.

[159] Musnjak, M. and Golub, M. (2004), "Using a set of elite individuals in a genetic algorithm", *Information Technology Interfaces, 2004. 26th International Conference on,* pp. 531.

[160] Ferreira Pinto, A. S. A. (2009), *Evolution of weight, fuel consumption and $CO_2$* (Masters thesis), Instituto Superior Tecnico, Lisbon.

[161] Moawad, A., Singh, G., Hagspiel, S., Fellah, M. and Rousseau, A. (2009), "Impact of real world drive cycles on PHEV fuel efficiency and cost for different powertrain and battery characteristics", *EVS24 International Battery, Hybrid, and Fuel Cell Electric Vehicle Symposium, Stavanger, Norway.*

[162] Wirasingha, S. G. and Emadi, A. (2011), "Classification and Review of Control Strategies for Plug-In Hybrid Electric Vehicles", *Vehicular Technology, IEEE Transactions on,* vol. 60, no. 1, pp. 111-122.

[163] Musardo, C., Rizzoni, G., Guezennec, Y. and Staccia, B. (2005), "A-ECMS: An adaptive algorithm for hybrid electric vehicle energy management", *European Journal of Control,* vol. 11, no. 4, pp. 509-524.

[164] Pisu, P. and Rizzoni, G. (2007), "A Comparative Study Of Supervisory Control Strategies for Hybrid Electric Vehicles", *Control Systems Technology, IEEE Transactions on,* vol. 15, no. 3, pp. 506-518.

[165] Pourabdollah, M., Murgovski, N., Grauers, A. and Egardt, B. (2013), "Optimal Sizing of a Parallel PHEV Powertrain", *Vehicular Technology, IEEE Transactions on,* vol. 62, no. 6, pp. 2469-2480.

[166] Sundstrom, O., Guzzella, L. and Soltic, P. (2010), "Torque-assist hybrid electric powertrain sizing: From optimal control towards a sizing law", *Control Systems Technology, IEEE Transactions on,* vol. 18, no. 4, pp. 837-849.

[167] Fischer, M., Werber, M. and Schwartz, P. V. (2009), "Batteries: Higher energy density than gasoline?", *Energy Policy,* vol. 37, no. 7, pp. 2639-2641.

[168] DEFRA, (2012), "DECC. 2012 Guidelines to Defra/DECC's GHG conversion factors for company reporting", *Produced by AEA for the department of energy and climate change (DECC) and the department for environment, food and rural affairs (DEFRA), UK.*

[169] Marler, R. T. and Arora, J. S. (2004), "Survey of multi-objective optimization methods for engineering", *Structural and multidisciplinary optimization,* vol. 26, no. 6, pp. 369-395.

[170] FUTURE Vehicles (2014), *FUTURE Vehicles website*, available at: http://www.futurevehicles.ac.uk (accessed January 2014).

[171] Hutchinson, T., Burgess, S. and Herrmann, G. (2014), "Current hybrid-electric powertrain architectures: Applying empirical design data to life cycle assessment and whole-life cost analysis", *Applied Energy,* vol. 119, no. 0, pp. 314-329.

[172] CarFolio.com (2014), *Car specification database*, available at: www.carfolio.com (accessed January 2014).

[173] Auto Motor und Sport (2013), *Spritsparpotential Leichtbau ist nicht das Wichtigste (Translated: Fuel saving potential lightweight is not the most important)*, available at: http://www.auto-motor-und-sport.de/eco/spritsparpotential-leichtbau-ist-nicht-das-wichtigste-1478244.html (accessed September 2013).

[174] Scherer, H., Bek, M. and Kilian, S. (2009), "ZF New 8-speed Automatic Transmission 8HP70-Basic Design and Hybridization", *SAE International Journal of Engines*, vol. 2, no. 1, pp. 314-326.